Unconventional superconductivity and strong electronic correlations in molybdenum cluster compounds

Petrovic, Alexander

UNIVERSITÉ DE GENÈVE
Département de Physique
de la Matière Condensée

FACULTÉ DES SCIENCES
Professeur Ø. Fischer

Unconventional Superconductivity and Strong Electronic Correlations in Molybdenum Cluster Compounds

THÈSE

presenté à la Faculté des Sciences de l'Université de Genève
pour obtenir le grade de docteur ès Sciences, mention physique

par

Alexander Petrović
de
Les Agettes (VS)
Frome, Somerset (Angleterre)

Thèse n°

GENÈVE
Atelier de reproduction de la Section de Physique
2009

À mon grand-père
DESIMIR PETROVIĆ
qui souhaitait un docteur dans la famille

Résumé en français

Les composés ternaires à base de clusters de molybdène Mo_6X_8 (X = chalcogénide) peuvent montrer une grande varieté de comportements physiques. Par exemple, ils peuvent être assemblés dans un réseau tridimensionnel pour devenir des “phases de Chevrel” avec composition $M Mo_6X_8$, mais aussi en condensations linéaires - des chaines faiblements couplées - avec des proprietés fortements mono-dimensionnelles: $M_2Mo_6Se_6$. Une grande partie de toute cette famille de composés devient supraconductrice à basse température. Le mécanisme de cette supraconductivité n'était pas encore connu.

Dans cette thèse, nous allons appliquer deux techniques expérimentales très puissantes - la microscopie à effet tunnel (STM) et les mesures de chaleur spécifique - pour essayer de résoudre les mystères de ces composés. Nous avons construit un nouveau STM dans un cryostat hélium-3, qui nous permet de mesurer de très petits échantillons, jusqu'à une température de 400 mK et un champ magnétique de 11 T. En combinaison avec nos mesures calorimetriques, magnétiques et résistives, nous obtenons une vue sans pareille sur le monde des clusters de molybdéne.

Dans $M_2Mo_6Se_6$, les mesures de transport et de chaleur spécifique à très basse température nous indiquent que la supraconductivité dans $Tl_2Mo_6Se_6$ et $In_2Mo_6Se_6$ est fortement influencée par des fluctuations de basse dimension. De plus, le couplage électron-phonon est plus fort dans $Tl_2Mo_6Se_6$ que dans $In_2Mo_6Se_6$. En utilisant une spectroscopie phononique dérivée d'une comparaison de la chaleur spécifique et de la résistivité dans l'état normale, nous avons montré que la supraconductivité dans $M_2Mo_6Se_6$ est crée par un phonon qui a pour origine les chaines Mo_6Se_6, mais que le mode phononique optique du ion M ajoute un couplage additionel pour $Tl_2Mo_6Se_6$.

La transition métal-isolant vue pour $M_2Mo_6Se_6$ (quand M est un ion de Groupe IA) reste assez mystérieuse. Ayant constaté qu'il n'y

a pas de modulation structurale, nous suggèrons que cette transition a pour origine une onde de densité de charge électronique, qui se produit à cause d'une forte anisotropie électronique. Nous postulons aussi qu'un point critique quantique sépare les domaines supraconducteurs et isolants dans le diagramme de phase.

La spectroscopie à effet tunnel de $PbMo_6S_8$ et $SnMo_6S_8$ montre deux gaps supraconducteurs, avec une forte anisotropie dans le plus petit gap (qui n'est quasiment vue que quand on traverse une marche (un parametre de maille) sur la surface des echantillons avec la pointe STM). En faisant des simulations avec un modèle BCS deux-bandes, nous arrivons à bien reproduire nos résultats expèrimentaux. Ces données sont confirmées par des mesures de chaleur spécifique électronique, qui montrent une petite contribution d'une deuxième bande.

En utilisant notre STM pour faire des grandes images des vortexs magnétiques dans $SnMo_6S_8$, nous avons obtenus les premières images d'un verre des vortexs dans l'espace réel. Ayant confirmé que la zone de "l'effet d'aiguille" se trouve dans un partie de l'espace de phase à beaucoup plus haute température et champ, nous tirons la conclusion que le désordre n'est pas limité à la zone de l'effet d'aiguille et qu'il n'y a pas de lien entre la formation d'un verre de vortexs et de cette zone.

La spectroscopie sous champ magnétique des coeurs des vortexes dans $PbMo_6S_8$ et $SnMo_6S_8$ montre un grand "pseudogap", qui ne peut pas être expliqué par les théories conventionelles. Ce pseudogap est beaucoup plus profond dans $PbMo_6S_8$ que dans $SnMo_6S_8$. Nous suggèrons que ce phénomène est lié à une grande dispersion électronique entre les deux bandes.

Contents

A short introduction to Superconductivity, in which we learn the importance of Chevrel phases

Before 1911, condensed matter physics as we know it did not really exist. Phenomenological differences between metals and insulators had been observed but remained unexplained and rudimentary ferromagnets had started to find electrical applications in motors and dynamos; however the electron had only been discovered 14 years previously, the semiconductor revolution was still 40 years away and the concept of a phase transition was only just beginning to receive theoretical attention.

Everything changed when Heike Kamerlingh Onnes liquefied helium at his laboratory in Leiden and noticed an abrupt disappearance of the electrical resistivity of mercury at 4 K: the age of superconductivity had arrived [1]. Although scientists would only realise many years later, this discovery heralded the dawn of strongly-correlated electron physics and launched a century of intensive research. Despite the significant advances in both experimental tools and theoretical methods, new discoveries continue to outpace our understanding of existing problems. Superconductivity remains just as mysterious and exciting now as in 1911.

The ultimate challenge remains the synthesis or discovery of a superconductor which "works" at room temperature, since this would rev-

olutionise energy storage/transfer, electronics, computing and transport among many other potential applications. Sadly this has not yet proved possible (though is by no means out of the question). While the search continues we must strive to fully understand existing superconductors in order to maximise our chances of synthesising a room-temperature version.

Early advances

The first successful theories of superconductivity emerged in the 1930s: the two-fluid model of Gorter and Casimir [2] and the London equations which describe the electrodynamics of superconductors [3]. The next breakthrough came in 1950 with the development of the powerful phenomenological Ginzburg-Landau theory [4], which describes the free energy of a superconductor as an power-series expansion of the order parameter and may be applied to all superconducting materials within the mean-field limit. This divided superconductors into two classes - types I and II - depending on their surface energies. Shortly afterwards, Abrikosov solved the Ginzburg-Landau equations for type II superconductors in a magnetic field and realised that the field penetrated in a regular array of quantised flux vortices, the so-called vortex lattice.

However, it was not until 1957 that the first microsopic theory was developed by Bardeen, Cooper and Schrieffer [5]. This model is based on the principle that the local positive charge density from a lattice distortion (phonon) generated by a passing electron is able to attract a second electron, thus forming a pair. The pairs of electrons are phase-coherent and condense into a single macroscopic quantum ground-state, described by a wavefunction whose characteristic lengthscale ξ_0 corresponds to twice the pair radius. Each pair is bound together by a condensation energy 2Δ, leading to the opening of a gap of width Δ beneath the Fermi level E_F in the single particle tunnelling spectrum within the superconducting phase.

The BCS model was immediately a great success, although only valid in the weak electron-phonon coupling limit. Gor'kov soon derived the Ginzburg-Landau equations from BCS theory [6] and Eliashberg later extended the BCS formalism to describe strongly-coupled materials [7]. However, somewhat disappointingly these theories appeared to predict an upper limit to the superconducting critical temperature T_c of around 30 K. The most advanced model for calculating T_c was developed by McMillan in 1968 and successfully described the majority of super-

conductors then known; however the 30 K limit to T_c was thought to remain.

Experimentalists had not been resting on their laurels in the midst of all this theoretical activity. The maximum known T_c had been slowly but steadily increasing since 1911, peaking at 23.2 K in 1971 with the discovery of Nb_3Ge (a member of the A-15 family), a figure altogether compatible with BCS theory and the McMillan formula. Over the next 15 years many more exotic superconductors would be discovered, in particular the Chevrel phases in 1973 [8], heavy fermion compounds in 1978 [9] and the organic Bechgaard salts a year later [10]. Although the physics in these new materials was clearly much more unconventional (and hence of greater interest) than that of classical low-T_c materials, frustratingly it did not prove possible to improve on T_c^{Max} = 23.2 K.

The high-T_c era

Arguably the biggest revolution in solid-state physics since the development of the transistor took place in 1986 at the IBM laboratory in Zürich, where Bednörz and Müller discovered superconductivity at 30 K in the copper oxide material $La_{1.85}Ca_{0.15}CuO_4$ [11]. The rest of the research world dropped whatever it was doing and focussed all its resources on this new high-T_c cuprate family. T_c^{Max} rapidly climbed, first breaking the 77 K liquid nitrogen barrier with $YBa_2Cu_3O_{6+x}$ [12], then peaking at 164K (under pressure) in $HgBa_2Ca_2Cu_3O_{8+\delta}$ [13]. The parent compound of any high-T_c cuprate is an antiferromagnetically ordered Mott insulator, which may then be doped by adding charge carriers (electrons or holes). As the doping increases, we pass through a glassy régime featuring short-range charge and spin ordering, before reaching the characteristic superconducting "dome" [14]. A quantum critical point is thought to lie beneath this dome, separating Fermi liquid and non-Fermi liquid (glassy) groundstates.

Theoretical debate continues to rage uncontrollably over the mechanism responsible for superconductivity in the cuprates, with the three most popular schools of thought being Anderson's resonating valence bond (RVB) theory [15], Laughlin's Gossamer superconductivity [16] and Varma's fluctuating current loops [17]. A cynical observer might claim that the only true scientific breakthrough we have made is the seemingly unlimited release of large quantities of energy whenever two rival theoreticians are placed in the same room. However, humour aside the painful truth is that 23 years after the initial discovery, we

are scarcely any closer to developing a microscopic description of high-T_c superconductivity than we were 10 years ago.

A little quantum mechanics

So what do we know? It has been confirmed beyond reasonable doubt that the symmetry of the order parameter in hole-doped cuprates is d-wave, thanks to the seminal phase-sensitive experiments of Tsuei and Kirtley [18]. The vast majority of other known superconductors display s-wave symmetry. The s and d are a basic quantum-mechanical nomenclature referring to the orbital angular momentum L of the Cooper pair: an s-wave pair is a spin singlet (S = 0) with L = 0 but a d-wave pair has L = 1. It is also possible to pair electrons in a spin-triplet configuration: p-wave symmetry (as found in quasi-1D Bechgaard salts [19] and iron under very high pressure [20]) has S = 1 and L = 0 while f-wave pairs (which are hypothesised to exist in Sr_2RuO_4 [21]) would have L = 1. A d-wave order parameter has the important property of possessing nodes in its gap function, i.e. points on its Fermi surface where Δ = 0, marking the crossover between positive and negative-phased gaps. This implies that for certain directions in momentum space, the pairing interaction (the "glue" holding the Cooper pairs together) must be repulsive rather than attractive. The concept of a highly anisotropic pairing interaction is incompatible with strongly overlapping pairs arising from a large coherence length ξ, since any variations in the pairing will average to zero over large separations. d-wave superconductors therefore tend to have short coherence lengths and high upper critical fields; hence they are potentially more useful for practical applications.

The mysterious Pseudogap

We are also aware of the existence of a "pseudogap" in the phase diagram of the cuprates. A pseudogap is essentially a depletion of spectral weight around E_F which develops at high temperature (above T_c) and may be detected by a variety of experimental techniques, including tunnelling methods, angle-resolved photoemission spectroscopy (ARPES) and specific heat measurements.

It was originally suggested that the pseudogap was a "pairing gap" due to high-temperature incoherent pair formation at temperature $T^\star$, with phase coherence and bulk superconductivity eventually setting in

at T_c. Within this interpretation, a pseudogap should be visible above the entire superconducting dome. This is generally consistent with tunnelling experiments [22]. However, heat capacity data and other experiments indicate that the pseudogap terminates in the middle of the dome, possibly at the quantum critical point [23]. Recent ARPES experiments suggest that the pseudogap is a competitor to superconductivity and may predominantly be found in the antinodal regions of momentum space [24]. This casts seeds of doubt over whether different experimental techniques are sensitive to the same gap and remains an open question.

In tunnelling spectroscopy, the pseudogap is representative of the normal state of a material in the absence of bulk superconductivity. Vortex cores in a type II material can therefore provide invaluable information regarding the nature of superconductivity, since within the cores the superconductivity is locally destroyed. The core spectra reveal the bound states of the core [25], superposed on the low-temperature normal state signature. Both the bound states and the normal state density of states (DoS) will vary depending on the superconducting order parameter and the cleanliness of the material, i.e. the ratio of the superconducting coherence length to the electronic mean free path.

Twists along the road to enlightenment

The past 10 years have not been without their success stories. In 2001 Nagamatsu and co-workers discovered superconductivity at 39 K in MgB_2, which briefly usurped the cuprates as material of choice for the world's researchers. Initial confusion over the symmetry of the order parameter was resolved with the discovery of two distinct superconducting gaps: a large gap in the 2D σ band and a smaller induced gap in the 3D π band. Following this observation, MgB_2 was quickly shown to follow two-band BCS theory, with a high-energy 58 meV phonon mediating the pairing interaction. It is now regarded as the textbook example for multiband superconductivity and is the only superconductor with a T_c of over 20 K which we can profess to understand well. Research continues into powder-based cables and high-field dirty-limit films for applications [26, 27] and it is hoped that MgB_2 can make the significant commercial impact envisaged back in 2001. However, from a research perspective the impression that physicists "understand" MgB_2 has led to the spotlight falling firmly back on cuprates and other more exotic materials in recent years.

Very recently, the research community was thrown into disarray by the discovery of superconductivity in the family of iron pnictides [28]. The shock lies in the iron content of these materials, in spite of their high T_cs (up to 57 K in $Sm_{0.95}La_{0.05}O_{0.85}F_{0.15}FeAs$ [29]). Iron is the archetypal ferromagnet and ferromagnetism is generally incompatible with spin-singlet superconductivity (since it acts to align spins and hence breaks pairs). The presence of iron in a bulk superconducting material is therefore suggestive of an unconventional pairing mechanism. Currently, the leading theoretical model promotes a multi-band $s^{+/-}$ scenario in which superconductivity is mediated by antiferromagnetic correlations and s-wave gaps on different Fermi surfaces have order parameters which are out of phase by π [30]. Iron pnictides display extremely high upper critical fields (over 100 T) and it is thought that this may be due to the multi-band order parameter [31]. Just like the other high-T_cs, pnictides have many secrets still to reveal despite the significant advances made in the last year.

The revenge of the Chevrel phases

In this chaotic world, it may sometimes be instructive to look backwards in order to move forwards. Faced with an apparent impasse in research on the high-T_c cuprates, our attention in Geneva turned to a long-forgotten problem from the 1970s and early '80s: Chevrel phases and other molybdenum chalcogenide cluster-based materials.

The Mo_6X_8 (X = S, Se, Te) cluster is a remarkably versatile building block for strongly-correlated electron systems, since it can be assembled using a variety of different structures. This allows the synthesis of a vast family of compounds with wide-ranging physical properties, not only caused by their varying chemical content but more importantly due to their effective dimensionality. For example, individual clusters may be weakly coupled into a quasi-3D network by metallic ions to form the well-known quasi-three-dimensional (q3D) Chevrel phase materials [8]. Alternatively, Potel succeeded in stacking clusters end-to-end to create infinite-length chains, then coupling these chains using Group IA or III cations to form highly one-dimensional metals [32]. A large class of intermediate compounds also exist, consisting of weakly-coupled finite-length chain fragments. Many Chevrel phases become superconducting at low temperature, with $T_c^{Max} \sim 15$ K in $PbMo_6S_8$. Chain-based compounds also exhibit a superconducting instability, although this appears to compete with a metal-insulator transition to

become the low-temperature groundstate.

One attribute shared by all superconducting Mo_6X_8 cluster-based materials is a short coherence length (pair size) along at least one crystallographic axis (since the clusters are always weakly coupled in at least one direction). In $PbMo_6S_8$, early pulsed-field experiments in the early 1970s indicated an upper critical field $H_{c2} \sim$ 55-60 T [33]. Prior to the discovery of the high-T_c cuprates, this was 50% higher than that of any other superconductor. Applying standard single-band Ginzburg-Landau theory, this corresponds to a coherence length of around 20 Ångstroms, a value which approaches those found in the cuprates (e.g. $\sim$ 24 Å in $La_{2-x}Sr_xCuO_4$ and $\sim$ 19 Å in $YBa_2Cu_3O_{7+\delta}$). Such high upper critical fields aroused great interest in the early 1980s and many efforts were made to explain them theoretically (without success). It has been shown that neither enhanced spin-orbit scattering nor strong electron-phonon coupling is sufficient to account for H_{c2} [33]. Another factor driving the research effort was the discovery of rare-earth-coupled Chevrel phases with long-range magnetic ordering [34].

Previous tunnelling experiments in $PbMo_6S_8$ have displayed an unusually high zero-bias conductance, which at non-zero temperature indicates an anisotropic order parameter [35]. Given their short coherence lengths, this raises the important question of whether Chevrel phases could share a d-wave order parameter with the cuprates. If so, Chevrel phases would provide a much simpler system than cuprates in which to study a d-wave pairing interaction, since they do not exhibit any intrinsic magnetism. Even if the Chevrel phases do not have a d-wave order parameter, our puzzle remains just as interesting since we now need to provide a reason for their exotically high H_{c2} within a potentially more conventional superconducting framework.

However, not every practical application will require a superconductor with an ultra-high critical field. As we enter the age of nanotechnology, it becomes increasingly necessary to understand the behaviour of electrons in systems with reduced dimensionality such as nanowires, both in metallic and superconducting phases. Research has recently focussed on MoSe nanowires: although lacking the tensile strength of their carbon nanotube rivals, it is easier to manipulate the electronic properties of MoSe [36]. The $M_2Mo_6Se_6$ linear cluster condensates present us with a golden opportunity to study a related system lying on the boundary of a superconducting instability, whose dimensionality may be readily modulated by changing the M ion. Previous work has indicated that $M_2Mo_6Se_6$ are the most strongly one-dimensional super-

conductors currently known [37], thus offering us a uniquely powerful chance to observe the effects of low-dimensional fluctuations on both superconducting and metal-insulator phase transitions.

Motivated by the great promise of the Mo_6X_8 cluster, we present a comprehensive study of a selection of Chevrel phase superconductors $M Mo_6S_8$ and the entire quasi-one-dimensional (q1D) $M_2Mo_6Se_6$ family, using a variety of experimental techniques. Numerous longstanding questions will be resolved, including:

- The nature of superconductivity in $M_2Mo_6Se_6$
- The origin of the metal-insulator transition in $M_2Mo_6Se_6$
- The order parameter in q3D Chevrel phase superconductors
- The topology of a vortex glass and the origin of the Peak effect in type-II superconductors
- The nature of vortex cores in a two-band superconductor with non-negligible inter-band scattering

Spurned by researchers around the world following the discovery of the cuprates and denounced as "conventional BCS superconductors" following the observation of an isotope effect in the related binary compound Mo_6Se_8 [38], the time is ripe for the Chevrel phases and friends to return to the fold. They may still have the last word in the riddles of high critical field and low-dimensional superconductivity.

Chapter 1

Theoretical Concepts and Tools

There are two types of experimental physicists: those who consecrate their careers to the perfection of a single technique and those who address the problems at hand using whichever technique they feel is most suitable. While the latter category of researchers undoubtedly lack the deep knowledge of their equipment which can only be acquired through years of practice, no single technique can give all the answers to a complex physical problem and it is only by polyvalency or collaboration that a physicist may conclusively solve a demanding puzzle.

With this in mind, we have combined scanning tunnelling microscopy (a local spectroscopic probe) with high-resolution specific heat measurements (a bulk thermodynamic technique) in an effort to understand the physics of molybdenum cluster-based materials. These two techniques are not only complementary but also mutually verifying, together providing a uniquely detailed image of the strongly-correlated electronic behaviour inherent to both short coherence length and low-dimensional superconductivity. Where appropriate, we have also supplemented our data with electrical transport, magnetic and synchrotron X-ray diffraction measurements (although the latter will only be discussed phenomenologically in chapter 5).

However, even the highest quality experimental data is almost meaningless without a grasp of its physical origins. An understanding of the theories which could explain experimental observations is also invaluable, even though the most exciting data will blaze a trail for theoreticians to follow. In this chapter we outline the physical laws underpin-

ning scanning tunnelling microscopy and specific heat measurements. We quantitatively explain the behaviour of superconductors when measured using these techniques and introduce several theoretical models which will be employed in later chapters.

1.1 Scanning Tunnelling Spectroscopy

The gates to the nano-kingdom were thrown open in 1981 with the invention of the scanning tunnelling microscope (STM) by Binnig and Rohrer at the IBM Rüschlikon lab near Zürich [39]. For the first time, the world had access to an instrument capable of producing atomic-scale real-space images. Nearly 30 years later, other local probes such as atomic/magnetic force microscopy or scanning near-field optical microscopy may offer a similar degree of topographic resolution but the true strength of STM lies in its spectroscopic abilities. It remains the only experimental probe capable of yielding the momentum-averaged local electronic density of states (LDoS), thus opening a completely new avenue towards the exploration of numerous fundamental material properties. The intrinsic heterogeneity, strong electronic correlations and short characteristic lengthscales render STM particularly apt for studying superconductivity, charge density waves and other unconventional areas of condensed-matter physics.

1.1.1 STM theory

Scanning tunnelling microscopy was founded on a basic quantum-mechanical premise: a wavefunction may "tunnel through" a potential barrier with a transmission coefficient which decays exponentially as the barrier width increases. In practice, this means that if two conductors are brought into close proximity and one is biased with respect to the other, a current can still flow between them due to the evanescent electron wavefunction propagating within the barrier. A schematic of the tunnelling effect is shown in Fig. 1.1.

The breakthrough made by Binnig and Rohrer was their realisation that a high-resolution probe could be created by employing the extremely sensitive barrier-thickness dependence in quantum tunnelling. The tunnel current flowing from a biased sample to a metallic tip is given by

$$I \propto e^{-2\aleph z} \tag{1.1}$$

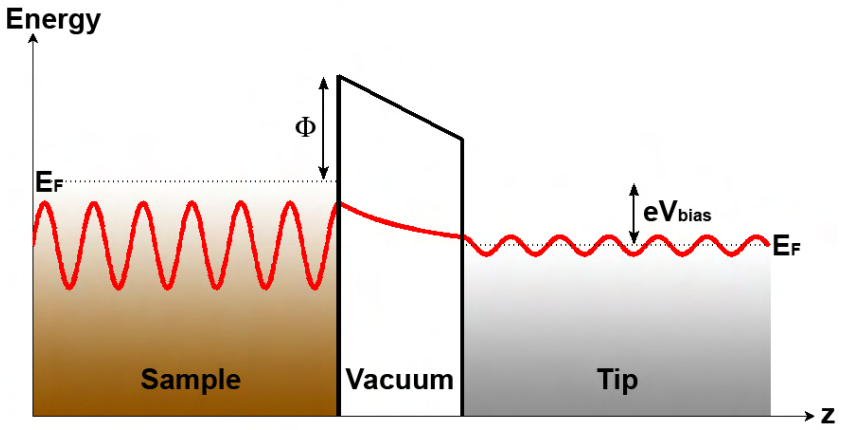

Figure 1.1: One-dimensional vacuum tunnelling schematic. Note that in real STM experiments the sample bias voltage eV_{bias} is much smaller than the work function Φ.

where z is the tip-sample separation and the wavefunction decay rate $\aleph = 2m_e\Phi/\hbar$ is a function of the potential barrier height Φ (also known as the work function). A STM therefore measures the spatial variation of the tunnel current and converts this into topographic information.

Two basic measurement modes exist: constant current or constant height imaging. Constant height mode permits the fastest measurements, but can only be used on extremely flat samples. An additional disadvantage is the lack of knowledge of the local I(z) relation and hence work function, thus rendering it difficult to extract any absolute surface height values. Constant current imaging involves regulating the tip-sample separation to maintain a constant current as the tip scans over the sample surface. Measurements take longer due to the delay from the feedback circuit, but it is possible to directly measure the local height variation and the risk of crashing the tip into uneven parts of the surface is also greatly reduced. For these reasons, all topographic measurements displayed in this work were performed in constant current mode.

If we only wanted simple topographic data from our STM, we could draw a close to our discussions here. However, we wish to perform spectroscopy and it is therefore necessary to understand the relationship between the tunnel current and the local electronic densities of states, both of sample and tip. In the following, we will briefly out-

line the transfer Hamiltonian tunnelling description and the first detailed analysis of the tunnel current by Tersoff and Hamann. Many outstanding reviews of this field have already been published, in particular references [40, 41] and the reader is urged to explore these to indulge any deeper theoretical desires.

Bardeen was the one of the first scientists to successfully address the problem of electron tunnelling [42]. Using his ideas, we treat tip t and sample s as independent quantum systems and consider the transfer of electrons between them. This is controlled by the transfer Hamiltonian:

$$H_{trans} = \sum_{ts} T_{ts} c_t^\dagger c_s + \text{higher order terms} \tag{1.2}$$

Within the second quantisation formalism, operator c_s annihilates a particle in state ψ_s and operator $c_t^\dagger$ creates a particle in state ψ_t. T_{ts} is the tunnelling matrix element, obtained by integrating the following expression over any surface S lying entirely within the vacuum barrier between tip and sample.

$$T_{ts} = \frac{-\hbar^2}{2m} \int dS.(\psi_t^\star \nabla \psi_s - \psi_s \nabla \psi_t^\star) \tag{1.3}$$

For a small junction bias V_b, the single-particle tunnel current I_t may be calculated by linear response theory and is given by

$$I_t(V_b) = \frac{2\pi e}{\hbar} \int d\omega \left[f(\omega - eV_b) - f(\omega) \right] \sum_{ts} \left| T_{ts} \right|^2 A_s(\omega) A_t(\omega - eV_b) \tag{1.4}$$

where A_s and A_t are the single-particle spectral functions of sample and tip respectively and $f(\omega)$ is the Fermi function. This equation basically states the conditions necessary for tunnelling to occur: electrons in state ψ_s may tunnel into state ψ_t provided that:

- the tunnelling matrix element between the states T_{ts} is non-zero
- the states have the same energy, following alignment by eV_b
- the Fermi function overlap allows tunnelling from occupied to empty states

Calculating the tunnelling matrix element is not straightforward, since it requires knowledge of the tip wavefunctions. These are generally uncertain, given that we have no means of measuring the exact geometry

of our tips. Tersoff and Hamann circumnavigated this problem by modelling the end of the tip as a sphere centred on position $\mathbf{r_0}$ and hence conveying spherically symmetric symmetry to the tip wavefunctions. A schematic of their model is shown in Fig. 1.2.

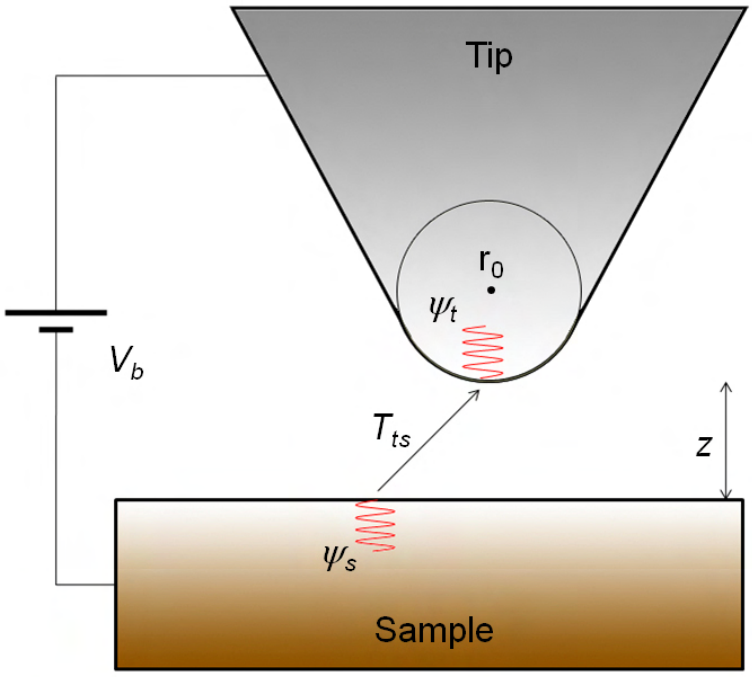

Figure 1.2: Modelling single-particle tunnelling using the Bardeen transfer Hamiltonian formalism and the Tersoff-Hamann approach to evaluating the transfer matrix T_{ts}.

Within the spherical approximation, $|T_{ts}|^2 \propto |\psi_s(z)|^2$. We may now re-express the single-particle spectral functions as the real-space LDoS $N(r,\omega)$ to obtain

$$I_t(V_b) \propto \int d\omega \, [f(\omega - eV_b) - f(\omega)] N_s(\mathbf{r_0}, \omega) N_t(\omega - eV_b) \tag{1.5}$$

This shows that I_t is merely a thermally-smeared convolution of the tip and sample densities of states. Assuming that the tip has a constant density of states within eV_b of the Fermi level, we may differentiate

equation 1.5 with respect to V_b to obtain the differential conductance:

$$\frac{dI_t}{dV_b}(\mathbf{r_0}, V_b) \propto \int d\omega \left[f'(\omega - eV_b) \right] N_s(\mathbf{r_0}, \omega) \tag{1.6}$$

Within this approximation, the derivative of the tunnel current with respect to the bias voltage is directly proportional to the local density of states in the sample. This relationship is the cornerstone of tunnelling spectroscopy.

For the approximation that a tip has spherically-symmetric wavefunctions to be valid, it must be terminated with s-wave electronic states. However, the majority of tip materials used for STM experiments are d-band metals, due to their mechanical resilience and low reactivity. The angular dependence of the d-band modifies the tunnelling matrix element, resulting in it being proportional to the second derivative of the sample wavefunction at $\mathbf{r_0}$ rather than the wavefunction itself [43, 44]. This results in any topographic corrugations being accentuated by a d-band tip, but does not affect the proportionality of $\frac{dI_t}{dV_b}$ to the LDoS.

While the power to measure the LDoS is clear, the debate over whether it is actually possible to image an electronic bandstructure using STM (as suggested by Tersoff and Hamann) continues unabated. However, recent observations of a large peak consistent with a Van Hove singularity in the high-T_c cuprate Bi-2201 [45] appear to confirm Tersoff and Hamann's claims; the opposing Harrison conjecture is thought to only apply to planar tunnel junctions [46].

1.1.2 Tunnelling in superconductors

In the previous section, we have tacitly assumed that both tip and sample are metallic. However, the analysis is still valid for tunnelling from a metallic tip into a superconducting sample (or vice versa); the only difference is that one of the two densities of states convolved during tunnelling now has a characteristic gap of width 2Δ around the Fermi energy.

It is important to note that the microscopic procedure for electron tunnelling is different from that for hole injection. When the sample is negatively biased at $eV_b > \Delta$ with respect to the sample, an electron simply tunnels straight from the tip into an empty quasiparticle state above the Fermi level. However, for positive sample bias (hole injection), an electron must leave the superconductor. This necessitates breaking

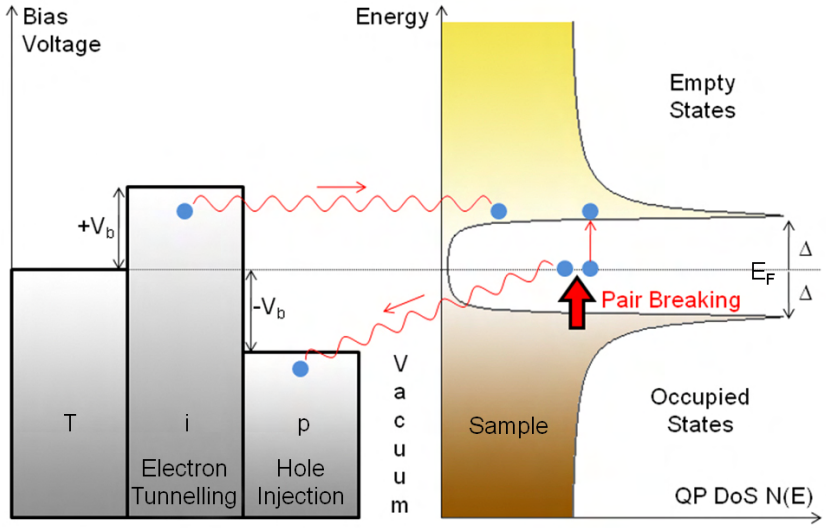

Figure 1.3: Current flow in a Superconductor-Insulator-Normal tunnel junction, highlighting the different physical mechanisms for electron tunnelling and hole injection. A BCS s-wave quasiparticle density of states (QP DoS) has been used for illustrative purposes.

a Cooper pair, releasing energy 2Δ and hence creating two quasiparticles at the Fermi level. One of these particles will tunnel through the barrier to the tip, the other is excited to a state above the gap in order to conserve energy.

Strong electronic correlations may lead to an asymmetry in the measured LDOS in certain doped compounds, such as the cuprates [47]. Other more subtle factors are also able to influence the LDOS, including low-energy bosonic modes. For example, in strongly-coupled phonon-mediated superconductors it should be possible to observe a small spectral renormalisation located at Δ plus the phonon energy. Interactions with local resonant modes have also been observed in tunnelling spectra for high-T_c cuprates [48].

1.1.3 Pairing symmetry and BCS gap equations

In order to interpret tunnelling spectra in a superconductor, a theoretical model for the LDoS is generally fitted to the experimental data.

The variation of the LDoS is dependent on the symmetry of the superconducting gap: given that almost nothing is known about the superconducting groundstate of the Chevrel Phases except the fact that low-energy quasiparticle states seem to be present [35], a highly generalised gap equation is clearly required. The three principal symmetry scenarios which should be considered are shown in Fig. 1.4. We do not consider p-wave or more exotic order parameters since there is no breakage of spatial inversion symmetry in the Chevrel Phases.

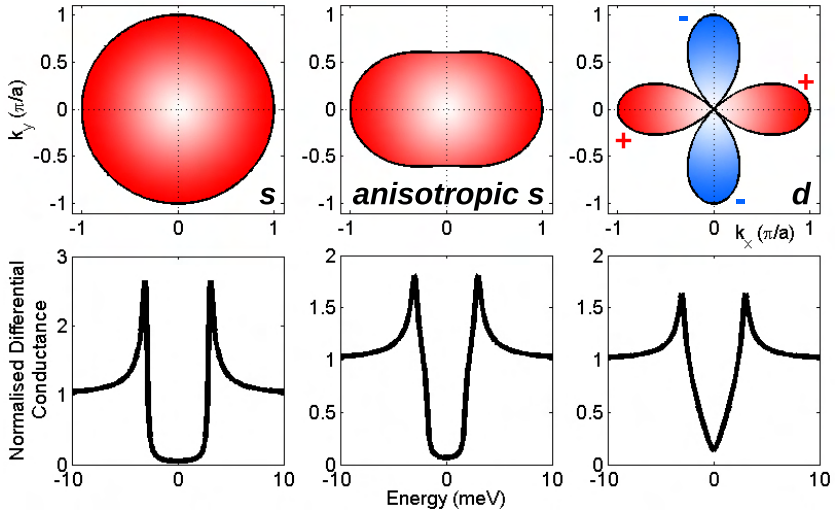

Figure 1.4: Above: **k**-space variation of the superconducting gap for s-wave, anisotropic s-wave and d-wave gap symmetries. Note the change of phase in the d-wave graph. Below: corresponding simulated zero-temperature tunnelling spectra. Δ_0 = 3 meV, Γ = 0.15 meV and for the anisotropic s-wave a = 0.8 (see text for details).

It is therefore necessary to introduce a momentum-dependent gap function $\Delta_{\mathbf{k}}$ into the Dynes expression for the BCS density of states. A full derivation of the Dynes equation is beyond the scope of this work; however details may be found in ref. [49]. We obtain

$$N(\omega) = \frac{1}{2\pi}\int_0^{\pi} \mathrm{Re}\left[\frac{(\omega + i\Gamma)\mathrm{sign}(\omega)d\theta}{\sqrt{(\omega+i\Gamma)^2 - \Delta_{\mathbf{k}}^2}}\right] \tag{1.7}$$

in which the Dynes broadening parameter Γ is related to the quasiparticle lifetime τ by $\tau \sim \hbar/\Gamma$, θ describes the azimuthal variation of

wavevector k and the gap momentum dependence is given by

$$\Delta_{\mathbf{k}} = \Delta(T)F(\theta) \quad \text{with} \quad F(\theta) = a + (1-a)\cos 2\theta \tag{1.8}$$

where $\Delta(T)$ is the temperature-dependent gap value and a parametrises the gap anisotropy. a = 1 corresponds to isotropic s-wave symmetry, while a = 0 describes a purely d-wave scenario (see fig. 1.4). $0 < a < 0.5$ yields mixed s/d-wave symmetry, while a = 0.5 is the limiting case describing an s-wave gap with nodes but no phase-change. If $0.5 < a < 1$ the resultant gap has anisotropic s-wave symmetry; a similar model has already been used to deduce a 30% gap anisotropy in the pyrochlore compound KOs_2O_6 [50]. Since STM is not a phase-sensitive probe, the useful fitting range of this model only covers a = 0 and $0.5 < a < 1$.

1.1.4 Signatures of the vortex core

Superconductors may be classified as type I or type II, depending on their behaviour in a magnetic field [4]. Type I superconductors have a positive normal/superconductor interface energy: there is therefore total field exclusion until the critical field H_c at which point field penetration is total and the material reverts to normal. Such materials generally have low T_c values (< 5 K), exhibit rather conventional behaviour and will not be further considered here. In type II superconductors the surface energy is negative and in a magnetic field the superconductor will thus seek to minimise its free energy by maximising the normal/superconductor interfacial area. This is achieved by field penetration at a field H_{c1} in the form of quantised vortices, each carrying $\Phi_0 = h/2e$ of magnetic flux. The radius of each vortex is approximately equal to the coherence length ξ: by measuring the size of a vortex and applying Ginzburg-Landau theory [51], we may rapidly estimate H_{c2} for any type II superconductor.

The thermodynamic groundstate configuration of these vortices has hexagonal symmetry and is known as an Abrikosov lattice [52]. An example of this is shown in Fig. 1.5. It is simple to calculate the lattice parameter a_0, since the flux penetration corresponds to the applied field H: $a_0 = 48.8/\sqrt{H}$ where a_0 is measured in nanometres and H in Tesla.

The centres of each region of flux penetration are known as the vortex cores; we may consider them as quasi-normal islands in a superconducting matrix. Given that superconductivity must be locally destroyed in the cores, the LDoS should be markedly different from that in the matrix. STS allows us to measure the variation in the local density of states over a wide area, thus creating a map of vortex locations. In

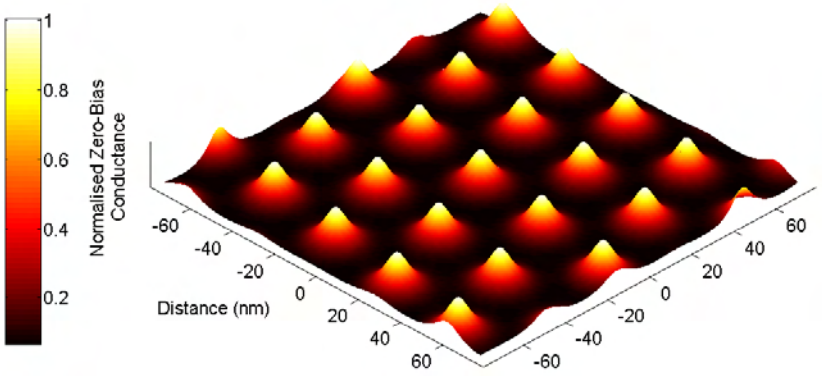

Figure 1.5: 150 × 150 nm dirty-limit zero-bias conductance map for an Abrikosov lattice with H = 2 T and ξ = 30 Å.

contrast with older Bitter decoration vortex imaging techniques which are only viable in low applied fields, STS may be used to image the vortex topology over a wide magnetic field range.

The characteristics of a superconducting spectrum are the deep gap and the twin coherence peaks. For rapid imaging, an optimal matrix/core contrast may therefore be obtained by measuring the spatial variation in the ratio between peak and zero-bias conductances σ_{pk} and σ_{zbc}. This contrast will depend on the nature of the vortex core states: the true power of STS lies in the ability to track these with position, field and temperature.

The first calculations for the LDoS were performed in 1964 [53] and describe the so-called "clean limit" in which the superconducting coherence length ξ is less than the mean free path l. Discrete quantised core states are predicted, dominated by a large zero-bias conductance peak with fringes similar to a diffraction pattern. Experimentally, the clean limit has been observed in $NbSe_2$ (see Fig. 1.6 left), with $\sigma_{pk}/\sigma_{zbc} > 1$ in the matrix and $\sigma_{pk}/\sigma_{zbc} < 1$ in the vortex cores.

The situation changes if $l < \xi$ and we move into the "dirty limit". In this case, scattering - either intrinsic or impurity-based - smears out the discrete states in the vortex core, leaving a flat conductance reminiscent of a normal metal. This has been observed in $NbSe_2$ [56] and is also the case for MgB_2 (Fig. 1.6 right) and the majority of other non-high-T_c superconductors whose cores have been investigated. Vortex core behaviour is rather different in high-T_c cuprates since the normal

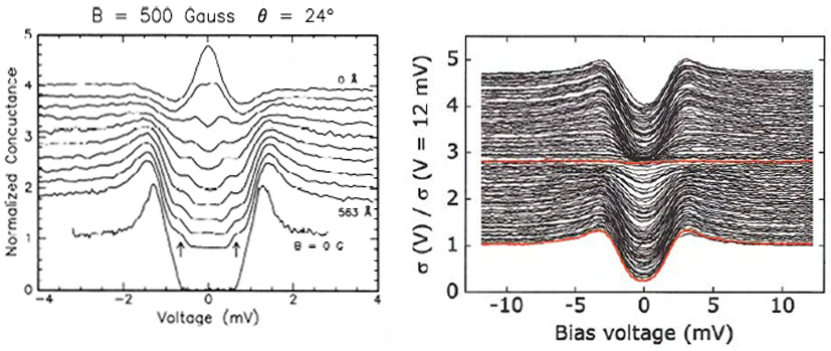

Figure 1.6: Left: clean-limit vortex core spectra showing a clear zero-bias conductance peak in $NbSe_2$ from ref. [54]. Right: a dirty-limit vortex core in MgB_2 from ref. [55] displaying the characteristic flat core spectrum. It should be noted that an analysis of the vortex cores in MgB_2 is not trival due to the two-band order parameter.

state is pseudogapped; this will be discussed further in chapter 8.

1.1.5 Multi-band superconductivity

There is no restriction on a material having more than one electronic band at the Fermi level, i.e. a compound Fermi surface. Providing that these bands are not degenerate, then for a phonon-mediated superconductor there is no reason to suppose that the electron-phonon coupling (and hence superconducting pairing interaction) will be the same for each band. It is therefore entirely conceivable that a strong pairing interaction in a band with relatively low density of states can induce superconductivity in another (weakly-coupled) band at the Fermi level through inter-band scattering, unless the two bands are perfectly orthogonal and scattering is hence impossible (a rather unlikely scenario). The superconductivity "profits" from the increased density of states contributed by the second band, thus increasing the bulk T_c of the material.

This is not a new concept and was first suggested by Suhl *et al.* in 1959 [57]. Despite some limited calorimetric [58] and tunnelling [59] evidence for multi-band superconductivity, we had to wait until the discovery of MgB_2 in 2001 for a clear and unambiguous example. MgB_2 was the first multi-band superconductor to be investigated by STM,

with early measurements on polycrystals resulting in conflicting values for the superconducting gap. However, with improved sample quality it became clear that tunnelling parallel to the c-axis only imaged a single (small) gap, whereas two gaps were visible when tunnelling perpendicular to c (see Fig. 1.7).

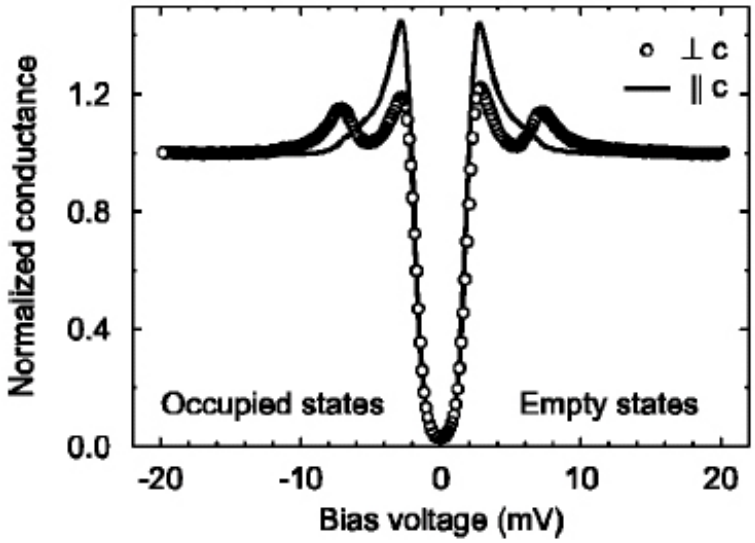

Figure 1.7: Scanning tunnelling spectroscopy in MgB_2 (taken from ref. [60]. Both gaps are clearly visible when tunnelling perpendicular to c (circles); however only the weakly-coupled gap from the π band is visible when tunnelling parallel to c (solid line).

In a first approximation, tunnelling spectra for a multi-band superconductor may be modelled simply by a linear superposition of single-band BCS LDoS for each band at the Fermi level. This assumes that the samples are clean and that inter-band scattering is low. As we will see in Chapters 6 and 8, the nature of electron scattering has a huge influence on multi-band superconductivity, far more so than in single-band superconductors. Enhancing the inter-band scattering (for example by irradiating the material, introducing defects and hence scattering centres) has been shown to "mix" the two superconducting gaps and reduce T_c in MgB_2 [61]. Since inter-band scattering is intrinsically very weak in MgB_2, two gaps remain visible even after substantial irradi-

ation and a drop in T_c of nearly 10 K. However, in a superconductor more susceptible to inter-band scattering, impurities could in principle easily convert the double-gapped order parameter into effectively an anisotropic single-gap superconductor in the dirty limit. No theory currently exists to describe this effect in tunnelling spectra and caution must therefore be exercised when interpreting results.

1.2 Specific Heat Analysis

The heat capacity of a material at constant pressure C_P is defined as

$$C_P = \left.\frac{\partial Q}{\partial T}\right|_P \tag{1.9}$$

where Q is the amount of thermal energy flowing into or out of the sample. The vast majority of experimental calorimeters measure at constant pressure and we will henceforth refer to C_P as C.

C is a purely thermodynamic and hence universally sensitive quantity which mixes electronic, lattice and (occasionally) magnetic contributions. This universal sensitivity explains why the heat capacity of a material remains the most powerful bulk probe of its physical properties. Understanding how to correctly separate its integral components is not always straightforward, but remains the key to successful specific heat measurements.

1.2.1 Electrons and phonons in the normal state

At high temperatures (above $\sim$ 10 K), the heat capacity is dominated by lattice contributions, i.e. phonons. Two distinct models exist for modelling phononic specific heat:

- The Einstein approach which superposes a series of ideal "Einstein mode" one-dimensional oscillators with discrete frequencies. This is most commonly used for simulating optical phonons, which retain a finite frequency when their wavevector $\mathbf{k} \to 0$.
- The Debye approximation which assumes a constant phonon velocity, then considers the total degrees of vibrational freedom available to a crystal and uses this to create a cut-off wavevector $\mathbf{k_D}$. Due to the constant sound velocity assumption, this model is best suited to simulating acoustic phonons.

A comprehensive review of both models may be found in any solid-state textbook, such as ref. [62]. At low temperatures (below $\sim$ 20 K) the most useful result is an approximation to the Debye model:

$$C_{latt} = \sum_{2j+1} \beta_j T^j \qquad j = 1 \ ... \ n \tag{1.10}$$

In practice, it is rarely necessary to include terms of higher order than n = 2 in equation 1.10. For more detailed simulations of the phonon density of states using data from 350 mK to 300 K, we apply a simple model based on a finite array of Einstein modes to fit our experimental results. This will be described in detail in chapter 4.

The low-temperature electronic heat capacity of a metal is characterised by the Sommerfeld constant γ and varies linearly with temperature:

$$C_{elec} = \gamma T \tag{1.11}$$

γ is equal to the electronic density of states (DoS) at the Fermi level and (discounting thermal broadening from the Fermi function) should not vary with temperature or applied field. In a superconductor, γ vanishes as $T \ \rightarrow \ 0$ due to the depletion of the DoS at E_F as the gap opens.

In compounds with antiferromagnetic correlations such as spin ladders, there is a further magnetic contribution to the specific heat from spin wave excitations known as magnons. However, since we have been unable to detect any evidence for antiferromagnetism in the materials studied in this work this will not be further discussed.

1.2.2 Superconductivity: coupling and entropy

In zero-field, the onset of superconductivity is heralded by a second-order phase transition at T_c. Since the heat capacity is a second-order derivative of the free energy, a discontinuity ("jump") in $C(T)$ occurs at T_c due to the formation of phase-coherent pairing states. The size of this jump is proportional to the square of the BCS coupling ratio $2\Delta/k_BT_c$. The electronic heat capacity was first calculated for a weakly-coupled isotropic BCS s-wave superconductor in 1959 [63], then in 1973 Padamsee *et al.* derived a set of functions - collectively referred to as the "α-model" - to describe the heat capacity in the superconducting state for a wide range of $2\Delta/k_BT_c$ values [64]. A selection of these is shown in Fig. 1.8.

Note that coupling values below $\sim$ 3.4 are "not physical" in isolation since they fall below the weak-coupling limit of BCS theory. However,

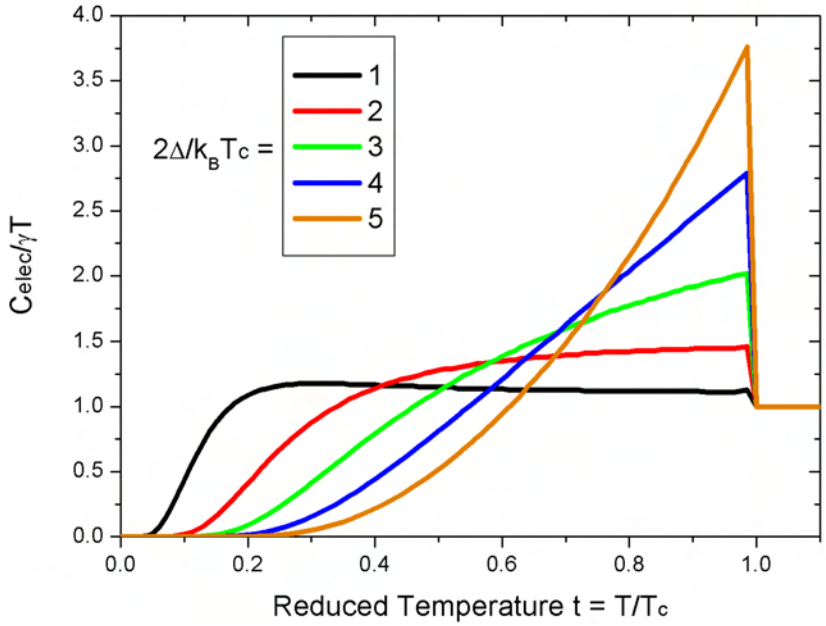

Figure 1.8: Normalised electronic heat capacity for an isotropic BCS s-wave superconductor for $2\Delta/k_BT_c$ values ranging from 1 to 5. Curves are calculated following ref. [64].

they are nevertheless useful for analysis in multi-band superconductors since within the non-zero interband scattering limit, T_c must be the same for each band. MgB_2 provides a good example of this, since superconductivity in the strongly-coupled 2D σ-band induces weak superconductivity in the 3D π-band with a bulk T_c of 39 K. The σ-band has $2\Delta/k_BT_c$ = 4.4, whereas the π-band has $2\Delta/k_BT_c$ = 1.2. Early specific heat measurements rapidly identified an anomalous bump in the electronic heat capacity at low temperature; Bouquet *et al.* showed that this could be described by a superposition of two heat capacity contributions with $2\Delta/k_BT_c$ values corresponding to the condensation energies Δ_0 for each band and the bulk T_c [65]. The fits from this work are shown in Fig. 1.9.

This procedure has been successfully employed in the clathrate superconductor Ba_8Si_{46} to detect a small second gap with effective coupling $2\Delta/k_BT_c$, contributing no more than 10% of the total density of

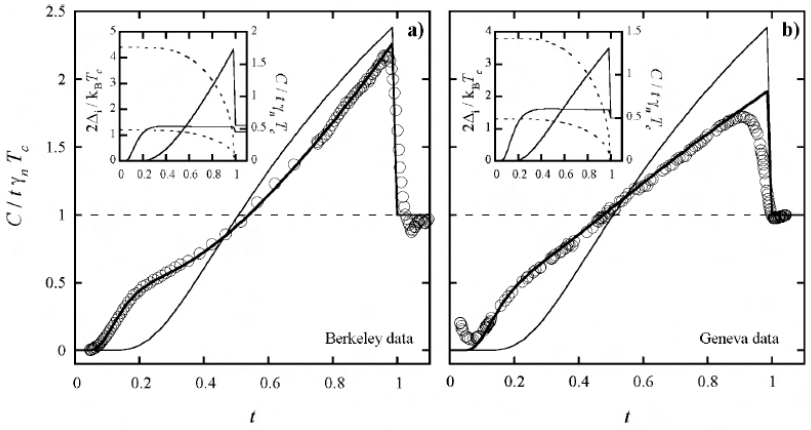

Figure 1.9: Two-band fits using the α-model for two MgB_2 samples (taken from ref. [65]). Left: 55% $2\Delta_1/k_BT_c$ = 4.4, 45% $2\Delta_2/k_BT_c$ = 1.2. Right: 50% $2\Delta_1/k_BT_c$ = 3.8, 50% $2\Delta_2/k_BT_c$ = 1.3. This sample is clearly dirtier, as can be seen from the broadened transition and the fact that the two gap values are starting to approach each other as expected for the dirty limit in two-band superconductors.

states [66]. Just as in MgB_2, the presence of the second gap increases the T_c (8 K) of this compound comfortably beyond that of the similar single-band $Ba_{24}Si_{100}$ (1.5 K).

Heat capacity measurements also give us direct acces to the entropy - thermal disorder - of a material, which is a powerful tool both for characterising samples and understanding phase transitions. The thermal entropy of a material S at temperature T_0 is defined as

$$S(T_0) = \int_0^{T_0} \frac{C(T)}{T} dT \tag{1.12}$$

Now, the entropy of a superconducting material in the normal state (above T_c) must be the same regardless of whether the material is allowed to undergo a superconducting transition at low temperature. For each graph in Fig. 1.10, the total area covered by pink and blue shaded zones must be identical otherwise entropy would not be conserved. This implies that the red and blue shaded zones must have equal areas for a given $C(T)/T$ curve.

In practice, we can only measure down to 350 mK at best. For su-

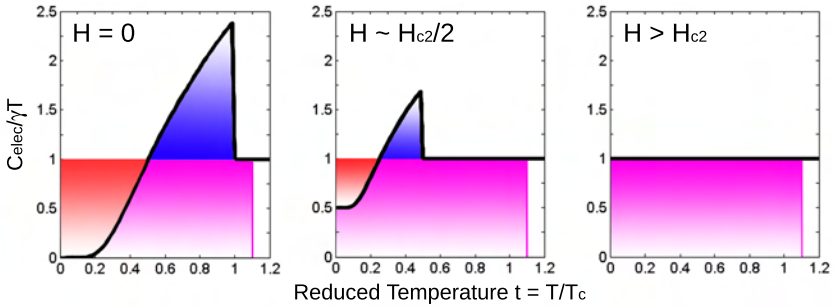

Figure 1.10: Entropy conservation illustrated by simulated BCS s-wave electronic heat capacities for a weakly-coupled superconductor in magnetic field H = 0 (left), $H \sim H_{c2}/2$ (centre) and $H > H_{c2}$ (right).

perconductors with low-lying phonon energies, it may be difficult to correctly model the lattice specific heat. In this case, if the material in question also has a high upper critical field then it will not be possible to accurately extract the electronic heat capacity below the critical temperature $T_{c2}(H_{max})$, where H_{max} is the highest field applied. However, by extrapolating the heat capacity using a known model (see section 1.2.3) and verifying whether the fit conserves entropy, we may still be able to draw conclusions on the properties of our sample. Similarly, we may also use entropic considerations to detect whether there are any "normal" electrons left in the sample at T = 0, which would be indicative of either a non-superconducting band at the Fermi level or an inhomogeneous sample with a parasitic non-superconducting impurity phase.

1.2.3 Gap symmetry

Just as is the case for STM spectra, s-wave and d-wave gap symmetry produce characteristically different behaviours for the low-temperature electronic heat capacity. An excellent example of this may be seen in the κ-ET$_2$ 2D organic superconductor family, where recent work has yielded conclusive evidence for a d-wave order parameter [67].

The problem with this method is that history tells us it can be surprisingly difficult to distinguish between exponential and power-law trends at low temperature. This is exacerbated by the fact that we are unlikely to be dealing with a clear-cut choice between isotropic single-band s-wave and textbook d-wave behaviours: real materials may ex-

hibit multi-band or anisotropic s-wave behaviour that is different to distinguish from d-wave in this experimental configuration.

However, heat capacity measurements offer us an alternative and more reliable means of discerning the gap symmetry. In the mixed state, as the magnetic field increases more and more vortices pile into the superconductor. For an s-wave superconductor the Sommerfeld constant γ should vary linearly with the field, reaching its normal-state value at $H = H_{c2}$. In contrast, Volovik calculated that for d-wave materials $\gamma(H)$ should vary as $\sqrt{H}$ [68]. It is considerably easier to differentiate between linear and power-law behaviour than power-law and exponential trends and hence $\gamma(H)$ is an excellent probe for gap symmetry. Multi-band order parameters with dissimilar coherence lengths are expected to manifest themselves as a kink, since the band with the lower H_{c2} will be the first to be populated with vortices.

In principle, $\gamma(H)$ can also be measured using an STM since γ is proportional to the spectral zero-bias conductance (ZBC). Therefore, by increasing the field and performing small spectral maps ($\sim 5a_0 \times 5a_0$ where a_0 is the vortex lattice parameter) over the same surface zone, a field-dependent ZBC value could be obtained. However, there are three potential pitfalls here. Firstly, it is necessary to remove the vortex core zones from the map before calculating the average ZBC. Not only is it unclear how to precisely define the radius of a vortex, but certain materials also exhibit a field-dependent coherence length $\xi(H)$. Secondly, any surface impurity layer or normal-metal tunnelling channel will have an additional contribution to the zero-bias conductance whose field-evolution is not evident. Thirdly, pinning barriers may create local variations in the vortex density which would affect the measured zero-bias conductance in an unpredictable fashion. For these reasons, it is safer and more accurate to measure $\gamma(H)$ by examining the field-evolution of the specific heat $C(H)$ at the lowest possible temperature (350 mK in our equipment).

1.2.4 Normal and mixed-state phase transitions

Within the mean field theoretical limit, a superconductor should exhibit a perfect second-order phase transition at T_c, i.e. a vertical jump in its zero-field heat capacity. However, this is never achieved in the laboratory for a variety of reasons. The most obvious extrinsic broadening effect arises from small variations in T_c due to sample inhomogeneities; this is a problem which can generally be remedied by improved crystal-growth techniques. Intrinsic broadening effects are altogether more

subtle and of greater interest to the physicist.

Thermal fluctuations of the order parameter become important close to T_c and also tend to broaden the transition. These fluctuations take place over the lengthscale of the superconducting coherence length ξ and hence become more disruptive in small coherence-volume materials. Dimensionality also plays an important rôle: fluctuations become increasingly important in low-dimensional systems as there are fewer directions in which to dissipate their effects. Transition temperatures may be suppressed due to the reduced spatial degrees of freedom; in the perfect one-dimensional limit a thermodynamic phase transition becomes impossible to achieve due to the collective nature of any fluctuation, however small.

It is important to note that these comments are not exclusive to superconducting transitions, but also hold for other phase transitions, e.g. ferromagnetism or charge density wave order. The coherence length is replaced by a characteristic correlation length of the new order parameter, but the fluctuation effects remain the same. This will be of particular importance when we discuss the metal-insulator transition in $M_2Mo_6Se_6$ in chapter 5.

The waters become still murkier when a magnetic field is applied. For a type-II superconductor, a "finite-size effect" occurs whereby the vortex-vortex separation limits the divergence of the coherence length at $T_{c2}(H)$ [69]. This reduces the effective coherence volume and broadens the transition still further. At high fields, this effect can be considerable and care is required to correctly analyse the heat capacity in the neighbourhood of the transition. In chapter 7 we will encounter an excellent example of a weakly first order vortex melting transition being almost completely masked by fluctuations from the neighbouring superconducting transition at high fields.

Chapter 2

Experimental Equipment

To Buy or to Build? That is the question which many experimental physicists find themselves pondering at the beginning of a major project. "Off-the-shelf" equipment - such as the Quantum Design PPMS^{TM} described in section 2.3 - offers fast and reliable performance with an almost "plug & play" approach to measurement. However, budget and samples permitting, any researcher around the world can perform the same measurement using the same equipment, thus leading to increased competition and a rapid data saturation. Furthermore, the range of more adventurous experiments currently possible with ready-built equipment is rather sparse. In particular, it is not possible to purchase a low-temperature high-field STM: almost all the spectroscopic data presented in chapters 6-8 was taken at temperatures below 1 K and without measurements in this temperature range our experimental conclusions would have been severely limited.

An additional advantage gained by building one's own equipment is the deep knowledge and intimacy acquired during both construction and operation procedures. This is invaluable when the equipment breaks down - as ⋆all⋆ cryogenic equipment does on at least one occasion during its lifetime - and the user is able to identify and solve the problem himself, rather than being faced with a mysterious black box and a series of desperate phone-calls to the manufacturer on the other side of the globe. Despite this inconvenience and the potential lack of performance compared to home-built equipment, many scientists choose to wield the chequebook for instant data gratification rather than toil for up to several years in the pursuit of a truly unique and powerful facility.

Since there should be no sacrifices in the pursuit of excellence, we have developed our own highly-specialised scanning tunnelling microscope facility for local probe measurements, at considerable expense - both temporal and financial - but with results which merit the effort. For our parallel bulk thermodynamic measurement program, we have combined ultra-high-precision relaxation calorimeters (built by Rolf Lortz in Geneva and Albin Demuer in Grenoble) with standard Quantum Design calorimeters for the optimal mix of accuracy and speed of use. All additional sample characterisation was performed in the PPMS^{TM} for convenience, except for two brief magnetic measurements detailed in chapter 7.

2.1 Aurora: A New Helium-3 High-Field STM

Over the past five years, our primary focus has been the design and construction of a new STM. The original design concept was for an ultra-low temperature rapid-access facility, intended for use on quasi-1D organic Bechgaard superconductors as well as quasi-1D molybdenum cluster compounds. Over the years the design brief and research foci have changed, but the core of the system - a single-shot helium-3 refrigerator with a vacuum sample space sitting in a liquid helium bath - has remained the same.

2.1.1 Cryogenic system

There are two excellent reasons to perform spectroscopic measurements at the lowest possible temperature. Firstly, some of the most interesting physics only occurs at very low temperature - many exotic materials (e.g. quasi-1D organic Bechgaard salts and heavy fermion materials) only become superconducting below 1 K. Secondly, thermal broadening is the principal limit to spectroscopic resolution when performing scanning tunnelling spectroscopy (STS) on low-T_c superconductors. As an example, consider the theoretical spectra shown in Fig. 2.1. For a double-gap BCS superconductor with T_c = 14 K, there is a negligible difference between spectra at 0 K and 0.3 K, compared with a significant variation between spectra measured at 0.3 K and 5 K (the typical base temperature for a commercially-available helium-4 STM). No trace of the smaller gap remains visible to the naked eye at 5 K and the V-shaped form of the spectrum is in fact rather reminiscent of that expected to result from d-wave gap symmetry (see section 1.1.3). This

potential confusion is further accentuated by the fact that the superconducting gap grows in amplitude as the temperature is reduced.

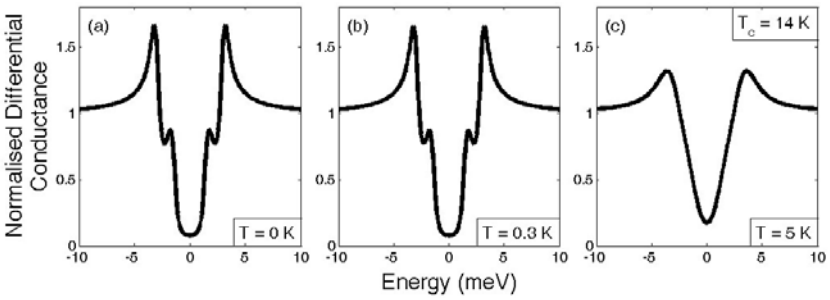

Figure 2.1: Simulated theoretical spectra at (a) absolute zero, (b) 0.3 K and (c) 5 K for an isotropic BCS double-gap superconductor with T_c = 14 K, including thermal broadening, Gaussian blurring from the lock-in amplifier and finite quasiparticle lifetime effects. Δ_1 = 3 meV and Δ_2 = 1.5 meV for the large and small gap respectively; $\sigma_{lock-in}$ = 0.2 meV; Γ = 0.15.

Although spectra may be partially compensated for thermal broadening by deconvolving with the derivative of the Fermi function at the experimental temperature, it is clear that there is a significant loss in detail within the crucial low-energy region inside the superconducting gap for the spectra taken at 4.2 K. For systems with complex order parameters (e.g. partially anisotropic gaps [50]) or other unconventional properties (e.g. an energy-dependent quasiparticle scattering rate Γ [70]), it is therefore critical to measure at the lowest temperature accessible to accurately evaluate the physical properties of the material.

The advantages of sub-Kelvin measurement are hence clear; however they are offset by technical difficulties inherent to low-temperature physics. Three principal methods exist for cooling materials below 1 K: adiabatic demagnetization (AD), dilution refrigeration (DR) and helium-3 refrigeration and an excellent review of their principles of operation may be found in reference [71]. Combining AD and DR provides the lowest possible temperatures (of the order of 1 mK) but is prohibitively complicated as well as financially demanding. The high still pumping rate necessary throughout the operation of a DR adds further difficulties due to significant mechanical vibrations being transmitted to the mixing chamber and cold finger.

A helium-3 fridge cannot reach such low temperatures as a DR or AD system, with the minimum temperature at the helium-3 pot in our system recorded as 219 mK. However, as can be seen from Fig. 2.1 there is little difference between the predicted spectra at zero and 300 mK for a superconductor with T_c = 7 K. The two materials principally studied in this work have T_cs of 14.2 K ($SnMo_6S_8$) and 14.9 K ($PbMo_6S_8$); the tiny increase in resolution which would be obtained by measuring in a DR is therefore greatly outweighed by the ease of use and low noise of a helium-3 fridge.

The cryostat and fridge used in this work were custom-built to our specifications by the Janis Research Company Inc. of Wilmington, Massachusetts. An annotated diagram of the system may be seen in Fig. 2.2. The basic principle of a helium-3 fridge is to pump on a small volume of helium-4 liquid (obtained from the main helium bath), reducing the pressure above it and hence cooling it evaporatively to around 1 K. Thermal contact with the 1 K pot is used to condense helium-3 gas (stored in a closed circuit), resulting in helium-3 liquid collecting at around 1.6 K in the helium-3 pot. When all the helium-3 in the reservoir has been condensed, a low-noise charcoal pump is used to evaporatively cool the helium-3 pot to below 300 mK.

Low-temperature STM environments can loosely be divided into 3 types: exchange gas, high vacuum and ultra-high vacuum (UHV). Exchange gas systems are difficult to implement below around $\sim$ 1.5 K since the helium gas used for thermalisation condenses on the cold walls of the experimental chamber. UHV chambers offer the cleanest sample environment and are the only viable choice for measuring oxygen-sensitive materials (such as high-T_c cuprates). Unfortunately, they are extremely expensive to set up and time-consuming to run due to the prolonged baking/pump-down periods every time the chamber is opened for maintenance. High-vacuum systems offer speed and ease of use, together with a relatively clean environment which (although unable to rival UHV) minimises the surface reconstruction risks associated with exchange gas STMs. Since Chevrel Phases are not oxygen-sensitive and were not previously known to display any ageing effects, the decision was therefore taken to measure in a high-vacuum environment. A brass tapered grease seal located just above the charcoal pump holds a hybrid copper/stainless steel inner vacuum can (IVC) in place. The IVC is evacuated to $\sim 10^{-6}$ mbar using a turbomolecular pump outside the dewar prior to cooldown; once cold the insert is cryopumped to a base pressure of around 10^{-8} mbar.

An important feature of our system is the fibre-glass sliding seal.

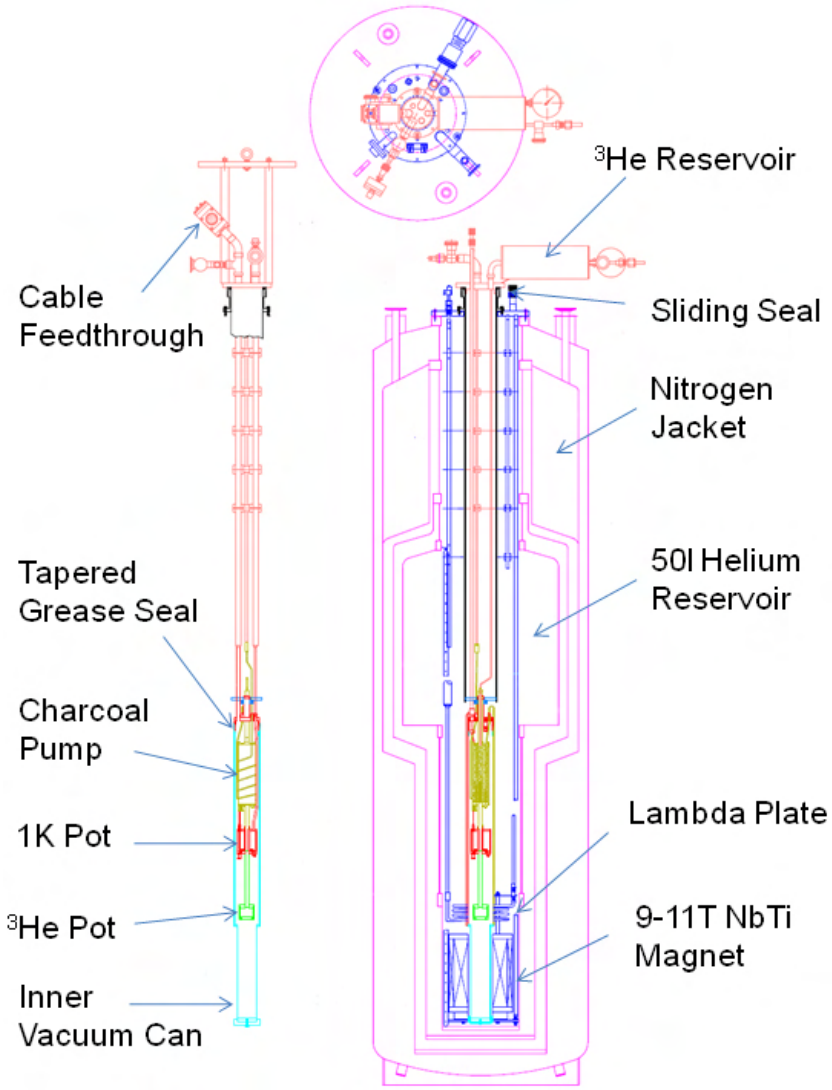

Figure 2.2: Cryogenic insert (left) and magnet dewar (right), viewed from side and above. The dewar is roughly 2 m tall.

Used in conjunction with a high precision vector motor-driven winch (manufactured by Thern Inc. of Winona, Minnesota), the sliding seal

allows the helium-3 insert to be gradually cold-loaded into the helium bath, hence minimising helium boil-off. It is important to maintain a backflow of helium-4 gas through the 1 K pot and charcoal pump pick-up lines during insertion, to prevent any blockages from ice formation. Once the helium-3 fridge is fully inserted the cool-down procedure is straightforward: the helium backflow is switched off and both the 1 K pot needle valve and charcoal pump flow line are opened. Pressure from the main helium bath cools the charcoal pump to a preset 40 K (regulated by a 25 Ω heater controlled by the amplified analogue output of a Lakeshore Model 340 temperature controller): it is important not to allow the charcoal to cool further since this will result in it absorbing helium-3 gas and reducing cooling power at the helium-3 pot. However, the principal source of refrigeration power comes from pumping on the 1 K pot with a low-noise BOC Edwards RV12 12 m^3/h rotary vane pump.

The temperature at the helium-3 pot reaches 1.6 K around 10 hours after inserting the fridge, although it can take up to 16 hours to fully thermalise the STM. At this point the system is held at 1.6 K for at least 90 minutes in order to completely condense all the helium-3 in the reservoir (6 litres at room temperature and 165 psi). A pressure gauge on the reservoir enables us to verify that condensation has taken place, as well as providing a handy facility for leak-checking. Once the system is at base pressure the charcoal pump heater is switched off and the flowline fully opened to cool the charcoal to 4.2 K. When cold, the charcoal strongly absorbs helium-3 gas and thus acts as a highly efficient pump on the condensate in the helium-3 pot. The condensate temperature drops below 300 mK after approximately 1 hour and stays cold for up to 6 days without any further intervention.

Two thermometers are located on the helium-3 pot, a ruthenium oxide chip for use below 20 K and a Lakeshore Cernox which functions up to 350 K. A second 25 Ω heater allows temperature regulation with millikelvin stability using the main control loop of the Model 340. There is a weak thermal link between the 1 K pot and helium-3 pot: to minimise helium-3 temperature (around 240 mK), it is therefore necessary to pump continuously on the 1 K pot. However, this results in a small increase in low-frequency ($\leq$ 25 Hz) vibrations, largely due to the superfluid/normal fluid interface inside the 1 K pot.

A Niobium-Titanium superconducting magnet with 2.5" bore is located at the bottom of the helium bath. At the standard bath temperature of 4.2 K a maximum field of 9 Tesla may be applied. However, by pumping on the bath with a lambda-point refrigerator situated just

above the magnet it is possible to reduce the temperature to below 2.2 K and hence increase the maximum field to 11 T. Allen-Bradley carbon resistors situated above and below the magnet allow the helium temperature to be verified during pumping and hence reduce the risk of a magnet quench at 11 T. It is necessary to refill with liquid helium once a week during normal measurement, or once every five days if pumping on the lambda plate. This long hold-time enables extended spectroscopic imaging over a large area, which proved invaluable to the vortex investigations which will be detailed in Chapter 7.

2.1.2 STM head units: design and thermalisation

The concentric-tube design of the Geneva STM [72, 73] and its retro-compatible XY micro-positioning table [74] have been well-documented in numerous texts. By applying a high-voltage cycloid to the z electrode, the external 1/2" diameter piezoelectric translator tube is used as an inertial slip-stick motor, driving a sample-mount "chariot" up a pair of polished sapphire rails towards the STM tip. The internal 1/4" scanner tube both sweeps the tip across the sample surface and regulates its height during measurement. However, Aurora is a unique facility in allowing users the choice of two different head units: an ultra-low-noise shielded version for ultimate measurement sensitivity or an XY STM with micro-positioning table. Diagrams of each head unit together with schematics of the different paths taken by the tunnel current are shown in Fig. 2.3.

The high-resolution head unit eliminates any capacitative coupling between the z-scanner and the tunnel current by grounding the single electrode on the interior of piezoelectric scanner tube. Instead, all scanner electrodes are sited on the outside of the tube. This reduces the scan range of the STM to around 1.6 $\times$ 1.6 μm at 400 mK, but removes the risk of any noise transmission from the high-voltage supply which drives the piezos (a known problem with the concentric-tube design).

The XY STM comes into its own when measuring small ($<$ 1 mm^2 surface) samples. Prior to measurement, the tip is manually positioned above the sample outside the cryostat and a "coarse approach" is performed to get the tip within $\sim$ 100 nm of the surface. It is already difficult to position the tip above a clean 1 mm^2 sample zone; now consider that a similarly-sized cleaved quasi-3D sample may only exhibit optically flat zones of size 100 $\times$ 100 μm and accurate tip placement rapidly becomes a nightmare. An XY table allows precise manipulation

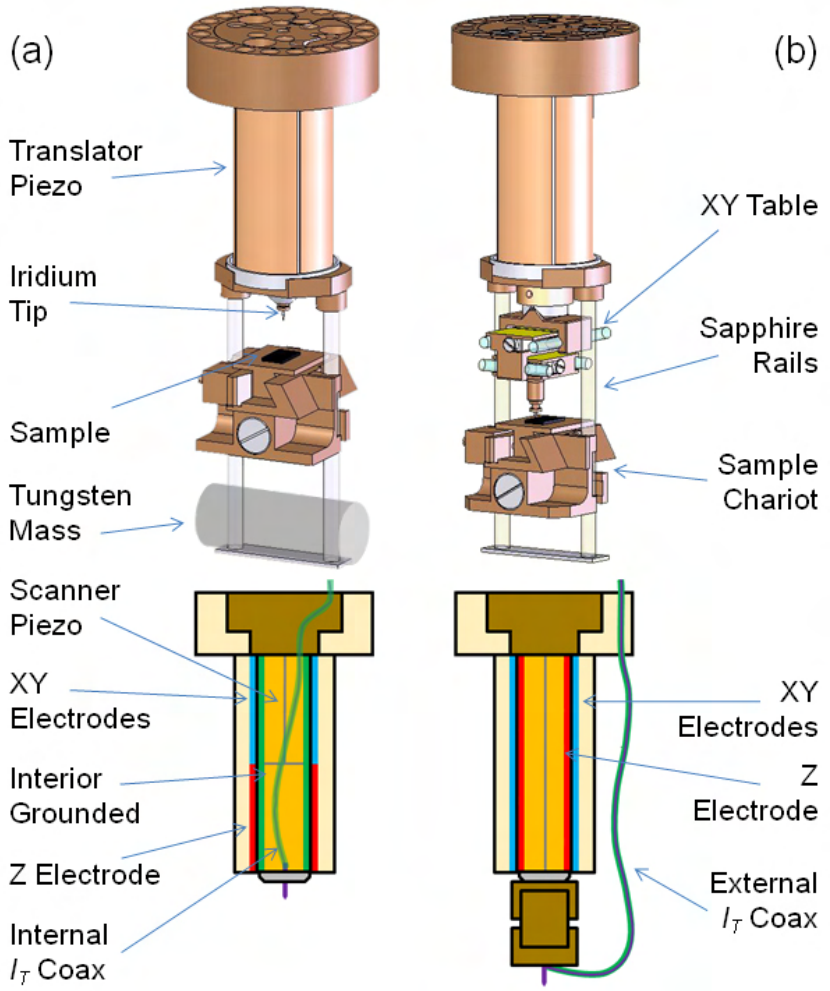

Figure 2.3: STM diagrams (above) and tunnel current path schematics (below) for (a) high-resolution head unit and (b) XY-table head unit. XY-Scanner electrodes are denoted in blue, z-scanner electrodes in red and grounded components in green.

of the tip position to within several microns, for example permitting tunnelling into a 15 μm early pnictide single crystal during testing. The incorporation of this table does have several minor disadvantages: the

base noise level is marginally higher than in the high-resolution head unit since the relative exposure of the tunnel current coax renders it slightly more susceptible to electromagnetic pick-up (particularly 50 Hz noise). However, this is largely eliminated by the shielding from the IVC. There is also a slight risk of mechanical noise from scanner-table coupling, although this can normally be controlled by maintaining a high tension on the CuBe leaf-springs in the table.

In the Chevrel phases, $PbMo_6S_8$ single crystals are typically much smaller than $SnMo_6S_8$ due to increased difficulties in the growth process. For this reason, all measurements on $PbMo_6S_8$ were carried out using the XY STM, whereas $SnMo_6S_8$ was exclusively studied with the high-resolution version.

It is clearly desirable to be able swap head units quickly and easily, to avoid down-time between measurements. However, a problem arises when measuring in a magnetic field: the field is only homogeneous over a sphere of 1 cm diameter and the tip must therefore fall within this sphere to avoid any field gradients and the mobile vortices which would ensue. Achieving this is not immediately obvious since not only does each head unit have a different mass, but the tip is located approximately 15 mm lower in the XY STM due to the space occupied by the XY table. The solution to this is twofold: firstly the design of the XY table has been modified to remove as much weight from it as possible (mainly by drilling holes in it wherever structurally feasible). Secondly, a small tungsten mass of carefully calibrated weight has been machined to slot into the base of the sapphire rails below the sample chariot of the high-resolution STM, thus increasing its mass. These steps combine to ensure that the STM tip is always located at the centre of the magnetic field, regardless of which head unit is in use.

We use iridium tips for all measurements. There are two basic requirements for a tip: it must be mechanically stable and have a flat density of states close to the Fermi level with a quasi-isotropic Fermi surface. Iridium is a hard d-band metal which fulfills these requirements; tungsten would be another option but tends to suffer from oxidation. Tips are sharpened by electrochemically etching in a calcium chloride/hydrochloric acid solution before screening under an optical microscope.

Adequate thermalisation of a sub-Kelvin STM is a considerable challenge. On one hand the head unit needs to be mechanically isolated from the helium-3 pot in order to limit vibration transmission; on the other hand it is vital to provide a strong thermal link between pot and STM. A photograph of our experimental solution to these requirements

is shown in Fig. 2.4. Mechanical isolation is achieved by a 20 mm diameter CuBe spring, clamped to the bottom of the helium-3 pot with a silver plate and CuBe screws, with further silver hardware attaching the spring to the STM. The dimensions of this spring have been optimised to minimise its resonant frequency: 1.7 Hz. A 24mm diameter copper cage is silver-soldered to the plate, ensuring that while the spring can still move freely, the STM cannot swing violently and hit the IVC walls while the insert descends into the dewar. It should be noted that even with this cage in place, extreme care is still needed whilst loading the insert into the dewar. Without the low-speed vector controller on the Thern winch it would be impossible to lower the insert sufficiently smoothly to avoid jolting the STM into the IVC. Any such violent shocks to the STM knock the chariot down the sample rails, distancing the tip from the sample and rendering any measurement impossible.

The majority of the heat transfer takes place through the 18 125 μm ultra-high purity (99.999%) kapton-insulated silver wires used to control the STM. In order to avoid heat-leaks to the walls of the IVC, these wires are wrapped around the bars of the copper cage. To minimise the heat load, the silver wires are replaced by low thermal conductivity insulated manganin at thermalisation junctions bolted to the bottom of the helium-3 pot. The tunnel current is carried by a stainless steel/copper flexible micro-coax, which is thermalised to the helium-3 pot using a copper bobbin. The STM temperature is measured using a calibrated Lakeshore Cernox thermometer (CX-1010) sited right next to the STM tip, attached using thermally conductive epoxy to the carobronze piece between translator tube and sapphire rails.

The proximity of the STM to the walls of the inner vacuum chamber (typically at 4.2 K) and the fact that the ultimate vacuum attainable is at best only $\sim 10^{-8}$ mbar means that the minimum temperature reached at the STM tip is only 400 mK. Tests showed that larger diameter wires brought this temperature down to 300 mK, but with the side-effect of increasing mechanical noise. Pumping on the lambda plate to reduce the main bath temperature below 2 K also has a small effect on the base temperature, but also increases vibration level. Nonetheless, as we will see 400 mK is a perfectly adequate measurement temperature for Chevrel phase superconductors.

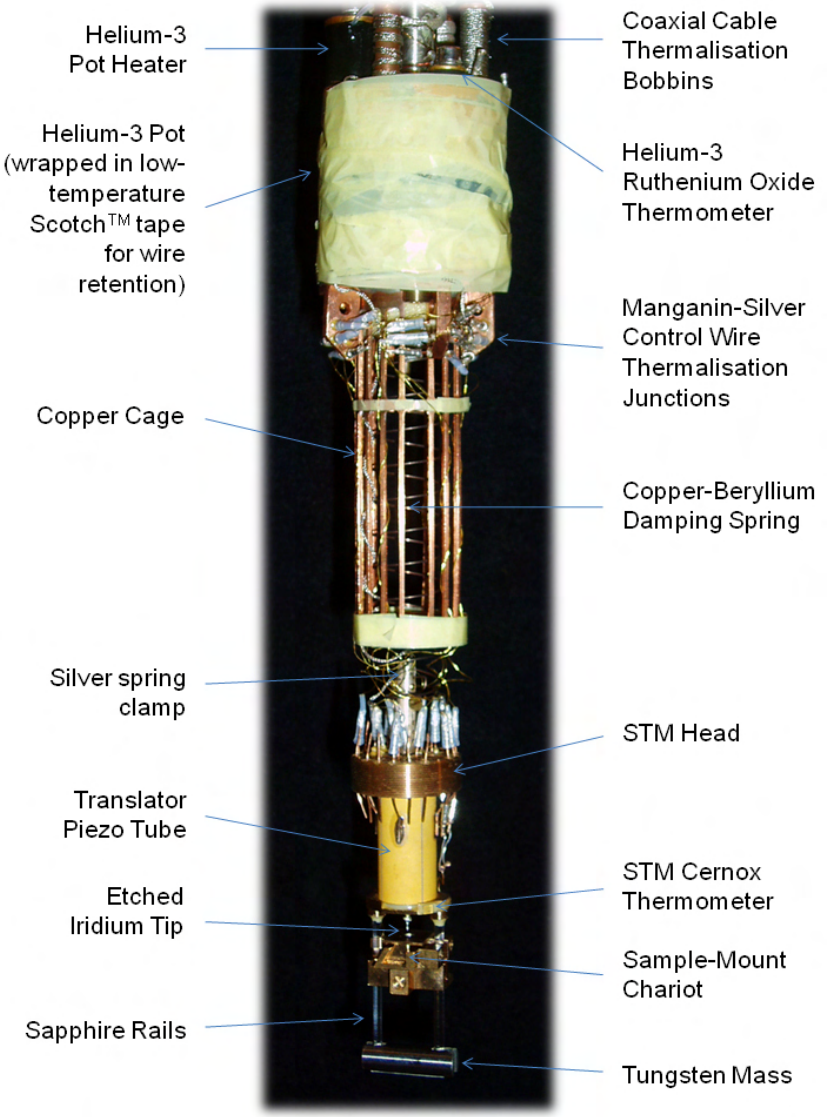

Figure 2.4: High-resolution STM head unit suspended from the base of the helium-3 pot.

2.1.3 Calibration

Prior to use, it is necessary to calibrate the voltage-displacement coefficients for the piezoelectric scanner tubes over the full experimental temperature range envisaged (400 mK - 300 K). XY and z scanners are calibrated separately using different reference samples: for the XY procedure we use a commercially-available Nanogrid. This is basically a gold-coated silicon matrix with a topographic periodicity of 160 nm; we therefore obtain large-scale topographic images (though do not approach the limits of the $\pm$150 V high-voltage power supply since non-linearities may occur here) and perform a 2D Fourier transform to accurately measure the periodicity. For z calibration we use a freshly-grown Au(111) on mica sample from our collaborators at Phasis [75] with a known c-axis lattice parameter of 2.36 Å. Typical STM images of such thin films display a large number of clean topographic steps, with a variety of different heights. The lowest common multiple of these step heights corresponds to a single unit cell, i.e. 2.36 Å. Several examples of the images obtained during calibration are shown in Fig. 2.5.

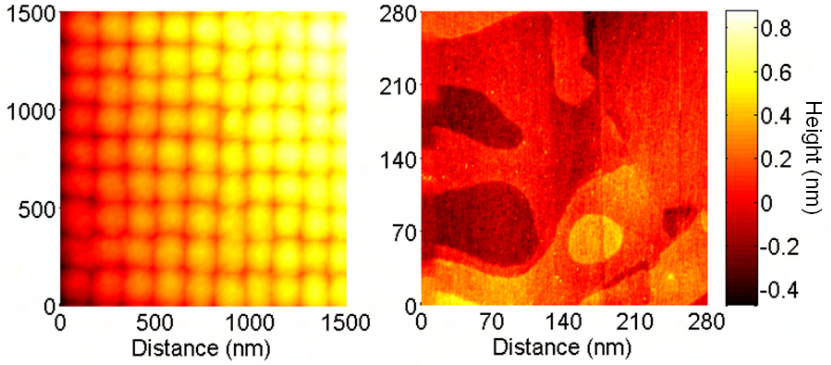

Figure 2.5: Examples of calibration measurements taken using the high-resolution STM head unit. Left: 1500 $\times$ 1500 nm nanogrid topography. Right: Atomic-scale unit-cell steps on freshly-deposited Au(111).

2.1.4 Control electronics, data acquisition & noise

An high-performance new in-house electronics module has recently been developed for STM control [76] and a schematic is shown in Fig. 2.6.

We predominantly measure in constant-current mode and the basic purpose of this module is therefore to maintain the tunnel current at a preset value I_0. This is achieved by regulating the voltage supplied to the z scanner within a negative feedback loop.

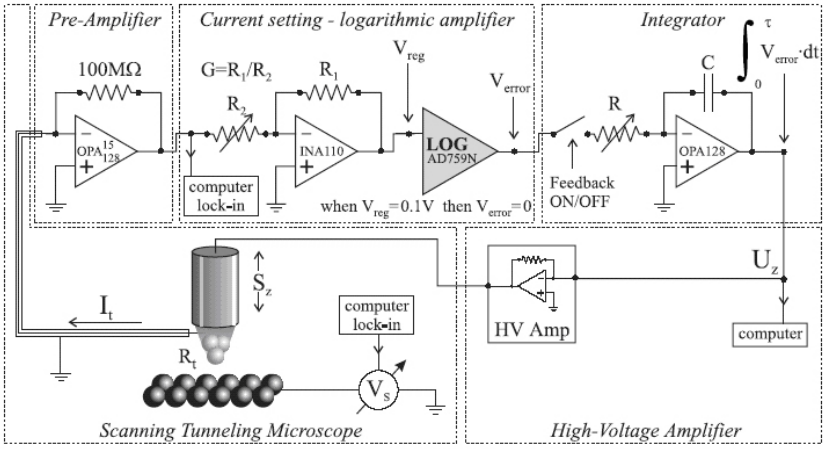

Figure 2.6: Schematic diagram of the analogue feedback circuit for z regulation in the STM control module.

A bias voltage is applied to the sample and a tunnel current I_t flows between sample and tip. Upon exiting the top of the cryostat, this current immediately enters a preamplifier which converts it into a voltage. It is then transferred in a double-shielded coaxial cable from cryostat to electronics module, where it enters a logarithmic amplifier. Since I_t is exponentially dependent on the tip-sample separation (see eq. 1.1), the logarithmic amplifier linearises this dependence. At this stage, the signal is also compared with the reference current I_0 and the amplifier output is proportional to the difference between I_t and I_0. An integrator circuit sums this error signal over time, with the output being sent to the z scanner channel of the high-voltage power supply. The time-constant of this integrator output is manually adjustable, thus allowing the z response to be optimised depending on the source of the noise in I_t and its characteristic frequency.

Let us consider the procedure for spectroscopic measurements in greater detail. Although it is possible to perform spectroscopy by taking the numerical derivative of $I(V_b)$ curves, this method is highly susceptible to noise and requires extensive averaging to obtain a clean signal,

particularly at the low energy scales ($<$ 5 meV) which are of interest in the Chevrel phases. Instead we use a lock-in technique to extract $\mathrm{d}I/\mathrm{d}V_b$ from a noisy background: although a single spectrum takes longer to acquire than an $I(V_b)$ curve, the requirement to average a large number of spectra is greatly reduced and minor features at low energy (such as a second superconducting gap) remain prominent. The bias voltage is modulated by a small AC signal V_{LI} from a Stanford SR830 lock-in amplifier:

$$V = V_b + V_{LI}\cos(\omega t) \tag{2.1}$$

The frequency $\omega = 2\pi f$ must be carefully chosen to lie comfortably above the z scanner feedback response. However, it should neither exceed the preamplifier bandwidth ($\sim$ 2 kHz), nor be a multiple of 50 Hz: we typically use 840 Hz while measuring. The tunnel current is now a function of $V_b + V_{LI}$,

$$I_t(V) = I(V_b + V_{LI}\cos(\omega t)) \tag{2.2}$$

which we expand in a Taylor series as

$$I_t(V) = I(V_b) + \left.\frac{\partial I_t}{\partial V}\right|_{V_b} V_{LI}\cos(\omega t) + \frac{1}{2}\left.\frac{\partial^2 I_t}{\partial V^2}\right|_{V_b} V_{LI}^2\cos^2(\omega t) + \ldots \tag{2.3}$$

Now, since $\cos^2(\omega t) = \frac{1}{2}(1 + \cos(2\omega t))$ we can simplify equation 2.3 to obtain the following proportionality:

$$I_t(V) \;\approx\; \alpha_0 + \alpha_1\cos(\omega t) + \alpha_2\cos(2\omega t) + \text{higher order terms} \tag{2.4}$$

where $\alpha_n \;\propto\; \frac{d^n I_t(V)}{dV^n}$. The lock-in amplifier therefore isolates and amplifies the component of $I_t(V)$ with frequency ω, since this will be proportional to $\mathrm{d}I/\mathrm{d}V$ and hence the LDoS. Since $V_{LI} \ll V_b$, we may neglect the higher order terms of the expansion. During measurements, V_{LI} is typically set at 0.2 mV; we simulate the broadening effect this has on our experimental data by convolving our model spectra with a Gaussian of width 0.2 meV.

The data acquisition is taken care of by a 16-bit Microstar Laboratories data acquisition processor which feeds a PC interface running home-built Labview control software [77]. This highly user-friendly

interface neatly automates the sample approach procedure prior to establishing a tunnel junction, then provides a range of topographic and multi-dimensional spectroscopic modes with full control over all measurement parameters. It also incorporates several useful toolboxes such as a temperature monitor, noisemeter and file-browser.

Great care has been taken to minimise electrical noise, both inside and around the cryostat and also in the 19" racks which hold the control electronics. New filters have been fitted to the power supplies in the principal electronics module, significantly reducing the 50 Hz noise level. All electronic elements are carefully grounded to the racks and the PC interface is bolted to a grounded metal table. Both cryostat and helium-3 insert are grounded (the insert by the tunnel current coaxial shield), but the area of direct contact between them is insulated to avoid any ground loops. A dedicated filter removes high-frequency noise from the temperature controller heater output (which would otherwise be transmitted directly to the helium-3 pot). Insulated O-rings and nylon clamps isolate the two vacuum pumps, pressure gauge and helium recovery line from the cryostat and insert. Finally, the winch is a potentially dangerous source of both ground loops and RF noise and must not under any circumstances be used during measurement.

Despite all these precautionary measures, it is very noticeable that the majority of interference enters the system between the STM head and the preamplifier tunnel current input, i.e. as pick-up along the tunnel current coaxial cable. The only way to improve this is to develop a low-temperature pre-amplifier, located as close as possible to the STM tip. Unfortunately, this is not an elementary experimental challenge due to the difficulty in sourcing a transistor which still functions correctly at sub-Kelvin temperatures. An example of such a pre-amplifier exists in the literature [78] and it is hoped that whoever inherits the Aurora will follow this example and develop a similar system as soon as possible.

2.1.5 Vibration isolation

Mechanical vibrations are one of the main challenges to overcome in successful STM design. Any extraneous low-frequency tunnel current modulation will generate a spurious oscillation in the measured topography, which is an unwelcome irritation but may be removed using 2D Fourier transform filtering. However, in spectroscopic mode low-frequency noise in I_t will destroy any hope of successfully imaging the local density of states since it generates large peaks in the $\mathrm{d}I/\mathrm{d}V$ curve

at random locations (depending on the measurement timescale). It is therefore imperative to locate any STM in a quiet, vibration-free environment, as well as maximising its integral mechanical stability during the design procedure.

Early tests of the Aurora indicated significant noise in I_t at 8 Hz and 12 Hz. The vast majority of noise below 25 Hz is of mechanical origin and so two ground motion detectors (geophones) were purchased: Geospace Technologies GS-11D (vertical) and HS-1 (horizontal). In principle, a motion detector should allow us to determine the resonant frequencies of the cryogenic system and ascertain whether vibrations of the building are being transmitted through the laboratory floor. A geophone is a simple inductive velocity detector which works following Faraday's law V = -dΦ_B/dt: a small magnet is free to vibrate inside a conducting coil and the voltage V induced in the coil is equal to the rate of change of magnetic flux dΦ_B/dt. V is therefore proportional to the velocity of the magnet. A sample noise spectrum is shown in Fig. 2.7. Knowing the frequency of vibration and the magnet velocity, it is simple to calculate the vibrational displacement of the object or environment under test.

By measuring vibrations both on the laboratory floor and at the helium-3 pot, we concluded that the resonant frequency of the building is 6 Hz, the horizontal resonant frequency of the helium-3 insert is 12 Hz (which is hence excited by the 6 Hz building noise) and the cryostat also resonates vertically at 8.5 Hz. Some form of vibration damping system was clearly necessary. The most effective vibration dampers available actively cancel out noise using piezoelectric motors. However, these are prohibitively expensive (around $50,000 for a set). Passive air dampers are a much more cost-effective alternative, despite their performance generally deteriorating below $\sim$ 5 Hz (piezo systems remain functional to below 1 Hz). Given that the minimum frequency to be eliminated was 6 Hz, three Technical Manufacturing Corporation Gimbal Pistons^{TM} were purchased and incorporated into a $\sim$ 180 kg cradle for the entire cryostat. A photo of the anti-vibration system can be seen in Fig. 2.8. In order to maintain stability it is crucial that the centre of gravity of the cryostat remains below the dampers, hence the tall columns. An acoustic blanket was also wrapped around the cryostat in order to minimise vibrational pick-up from ambient noise.

Following these vibration isolation efforts, the 8.5 Hz and 12 Hz noise in the geophone readouts at the helium-3 pot were substantially reduced but did not completely vanish. This can be attributed to the fact that although the Gimbal Pistons^{TM} are able to damp out almost all

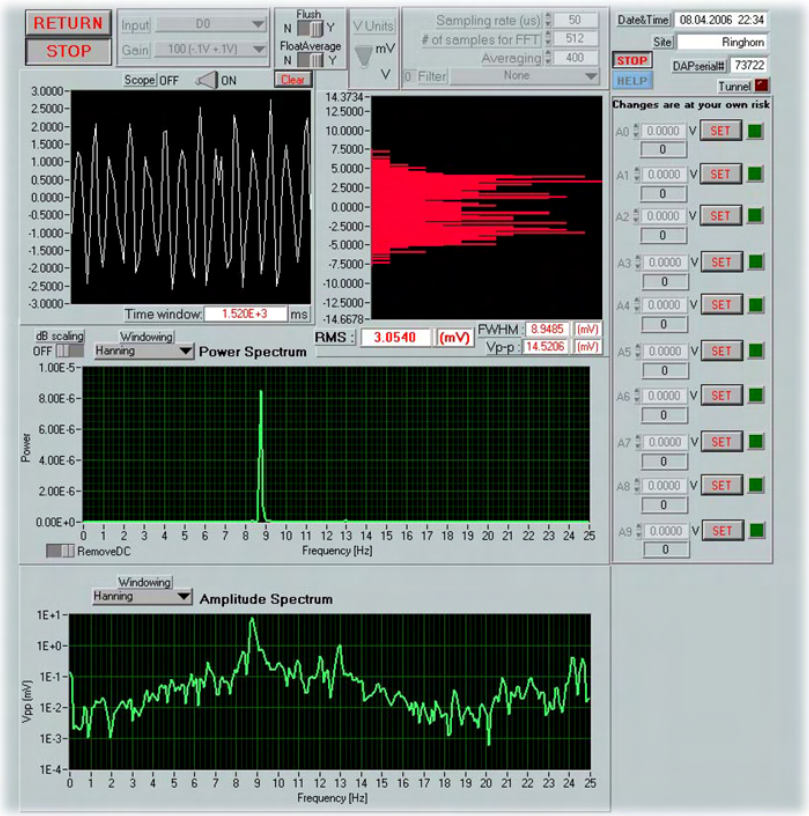

Figure 2.7: Screenshot of the Noisemeter in the STM control software, directly reading the output of the GS-11D vertical geophone mounted on the helium-3 pot. An amplitude peak may clearly be seen at 8.5 Hz.

vibrations of the cryostat (since they are directly attached to it), they are less capable of absorbing the vibrations of the helium-3 insert inside the cryostat. The insert is only weakly held in place by the sliding seal at the top of the cryostat: its long length (over 1.5 m) and relatively low weight render it particularly susceptible to vibration. In order to minimise any perturbations at the top of the cryostat, all metal pumping lines/exhaust tubes have therefore been replaced by reinforced nylon vacuum tubing which transmits very little noise, resulting in a further reduction in the noise level at the helium-3 pot.

Figure 2.8: Aurora cryostat, low-noise nylon pumping lines and anti-vibration system.

Testing has revealed a small increase in vibration amplitude below 2 Hz (the resonant frequency of the Gimbal Pistons^{TM}). However, since such low frequency noise only occurs after a direct impact to the cryostat (a generally avoidable scenario), it has no effect on measurements. Most importantly, the tunnel current oscillations which plagued early spectroscopic measurements (particularly for large I_t) have been significantly reduced, thus permitting accurate reproducible spectroscopy at higher bias voltages.

Looking into the future, further acoustic shielding from the rather noisy laboratory environment is the next logical step to continue to reduce noise levels. An ambitious project has been conceived, which aims to screen the cryostat using composite plasterboard/metal sheet walls with a sandwich layer of Green Glue^{TM} viscoelastic acoustic damping compound, as well as adding high-density foam tiles to the interior of

the screens in order to create a pseudo-anechoic chamber for the cryostat. Whilst remaining within the current laboratory setting and maintaining a realistic budget, it is difficult to envisage any further possible vibration limitation.

2.2 High-Sensitivity Relaxation Calorimeters

Three standard designs of calorimeter for specific heat measurements exist: relaxation, adiabatic and AC. Crudely speaking, the relaxation technique works by applying/removing a heat pulse to a sample, then measuring how long it takes to warm up or cool. Adiabatic calorimeters heat the sample continuously and measure the heater input power necessary for a given change in temperature. The AC method applies a small AC heat modulation to the sample and measures both the amplitude and dephasing of the sample temperature.

Each type of calorimeter has its own advantages and disadvantages. Adiabatic models provide the most accurate measurement of the absolute heat capacity of a sample and are the most sensitive to first order phase transitions, but they are only suitable for use with large samples (at least several tens of milligrams). The AC technique permits very fast measurements of samples weighing as little as several micrograms, but it is difficult to use at very low temperatures and frequently underestimates latent heats at first order phase transitions. Relaxation calorimeters are useful at all temperatures and can be tuned to detect latent heats by performing sufficiently long relaxations; however the sensitivity of a typical 25 μm version imposes a lower sample limit of around 500 μg and each calorimeter requires very careful calibration. Since $M_2Mo_6Se_6$ and MMo_6S_8 crystals typically vary in mass between 500 μg and 10 mg and our priority is accurate measurement at low temperature, we have used home-built relaxation calorimeters for our heat capacity measurements. A comprehensive introduction to modern heat capacity measurement techniques may be found in ref. [79], to which we refer readers in search of greater detail.

2.2.1 Calorimeter design

The key to successfully minimising a relaxation calorimeter is to combine the sample heater and thermometer into a single unit. A schematic of the Geneva/Grenoble design is shown in Fig. 2.9, together with a photo of a calorimeter mounted on its probe. The heart of the calorime-

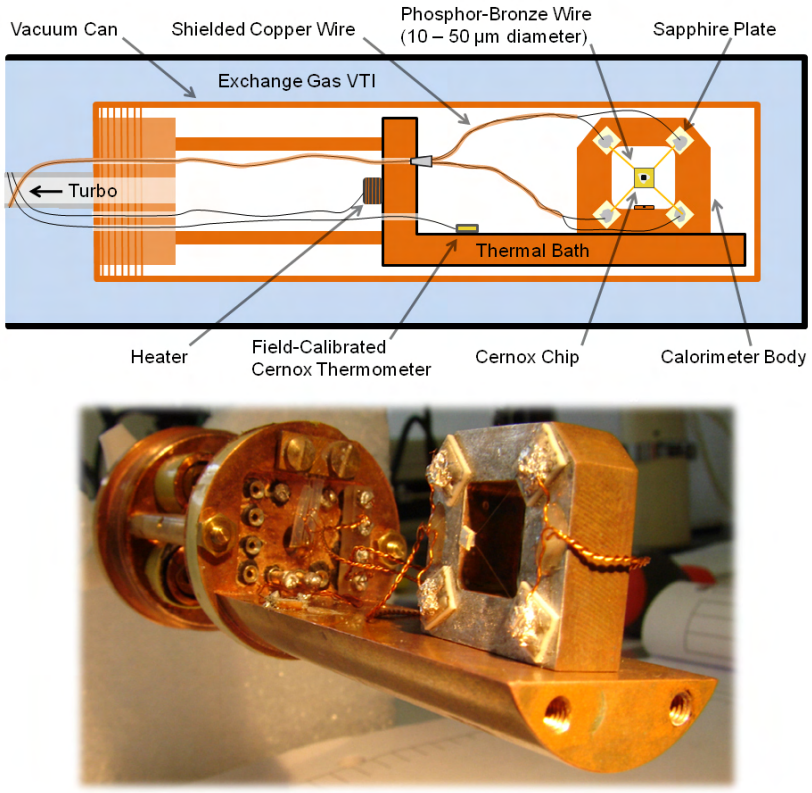

Figure 2.9: Above: Schematic of the Geneva/Grenoble relaxation calorimeter. Samples are attached to the Cernox chip using either General Electric (GE) varnish (for fragile calorimeters of wire diameter 25 μm and below) or Wakefield Thermal Compound (for 50μm calorimeters). Below: A 25 μm calorimeter mounted on its probe prior to sealing and loading into the 28 T magnet at the Grenoble High Magnetic Field Laboratory.

ter is a Lakeshore Cernox bare chip, attached by four phosphor-bronze wires to a copper thermal bath. Depending on the desired sample weight and measurement temperature range, not to mention the patience and skill of the calorimeter builder, these wires may range in diameter from 10 - 50 μm. The four wires are electrically isolated from the (earthed) copper bath, but are thermalised to the bath using sap-

phire plates. Electrical contacts to the Cernox chip are made using a viscous silver epoxy (Epo-Tek H31D), with soldered joints to shielded twisted-pair copper wires at the sapphire plates. During operation, the chip is "read" by inputting current from a Keithley 2400 power supply and measuring the voltage drop with a Hewlett-Packard 3458A digital multimeter.

The temperature of the thermal bath is controlled using a field-calibrated Cernox thermometer and a wire-wound heater. The thermal link between bath and vacuum can (which sits in helium exchange gas inside a variable temperature insert (VTI) cryostat) is relatively weak, thus allowing sub-millikelvin temperature stability with a low applied heater power and minimising the effects of temperature fluctuations in the VTI. The vacuum can is continuously evacuated using a turbomolecular pump during measurement, in order to eliminate any changes in the thermal conductivity from chip to bath due to slow leaks or outgassing.

2.2.2 Theory of operation

If a sample is mounted on the Cernox chip and a current I is passed through the chip, the temperature will rise since power $P = I^2R(T)$ is being delivered to the chip (where $R(T)$ is the chip resistance at temperature T). For a steady current I, the chip temperature will "relax" upwards until it stabilises at $T = T_\infty$. The chip and sample are now in thermal equilibrium with the bath, which is maintained at a constant temperature T_0 throughout the measurement. Since the thermal link (the four wires) between chip and bath is weak, this relaxation will typically take around 5τ. $\tau = C/\kappa$ is the system time constant, where C is the heat capacity of the sample at constant pressure and κ is the thermal conductivity between the sample and the bath.

At temperature T and time t, the chip power input is given by

$$P(t) = I^2R(T(t)) = C(T)\frac{dT}{dt} + \kappa(T)(T(t) - T_0) \tag{2.5}$$

At $T = T_\infty$ the temperature is stable, $\frac{dT}{dt}$ = 0 and hence we have

$$P(t) - P(\infty) = I^2[R(T(t)) - R(T(\infty))] = C(T)\frac{dT}{dt} + \int_{T_\infty}^{T} \kappa(T')dT' \tag{2.6}$$

In order to extract the sample heat capacity $C(T)$ by measuring $R(t)$ and employing this relation, it is necessary to calibrate the calorimeter

by precisely measuring $R(T)$ and $\kappa(T)$. The addenda from the intrinsic heat capacity of the calorimeter must also be measured (using a silver reference sample), then subtracted from the experimental data.

2.3 Quantum Design PPMS™

The Quantum Design Physical Property Measurement System (PPMS) is an audacious attempt to condense an entire laboratory into a single cryostat (together with a variety of experimental probes), controlled by a highly intuitive computer interface. While the ultimate measurement sensitivity of the instrument may not quite compare with dedicated individual measurement facilities, in the hands of a careful user the PPMS provides a fast and reliable means of accurately characterising samples, either prior to STM measurement or for independent investigations.

2.3.1 AC susceptibility

Knowledge of the magnetic susceptibility χ of a material is crucial for characterising its superconducting properties. χ is defined as the ratio of the sample magnetisation M to the applied field H; χ = M/H. The PPMS measures χ using a standard inductive method: the sample is placed at the centre of a set of detection coils and a small AC excitation field (maximum 10 Oe, typically 0.1 Oe) is applied. A small AC magnetic moment is consequently induced in the sample. Since this signal is time-varying, it in turn induces an easily-measurable voltage in the detection coils. This voltage is proportional to the magnitude and direction of the sample magnetisation M.

In the Meissner state a type-II superconductor is perfectly diamagnetic and hence χ = -1. A graph of χ vs. temperature will therefore exhibit a step at T_c. The width of this step yields important information concerning the quality of the sample. For a perfectly stoichiometric homogeneous single crystal, $\chi(T)$ should resemble a Heaviside function. However, any imperfections in the sample will result in a broader step of width ΔT_c, since different sample zones become superconducting at slightly varying temperatures. Consider Fig. 2.10 for an example: here we compare $\chi(T)$ for $SnMo_6S_8$ and $PbMo_6S_8$. Growing $PbMo_6S_8$ crystals is much more of a challenge than for $SnMo_6S_8$, since there is high potential for oxygen impurities in the precursor compounds to substitute for sulphur in the Mo_6S_8 clusters. Oxygen doping considerably suppre-

ses T_c and hence broadens the superconducting transition. In an STM measurement, this would result in the measured gap size varying over the sample surface. As well as threatening the accurate measurement of the gap, the observation of such variation could launch an awkward debate over whether inhomogeneity is intrinsic to Chevrel phases (as is the case for the high-T_c cuprates). It is therefore imperative to screen all samples by measuring $\chi(T)$ by AC susceptibility prior to any STM measurements, in order to reject any excessively inhomogeneous samples. For the highest quality single crystals available, ΔT_c is typically ~ 0.1 K in $SnMo_6S_8$ and ~ 0.3 K in $PbMo_6S_8$.

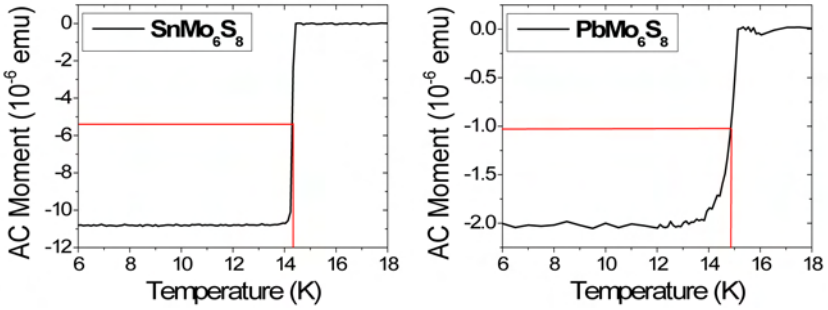

Figure 2.10: AC susceptibility curves $\chi(T)$ around the superconducting transition for (a) $SnMo_6S_8$ and (b) $PbMo_6S_8$. Excitation field: 0.1 Oe at 970Hz.

It should be noted that during low-field AC measurements in the Meissner state we are only probing the sample surface (to a maximum depth equal to the magnetic penetration depth λ), since the excitation fields used are smaller than the lower critical field H_{c1}. However, there are no competing phases in chemical proximity to either $SnMo_6S_8$ or $PbMo_6S_8$ and any substantial crystal growths are hence unlikely. The surface quality is therefore representative of the entire crystal and bulk-sensitive measurements (such as DC magnetisation performed in a SQUID magnetometer) are unnecessary.

The normal-state susceptibility also provides useful information regarding sample purity. With the exception of the magnetic Chevrel phases, clean molybdenum cluster-based compounds are weakly diamagnetic from 300 K down to low temperature, with $\chi(T)$ small, negative and constant. Any paramagnetic impurities present in samples may not necessarily reveal themselves via large values of ΔT_c, but will however produce a "Curie tail" of form $\chi \propto 1/T$ superimposed on the

susceptibility. Any upturn of $\chi(T)$ at low temperature is therefore indicative of a dirty sample.

2.3.2 AC transport

In principle, electrical resistivity is one of the easiest physical properties to measure, since following Ohm's Law it is merely the ratio of the applied current to the voltage across a sample. However, difficulties may arise at low temperatures in small highly-metallic samples with low resistivity: the current needs to be minimised in order to limit heating effects and the resulting voltage is frequently in the nanovolt range. In order to reduce experimental noise, the PPMS applies an AC current excitation and detects the resultant sample voltage using an integral lock-in amplifier. Furthermore, we employ a four-wire technique for greater accuracy, hence largely bypassing the effects of any anomalous large contact resistances. A typical quasi-1D $M_2Mo_6Se_6$ crystal prepared for a resistivity measurement is shown in Fig. 2.11: four gold contact pads of approximate thickness 2nm are first sputtered onto the sample surface, then 50 μm diameter gold wires are attached to the contact pads using a silver-loaded conducting epoxy. In this way we obtain thermomechanically stable sub-100 μm contacts with average resistance of the order of 2 Ω at 300 K. This allows the accurate and reproducible characterisation of the superconducting resistive transition for extremely small samples at temperatures down to 350 mK.

2.3.3 Specific heat

The PPMS includes two different relaxation calorimeters: an 8-wire 100 μm model for use with large crystals at high temperatures and a 4-wire 50 μm version which can measure milligram-scale samples down to 350 mK (with the PPMS helium-3 insert). Photos of each calorimeter may be seen in Fig. 2.12. Integrated software controls and fits the sample relaxations, directly outputting the heat capacity to a data-file.

The measurement principles are similar to those of our home-built microcalorimeters, except that relaxations are solely performed upwards in temperature and only the rapidly-varying part of the relaxation curve is fitted in order to save experimental time. In addition to the automatisation and ease of use, the main advantage of the PPMS system is the ease of handling the addenda contributions: the chip addenda are measured in a calibration run prior to sample mounting

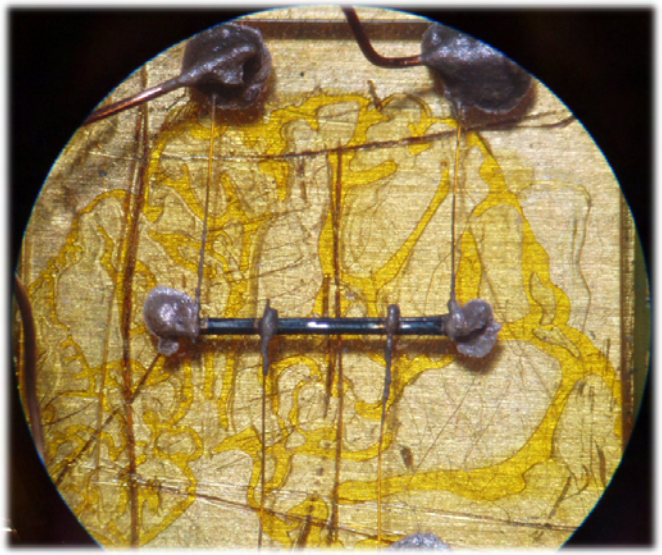

Figure 2.11: Quasi-1D $M_2Mo_6Se_6$ sample for four-wire AC transport measurement, with 50 μm gold wires attached using silver epoxy. The sample is stuck to a a clear sapphire plate using GE varnish and the orange streaks are the GE varnish used to thermalise the plate to the sample-holder. Total sample dimensions are $\sim$ 3 mm$\times$0.2 mm$\times$0.1 mm.

and automatically subtracted from the measured heat capacity. Furthermore, the resilience of the chip means that a measured quantity (typically 0.1-1 mg) of Wakefield^{TM} thermal compound may be used to mount the sample. Since the variation of the heat capacity of Wakefield grease with temperature is well-documented, the Wakefield contribution is simply subtracted at the end of the measurement.

PPMS calorimeters have three principal applications:

- High-temperature (20-350 K) measurements in large samples with a high signal-to-addenda ratio.
- Low-temperature (2-20 K) calibration of the absolute heat capacity values measured in a home-made microcalorimeter
- Ultra-low-temperature ($\leq$ 0.4 K) evolution of the specific heat in applied field $C(H)$

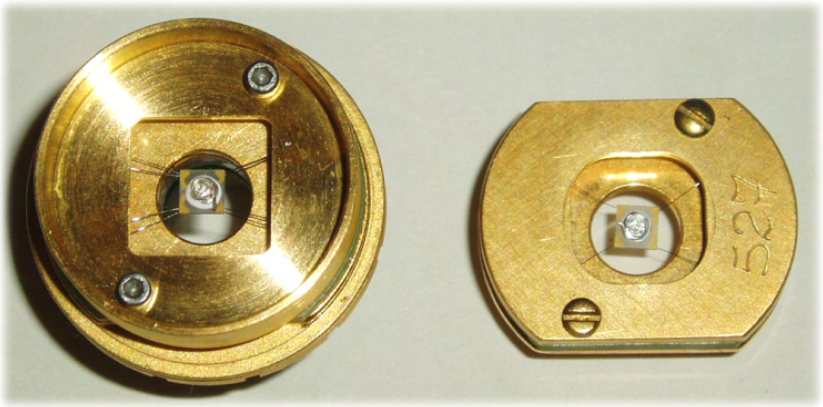

Figure 2.12: 8-wire (left) and 4-wire helium-3 (right) relaxation calorimeters for the PPMS. High purity silver wire samples for calibration are mounted on each chip with Wakefield^{TM} thermal compound.

Whilst refreshingly mechanically stable and robust compared with home-built 25 μm microcalorimeters, the PPMS calorimeters have their limitations. Since the chips incorporate a carbon film heater as well as a Cernox element, the addenda are relatively higher than for a microcalorimeter. At low temperatures in a magnetic field, the chip response is dominated by a bizarre magnetoresistive effect which requires very careful calibration with a silver reference sample for removal.

More seriously, the proprietary fitting algorithm tries to automatically account for any "τ_2 effect", which is essentially a secondary relaxation due to poor thermal coupling between sample and chip. This means that certain abrupt features in the specific heat - such as phase transitions - may be poorly fitted. In general, second-order transitions are reproduced acceptably, but first-order phase transitions are heavily broadened/smeared out due to their latent heat.

This fitting problem - in combination with the intrinsic lower resolution with the chip due to its increased thermal mass - explains why we are unable to see any evidence for the lambda anomaly characteristic of vortex melting and detailed in chapter 7. For these reasons, detailed studies of phase transitions should always be carried out using a microcalorimeter.

Chapter 3

Molybdenum Cluster Superconductors: a Brief Review

The superconducting world changed forever in 1971 when Roger Chevrel synthesised $M\mathrm{Mo_6S_8}$ - a new series of molybdenum cluster compounds - at the University of Rennes [8]. Superconductivity was discovered in several of these materials by Matthias in 1972 [80], with the highest T_c belonging to $\mathrm{PbMo_6S_8}$ at 13 K. Soon afterwards, not only did advances in sample preparation push the maximum T_c in $\mathrm{PbMo_6S_8}$ up to 15 K, the highest critical temperature for any ternary superconductor, but the upper critical field H_c2 was found to approach 60 T, an unprecedently large value and still the record-holder for non-cuprate superconductors [81, 82].

While the extensive range of commercial applications predicted for $\mathrm{PbMo_6S_8}$ and other high-field Chevrel-type compounds has so far failed to materialise (largely due to the advent of high-T_c cuprates coupled with sample preparation difficulties), the Rennes group has compensated for this by providing more gifts to the condensed-matter physics community. Using the $\mathrm{Mo_6}X_8$ cluster as a basic building block, Michel Potel and his coworkers developed a wide range of "cluster condensates", many of which exhibit superconductivity, anomalous metal-insulator transitions or sometimes both. Perhaps the most interesting group of these cluster-based materials is the quasi-1D $M_2\mathrm{Mo_6Se_6}$ family, composed of infinite-length $\mathrm{Mo_6Se_6}$ chains weakly coupled by M

ions. This group includes $Tl_2Mo_6Se_6$ and $In_2Mo_6Se_6$, which are the two most strongly one-dimensional superconductors currently known.

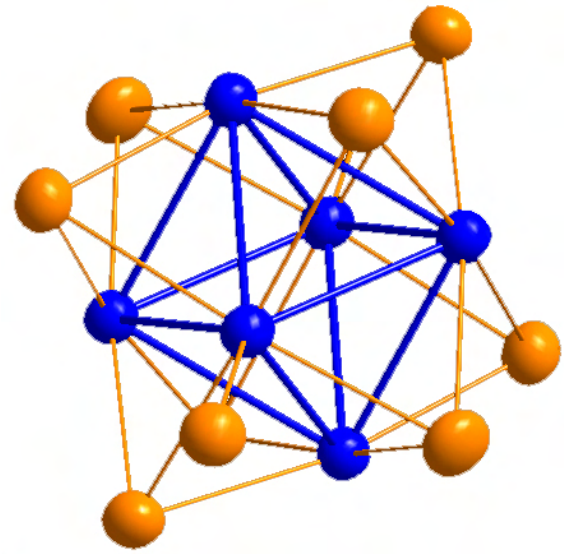

Figure 3.1: A single Mo_6X_8 cluster, the fundamental component of all molybdenum cluster compounds. A Mo_6 molybdenum octahedron (blue atoms) sits inside a X_8 chalcogen cube (yellow atoms).

By creating finite-length Mo_6X_8 stacks instead of infinite chains and coupling these with metallic ions, it is also possible to create compounds with an intermediate dimensionality. These materials offer the unique possibility to tune the effective dimensionality from quasi-1D to quasi-3D, simply by altering the stack height. This offers an unrivalled opportunity to control the evolution of low-dimensional effects in a crystal and observe their impact on its physical properties.

In this chapter we offer a brief review of the crystal structures and salient physical properties of the better-known molybdenum cluster-based materials, highlighting current gaps in our knowledge and key questions awaiting attention.

3.1 3D Chevrel Phase Materials $M\mathrm{Mo}_6X_8$

3.1.1 Crystal structure

Most Chevrel phases crystallise in a rhombohedral-hexagonal lattice with space group $R\bar{3}$. The crystal structure [83, 84] is shown in Fig. 3.2: essentially, Chevrel phases consist of Mo_6X_8 clusters, weakly coupled by metallic M atoms. All sides of the unit cell rhombohedron are equal in length and are inclined at a similar angle ($\sim$90°) to to each other; the structure may therefore be considered to be quasi-cubic. A Mo_6 octahedron sits inside a chalcogen X cube, which is in turn positioned within a lightly-deformed M cube.

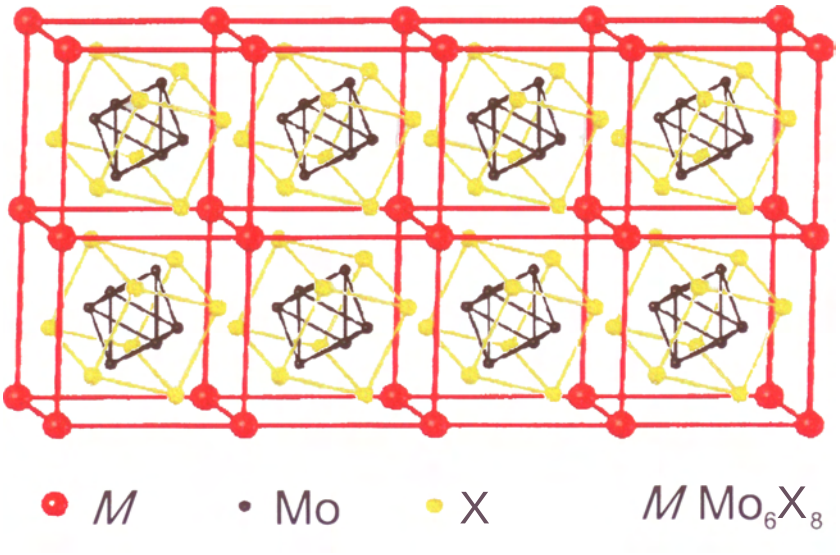

Figure 3.2: Generalised crystal structure for $M\mathrm{Mo}_6X_8$ stoichiometric Chevrel phase superconductors. M atoms are red, X (chalcogen) atoms yellow and Mo atoms black.

The faces of the X_8 cubes are rotated by 27° around the rhombohedral [111] axis. This increases the inter-cluster Mo-Mo separation to 3.10-3.60 Å, compared with a 2.65-2.80 Å intra-cluster distance. This results in the relatively weak cluster coupling: although the crystal structure may be quasi-three-dimensional, the electronic properties of Chevrel phases could almost be described as zero-dimensional, par-

tially explaining their very short superconducting coherence lengths.

3.1.2 Electronic structure

The Chevrel phase electronic band structure was originally calculated over 30 years ago [85, 86]. More recently, detailed full-potential linearized augmented plane wave (FLAPW) calculations have been carried out on a series of Chevrel phases by Gilles Santi in Geneva. The presence of two Mo d bands at the Fermi level has been confirmed for the majority of the compounds studied, although the binary compounds $\mathrm{Mo_6S_8}$ and $\mathrm{Mo_6Se_8}$ appear to have 3 bands at E_F and $\mathrm{LaMo_6Se_8}$ only has one. Diagrams of the calculated Fermi surfaces may be seen in Fig. 3.3: we only display Fermi surfaces for $\mathrm{PbMo_6S_8}$, $\mathrm{SnMo_6S_8}$ and $\mathrm{LaMo_6S_8}$ since these are the only compounds for which we present relevant data in chapters 6 and 8. The topology of these surfaces will be discussed in parallel with our experimental results. The relative contributions of the bands to the DoS at E_F are listed in Table 3.1, together with T_c and H_{c2} in each compound from the literature [33].

Table 3.1: Calculated relative contributions to the electronic density of states at the Fermi level in selected two-band Chevrel phase superconductors

	T_c	H_{c2}	Majority Band	Minority Band
$\mathrm{PbMo_6S_8}$	$\sim$ 14.5 K	55-60 T	63.0%	37.0%
$\mathrm{SnMo_6S_8}$	$\sim$ 13.5 K	35-40 T	60.8%	39.2%
$\mathrm{LaMo_6S_8}$	$\sim$ 6 K	$\sim$ 6T	93.6%	6.4%

3.1.3 Phonon densities of states

The phonon density of states (PDoS) in $\mathrm{PbMo_6S_8}$ and $\mathrm{SnMo_6S_8}$ was first evaluated by inelastic neutron scattering measurements in 1976 and confirmed by calculations in the same paper. It has been a source of occasional inspiration and frequent consternation to experimentalists ever since. Poppe *et al.* claimed to see traces of the phonon spectra in their planar tunnel junction experiments, thus suggesting that superconductivity may be conventionally mediated by the acoustic phonons associated with vibrations of the $\mathrm{Mo_6S_8}$ cluster [88]. Isotope effect measurements indicating conventional BCS-style behaviour in the binary $\mathrm{Mo_6Se_8}$ (T_c = 6.7 K) led to the unjustifiably hasty conclusion that the

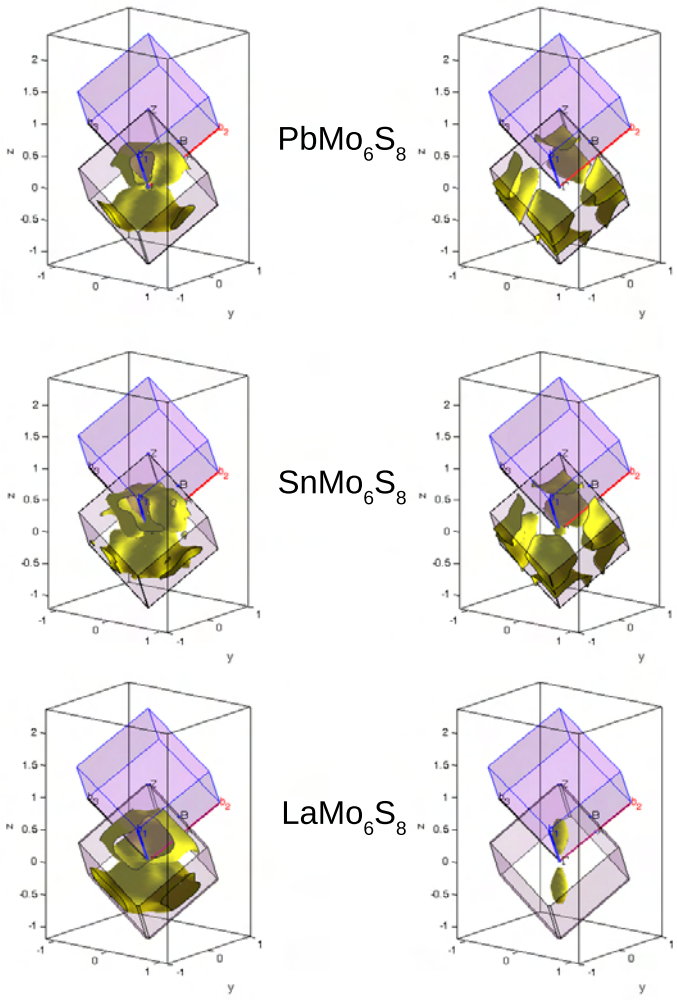

Figure 3.3: Calculated Fermi surfaces in $PbMo_6S_8$, $SnMo_6S_8$ and $LaMo_6S_8$. The majority contributor to the DoS at E_F is shown in the left column for each compound - see Table 3.1 for relative contributions. All Fermi surfaces are centred on the Γ point and displayed within the first Brillouin zone. Data courtesy of Gilles Santi.

Chevrel Phases were simple BCS superconductors, with the pairing in-

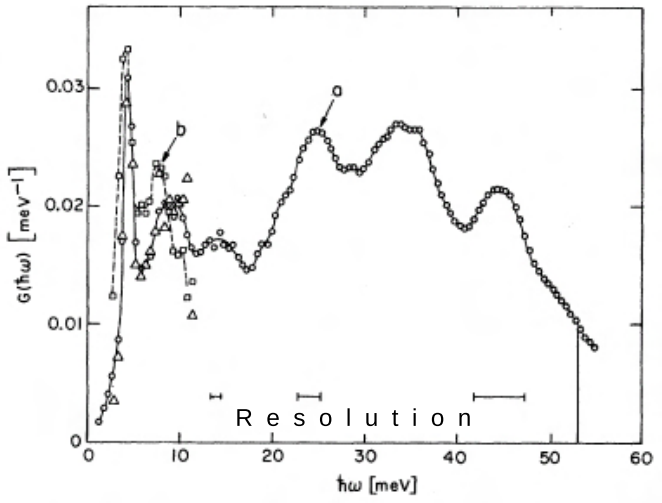

Figure 3.4: Phonon density of states from inelastic neutron scattering in $PbMo_6S_8$. The experimental resolution decreases at higher energy as indicated. The PDoS in $SnMo_6S_8$ is very similar. Data taken from ref. [87].

teraction mediated by a cluster phonon [38]. The low energy optical *M* phonon (located at around 4 meV in $PbMo_6S_8$) has been the major barrier to successful heat capacity measurements, since it is the dominant contribution to the specific heat below 10 K and cannot easily be modelled. Without this, the Chevrel Phases would probably have given up more of the secrets of their order parameter before now.

3.1.4 Previous tunnelling experiments

$PbMo_6S_8$ has previously been measured in an exchange-gas STM down to 2 K in Geneva [35] and the main conclusions of this work can be found in Fig. 3.5. The experimental spectrum clearly cannot be fitted using an isotropic BCS s-wave model; although the d-wave model does not give a perfect fit either, it is much more capable of reproducing the spectral gradient within the gap. This implies that quasiparticle states exist within the superconducting gap, an observation which is in qualitative agreement with a previous planar junction tunnelling experiment [88].

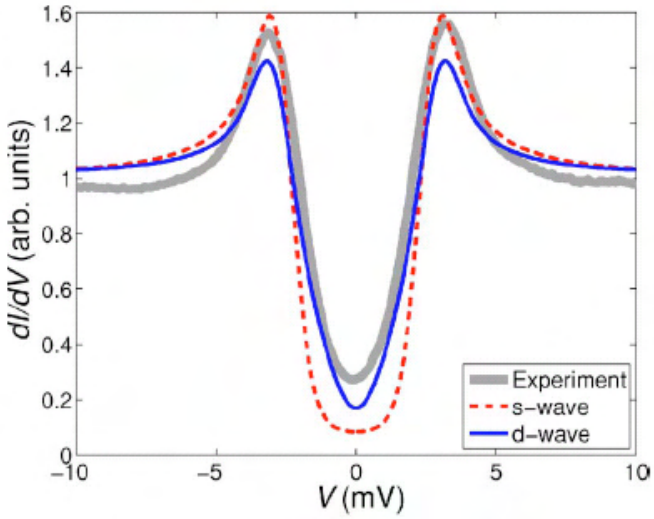

Figure 3.5: Normalised zero-field STM spectrum in $PbMo_6S_8$ at 2 K, together with isotropic s-wave and d-wave fits. Data from ref. [35].

The gap function in the Chevrel Phases is therefore expected to be unconventional. However, still more unusual was the observation of a depression in the LDoS within the vortex cores of $PbMo_6S_8$. This behaviour is reminiscent of the high-T_c cuprates and further encouraged a d-wave symmetry interpretation. The vortices also appeared to be oval in shape, indicating an anisotropic coherence length, although it remained unclear whether this was intrinsic or a lattice thermal drift effect. These early tunnelling experiments raised as many questions than they answered, highlighting the need to continue STM studies on both $PbMo_6S_8$ and $SnMo_6S_8$ at sub-Kelvin temperatures.

3.2 Intermediate Dimensionality Cluster Composites

Compounds formed from "cluster chain fragments" are an intriguing subset to the molybdenum cluster family. Essentially, Mo_6S_8 units are stacked together linearly to form short cylinders, which are weakly coupled by metallic ions in a similar fashion to the Chevrel Phases. One of the most interesting groups of compounds in this family is the

$Rb_{2n}(Mo_9S_{11})(Mo_{6n}S_{6n+2})$ series, where n = 1-4. Examples of the crystal structures and basic transport properties may be found in ref. [89]. It seems possible to tune the dimensionality from weakly 3D towards the quasi-1D limit by increasing n, which is a fascinating chemical alternative to mechanical dimensional modification by pressure or strain.

A single paper detailing transport and magnetic measurements in $Cs_2Mo_{12}Se_{14}$ and $Rb_4Mo_{18}Se_{20}$ has also been published [90]. This claims extremely short coherence lengths and $H_{c2} \sim 40$ T in $Rb_4Mo_{18}Se_{20}$. Given that the authors previously claimed $H_{c2} \sim 50$ T in $Tl_2Mo_6Se_6$ in contrast with other works indicating a value of around 10 T [91, 37], this estimate may perhaps be rather optimistic. However, the two compounds studied definitely merit further attention.

Many more of these intermediate compounds exist, all with rich physical promise. Although encouraging preliminary thermodynamic and magnetic measurements have been carried out in C and B, we will not discuss these further in this work. As one might expect, their physical properties appear to lie between those of the Chevrel Phases and $M_2Mo_6Se_6$, but significantly more data will be required before making any firm conclusions.

3.3 Quasi-1D Condensates $M_2Mo_6Se_6$

A logical progression from stacking together small numbers of Mo_6X_8 clusters is to attempt to create an infinite-length chain or "condensate". This was first achieved by Michel Potel in 1980 [32, 92], who synthesised $M_2Mo_6Se_6$ (M = Na, In, K, Tl), $M_2Mo_6S_6$ (M = K, Rb, Cs) and $M_2Mo_6Te_6$ (M = In, Tl). Shortly afterwards, superconductivity was discovered in $Tl_2Mo_6Se_6$ [91], leading to a small flurry of research which was only curtailed by the advent of high-T_c cuprates in 1987. Difficulties in synthesising the sulphides together with a lack of superconductivity in the telluride branch of the family [93] meant that efforts were concentrated on the selenides, whose numbers were soon increased to include $Rb_2Mo_6Se_6$ and $Cs_2Mo_6Se_6$. The bare uncoupled chain compound Mo_6Se_6 also exists, as does $Li_2Mo_6Se_6$, although the latter is unstable and dissolves in any polar organic solvent [94].

3.3.1 Crystal structure

Research in $M_2Mo_6Se_6$ has always focussed on the low dimensionality of these materials, which is immediately obvious when looking at the

crystal structure (Fig. 3.6). $M_2Mo_6Se_6$ crystallises in a hexagonal unit cell (space group $P6_3/m$) containing a single formula unit. $(Mo_6Se_6)_\infty$ chains run parallel to the c axis, weakly coupled by M "guest" ions. It is easiest to imagine the chains as an offset stack of Mo_3Se_3 triangles, pointing in alternate directions. Intra-chain Mo-Mo bonds are very close to the intra-cluster bonds observed in Chevrel-type compounds and the Mo-Mo separations are consequently also similar.

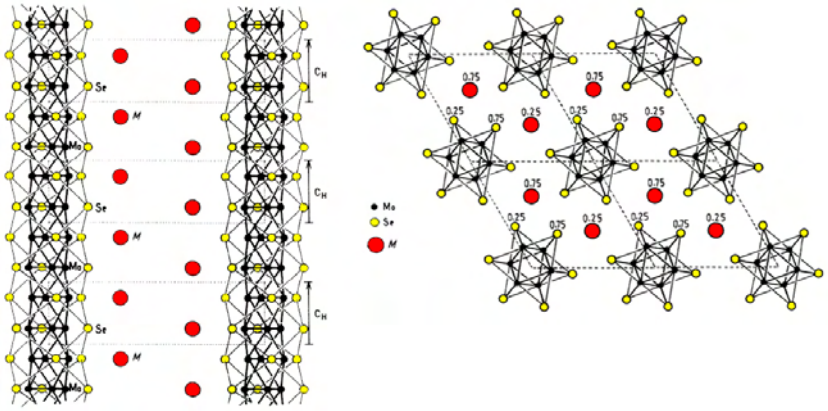

Figure 3.6: Generalised crystal structure for $M_2Mo_6Se_6$ quasi-1D cluster condensates. M atoms are red, Se atoms yellow and Mo atoms black.

The critical difference between $M_2Mo_6Se_6$ and all other molybdenum chalcogenides is that there is no Se atom on the c (ternary) axis. In other chalcogenides, three square chalcogen faces are created on each side of a cluster, thus facilitating a bond to the neighbouring cluster. These transverse bonds are totally absent in $M_2Mo_6Se_6$. Furthermore the minimum Mo-Mo interchain distance is greater than 6Å, virtually eliminating any direct interchain Mo $4d$-$4d$ overlap. This means that all electronic interchain coupling is mediated by two Se atoms per cluster. In a further contrast with the Chevrel Phases, the M ion is always monovalent in $M_2Mo_6Se_6$. Originally it was thought that all quasi-1D cluster condensates were stoichiometric [95, 96], but following an extensive powder diffraction study in Rennes it was concluded that a slight M ion deficiency is intrinsic to these materials. For $Tl_2Mo_6Se_6$, the Tl occupancy ranges from 1.88 to 1.96, with the highest T_c occurring at 1.94.

The lack of stoichiometry has been a major barrier towards interpreting the physical properties of $M_2Mo_6Se_6$, for the simple reason that in transport measurements, two samples of the same compound rarely behave in an identical fashion. While one might imagine that the average stoichiometry of two crystals from the same growth batch should be the same, the extremely weak coupling between the Mo_6Se_6 chains implies that current flow within a sample does not penetrate the bulk and may follow a complex path subject to local defects and stoichiometric variations. Bulk or thermodynamic measurements are therefore expected to provide more reproducible and statistically valid results.

3.3.2 Electronic band structure

Kelly and Andersen performed the first band-structure calculations on $Tl_2Mo_6Se_6$ in the early 1980s [95, 96] and for the next 20 years their results dominated all attempts to interpret the behavioural trends seen in $M_2Mo_6Se_6$. However, we do not wish to dwell on this data since more recent calculations have shown it to be incorrect [97, 98]. Instead of the original 3-band scenario, only a single Mo helix d band crosses the Fermi level, yielding an extremely one-dimensional Fermi surface consisting of two warped planes. The calculated bandstructures around E_F can be seen for all six compounds in Fig. 3.7.

The Mo d band at E_F is very broad, extending down to ~ 1 eV below E_F. This explains why $M_2Mo_6Se_6$ do not universally undergo a $2k_F$ charge density wave (CDW) transition at high temperature (where k_F is the Fermi wavevector), as would be expected for such a highly one-dimensional Fermi surface. Due to its large width, the Mo d band has a very low density of states. It would therefore cost more energy to create a lattice modulation than could be recuperated from the associated electronic reconstruction; hence the stability of $M_2Mo_6Se_6$ against the Peierls transition.

We may obtain a quantitative measure of the Fermi surface warping (and hence the electronic anisotropy) by considering the "linewidth" ΔE at E_F in Fig. 3.7. This is equal to the separation of the highest and lowest state energies in the d band when moving from reciprocal lattice point A $\rightarrow$ L $\rightarrow$ H $\rightarrow$ A (cutting the Fermi surface). Figure 3.8 shows the variation of ΔE across $M_2Mo_6Se_6$.

Group IA compounds are significantly more anisotropic than Group III, with the anisotropy increasing further as we move down Group IA. The implications of this trend on the physical properties of $M_2Mo_6Se_6$ will be discussed in detail in chapter 5.

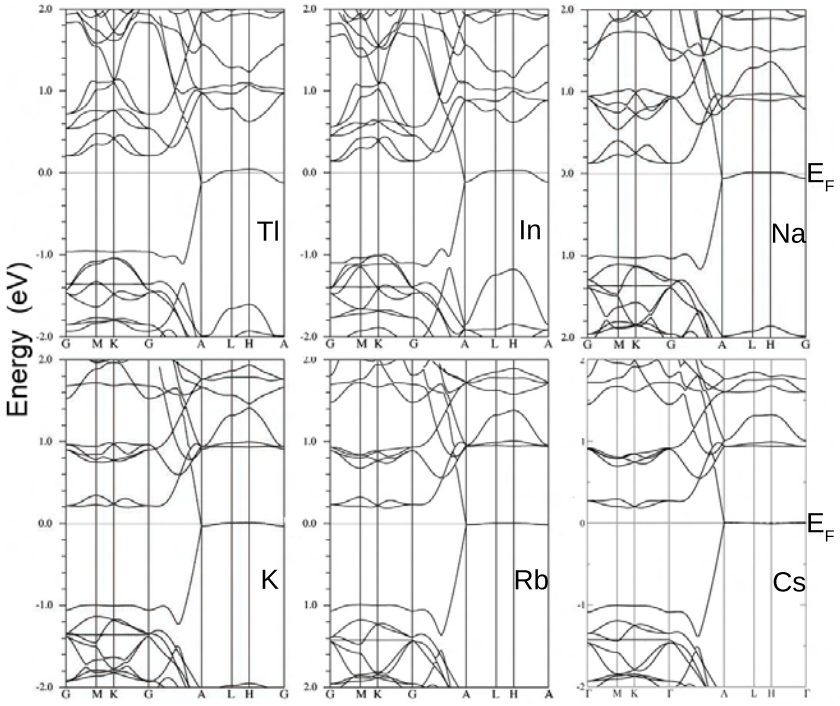

Figure 3.7: Calculated electronic bandstructures close to E_F in $M_2Mo_6Se_6$ for different M guest ions [97, 98].

3.3.3 Superconductivity in $M_2Mo_6Se_6$

Superconductivity was first detected in $Tl_2Mo_6Se_6$ by Armici *et al.* in 1980 by means of resistivity measurements [91]. Two distinct sample behaviours were observed: "A"-type samples maintain metallic resistivity down to a T_c of $\sim$ 2-3 K, whereas "B"-type samples displayed a minimum in resistivity at around 20 K followed by a superconducting transition at T_c = 6K. Early attempts at growing $In_2Mo_6Se_6$ crystals failed to produce superconducting samples [99, 100]. However, later measurements in Rennes indicated that this too was superconducting with a T_c of $\sim$ 2-3 K, although these results were never published [101].

Very little is known about the superconducting ground state in these materials. An attempt to measure the low-temperature specific heat in $Tl_2Mo_6Se_6$ failed due to a lack of sensitivity [102]. Brusetti *et al.* in-

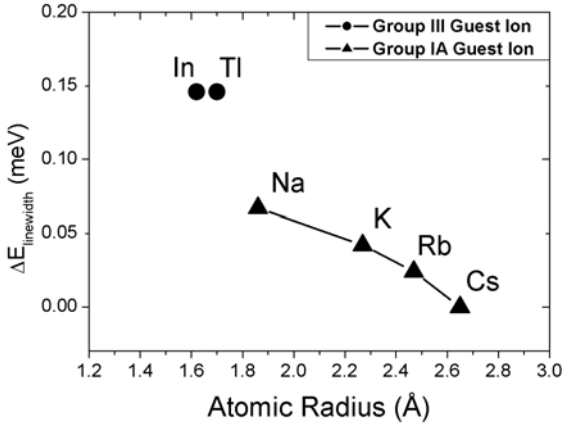

Figure 3.8: Calculated electronic linewidths in $M_2Mo_6Se_6$ for different M guest ions. The linewidth indicates the degree of warping of the Fermi surface and hence the electronic anisotropy.

vestigated the magnetisation and discovered that the lower critical field H_{c1} does not saturate down to low temperature, thus suggesting unconventional behaviour [103]. More recently, transport measurements in $Tl_2Mo_6Se_6$ down to 350 mK display a substantial broadening of the superconducting transition in an applied magnetic field [37]. Such a broadening is generally indicative of strong fluctuations and a departure from mean-field (i.e. BCS) behaviour, thus constituting additional evidence for unconventional physics.

3.3.4 Phonon densities of states

A comprehensive study of the PDoS by inelastic neutron scattering in $Tl_2Mo_6Se_6$, $In_2Mo_6Se_6$ and $Rb_2Mo_6Se_6$ has been carried out by Brusetti and co-workers [105, 104]. The results are slightly reminiscent of those obtained by Bader *et al.* in the Chevrel phases, with the low-energy PDoS dominated by an Einstein-type mode from the M ion vibrating between the chains, followed by a set of acoustic modes in the 12-20 meV range arising from the Mo_6Se_6 chains. Calculations have shown that the most important of these is the so-called "breathing mode" in which the Mo and Se atoms at each end of a unit cell vibrate by stretching and relaxing the cell parallel to the c-axis (chain direction) [97, 106] In principle, this mode is capable of driving a Peierls transition by producing

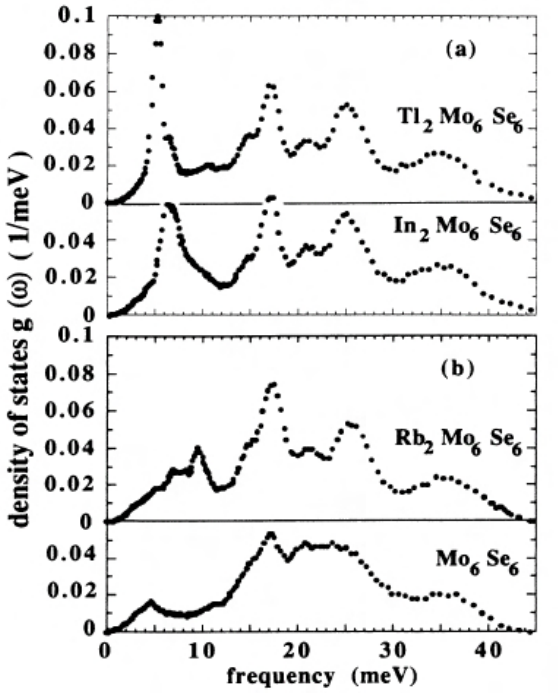

Figure 3.9: Phonon densities of states for (a) $Tl_2Mo_6Se_6$, $In_2Mo_6Se_6$ and (b) $Rb_2Mo_6Se_6$, Mo_6Se_6, from ref. [104]. The low-energy mode characteristic of *M* ion vibration is absent in Mo_6Se_6, as expected, but the intra-chain modes above 12 meV remain similar.

a $2k_F$ structural modulation along this axis.

The observation that the *M* ion mode loses intensity and moves to increasing energy upon travelling down Group IA led to the suggestion that this phonon could be responsible for superconductivity (since $Rb_2Mo_6Se_6$ exhibits insulating behaviour under ambient pressure [93]). As we will see in chapter 4, this assertion is not entirely true.

3.3.5 Metal-insulator transitions

Very little experimental data has been published for the *M* = Group IA compounds. Early resistivity measurements in $Rb_2Mo_6Se_6$ indicated a broad minimum followed by an upturn with decreasing tem-

perature and AC susceptibility data from the same authors confirmed the constant weak diamagnetic susceptibility from 5-300 K seen in all $M_2Mo_6Se_6$ [93]. Two papers from Hor *et al.* revealed a drop in the resistivity $\rho(T)$ for M = Na, K and Rb under hydrostatic pressure, even claiming a sudden drop in $\rho(T)$ at low temperature as evidence for induced superconductivity in these compounds [107, 108]. Since 1985 there has been no new data for M = Group IA except for the PDoS measurement in $Rb_2Mo_6Se_6$.

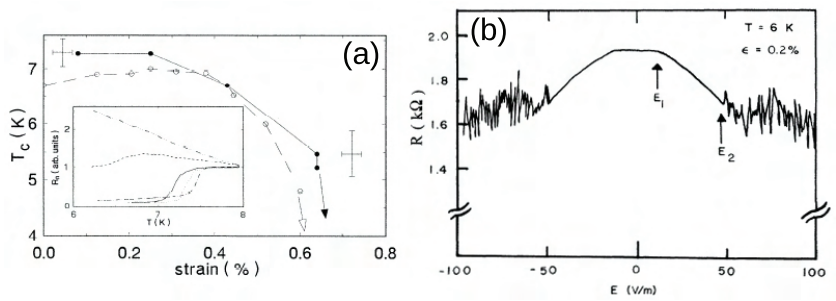

Figure 3.10: (a) Variation in the T_c for A (open circles) and B-type (closed circles) $Tl_2Mo_6Se_6$ single crystals as a function of applied strain. The inset shows the low-temperature $\rho(T)$ variation for an A-type sample at several different strains, confirming the suppression of superconductivity and development of an upturn in the resistivity. (b) Broadband noise in the differential resistance of a strained $Tl_2Mo_6Se_6$ sample. All data taken from ref. [109].

However, two more recent papers on superconducting $Tl_2Mo_6Se_6$ may offer valuable clues as to the nature of the groundstate in the insulating members of the family. Firstly, Tessema *et al.* applied uniaxial strain to single crystals along the c-axis using a piezoelectric pulling device [109]. Measuring both A and B-type samples, they discovered that they could suppress superconductivity with relatively low strain values (see Fig. 3.10(a)). Intuitively, stretching a quasi-1D metal along its chain axis should make it even more one-dimensional, thus linking the insulating phase to the low-dimensional crystal structure. Perhaps even more revealing was their observation of broadband noise in the differential resistance of $Tl_2Mo_6Se_6$ above a threshold voltage. Such a noise spectrum is generally taken as evidence for sliding density-wave motion [110].

In 1994 Brusetti *et al.* published their most detailed (and final)

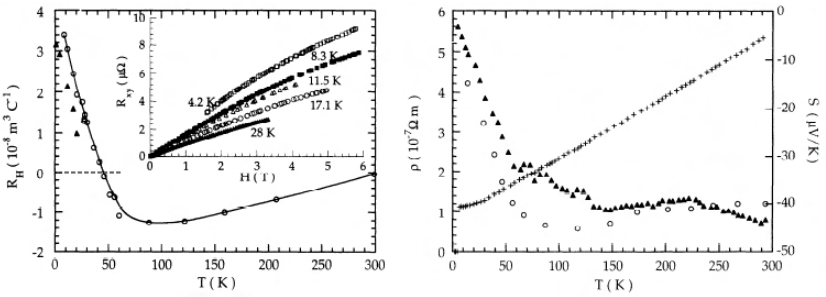

Figure 3.11: Left: Hall co-efficient in $Tl_2Mo_6Se_6$, with the inset displaying the magnetic field-dependence of the Hall voltage. Right: thermal conductivity from two independent measurements and resistivity in $Tl_2Mo_6Se_6$. Both Hall effect and thermal conductivity display a distinct crossover in their behaviour at around 80 K, despite no trace of this being visible in the resistivity. Data taken from ref. [111].

analysis of the transport properties of $Tl_2Mo_6Se_6$, including Hall effect measurements which are no mean feat given the small sample dimensions [111]. Although ultimately inconclusive, this work produced evidence for the onset of a hidden density wave at around 80 K: a minimum in the Hall voltage and a crossover in the thermal conductivity are both located at this point. The extremely low density of states at the Fermi level evaluated in ref. [103] also added weight to the argument that superconducting and density-wave groundstates might coexist at low temperature, as suggested by the strain data.

Perhaps the greatest failing in all previous work on $M_2Mo_6Se_6$ was the authors' concentration on individual compounds, rather than collectively considering the entire family. In chapter 5, we seek to redress this balance by assembling a universal $M_2Mo_6Se_6$ phase diagram and considering the trends across it. The data and conclusions from the experiments detailed above will prove invaluable to our interpretation and proposal of a model for the underlying physics in $M_2Mo_6Se_6$.

Chapter 4

Low-dimensional Fluctuations and Phonon Mode Spectroscopy in $M_2Mo_6Se_6$

During the construction period of the new helium-3 STM, an extensive characterisation of the little-known quasi-1D $M_2Mo_6Se_6$ compounds took place. Initially focussing on unusual behaviour in the superconducting state, we later diversified to a full analysis of both the normal-state and superconducting properties using AC susceptibility, electrical transport and specific heat measurements. In this chapter we will concentrate on superconducting $Tl_2Mo_6Se_6$ and $In_2Mo_6Se_6$, using data from $Rb_2Mo_6Se_6$ for comparative purposes. The reason $Rb_2Mo_6Se_6$ was chosen from the other Group IA metal compounds was simply that up until now, it has been the most widely studied of all the insulating $M_2Mo_6Se_6$ compounds, most importantly having already been the subject of an inelastic neutron scattering experiment. [104]

4.1 Crystal Growth and Experimental Procedure

All crystal growth was carried by Michel Potel, Diala Salloum and colleagues at the University of Rennes. Needle-like crystals of dimensions approximately 1-3.5 mm $\times$ 300 μm $\times$ 100 μm and mass $\approx$ 800 μg were synthesised by different methods depending on the thermal stability of the compounds: $Tl_2Mo_6Se_6$ and $Rb_2Mo_6Se_6$ were prepared in sealed molybdenum crucibles at 1700 °C and 1500 °C respectively, whereas $In_2Mo_6Se_6$ was prepared in an evacuated sealed silica tube at 1100 °C. Their crystalline structures were verified by a mono-crystal diffraction method using a KAPPA CCD NONIUS: the compounds exhibit a slight cation deficiency with occupancy factors 0.95, 0.94 and 0.93 for In, Tl and Rb based compounds respectively. Larger polycrystalline samples of $Tl_2Mo_6Se_6$ and $In_2Mo_6Se_6$ of mass 10-75 mg were also produced by the same methods. A photograph of a typical crystal - in this case $In_2Mo_6Se_6$ - is shown in Fig. 4.1.

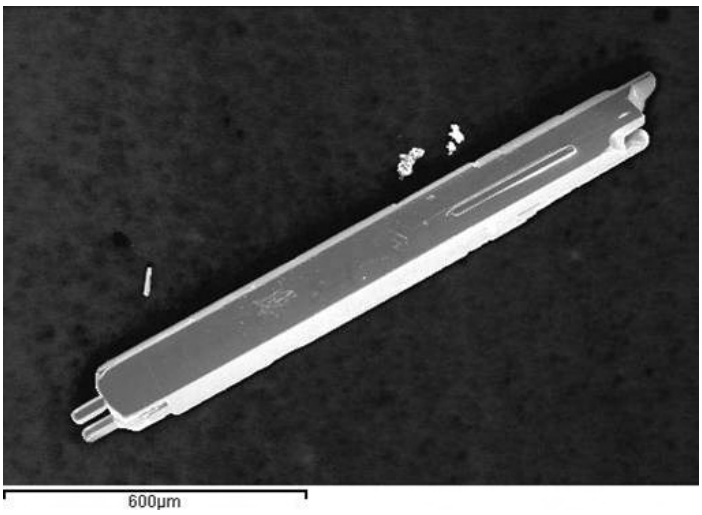

Figure 4.1: $In_2Mo_6Se_6$ single crystal exhibiting excellent as-grown surfaces.

The samples were initially characterized by AC susceptibility, measured using the PPMS with a 0.1 Oe excitation at 470 Hz. As shown in Fig. 4.2, $Tl_2Mo_6Se_6$ and $In_2Mo_6Se_6$ both exhibit superconducting tran-

sitions at T_c=4.2 K and 2.85 K, with ΔT_c=0.7 K and 0.5 K respectively. $Rb_2Mo_6Se_6$ displays a constant weak diamagnetic signal down to the lowest temperature measured (1.7K) with no sign of superconductivity being observed. No significant increase in transition width was observed for the polycrystals compared to the single crystals, indicating a high sample quality. We stress that all members of the $M_2Mo_6Se_6$ family remain stable under atmospheric conditions and none of our samples has exhibited any ageing effects.

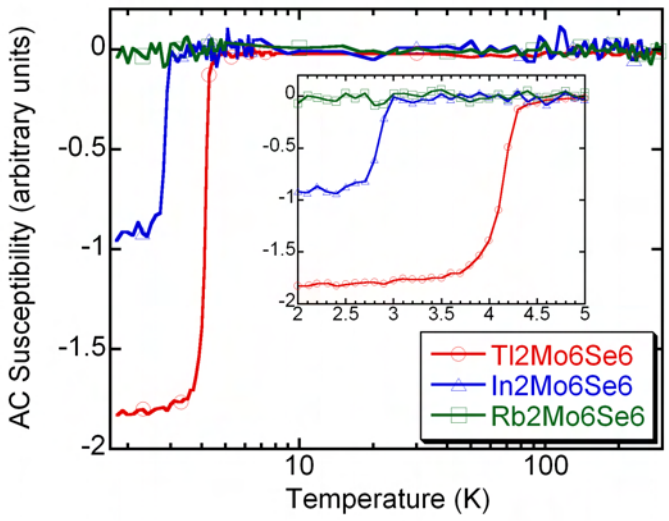

Figure 4.2: AC susceptibility of $Tl_2Mo_6Se_6$, $In_2Mo_6Se_6$ and $Rb_2Mo_6Se_6$ from 1.8-300 K. Inset: zoom onto superconducting transitions, with T_c=4.2 K and 2.85 K in $Tl_2Mo_6Se_6$ and $In_2Mo_6Se_6$ respectively. As is the case for all graphs in this work, only a small fraction (typically 10-20 %) of the data-points measured are explicitly marked for clarity.

4.1.1 Electrical transport measurements

AC Resistivity was measured using the same QD PPMS with a helium-3 insert from 0.35-300 K. Four gold contacts of thickness ~5 nm were sputtered onto single crystals of each compound and 50 μm gold wires attached using silver epoxy glue. This method yielded contact resistances ~1 Ω. Short (1 s) pulses of a small AC current (0.02 mA, 470 Hz)

were used to minimise any heating effects in the sample at low temperature.

4.1.2 Heat capacity data

Specific heat was initially also measured in the QD PPMS using a standard relaxation technique from 0.35-300 K. The largest homogeneous polycrystalline samples available for each compound were mounted using a measured quantity of Wakefield^{TM} grease (whose contribution to the heat capacity was later subtracted). However, due to the extremely small density of states at the Fermi level the QD PPMS was unable to detect the superconducting transition in $Tl_2Mo_6Se_6$ and $In_2Mo_6Se_6$. High-sensitivity relaxations from 1.3-10 K were therefore carried out on single crystals in our dedicated specific heat laboratory, enabling us to study the superconducting transition with a magnetic field both perpendicular and parallel to the z axis.

4.2 Characteristics of Superconductivity

As previously reported [37], resistive transitions into the superconducting state of $Tl_2Mo_6Se_6$ exhibit an anomalous broadening under an applied magnetic field H, similar to that seen in the HTS. We have performed similar measurements on $In_2Mo_6Se_6$ and show these in Fig. 4.3, together with the results in $Tl_2Mo_6Se_6$ for comparison. It can immediately be seen that $In_2Mo_6Se_6$ also displays a broadening of the transition with increasing field, although the effect is less spectacular than in $Tl_2Mo_6Se_6$. This is highlighted in Fig. 4.3(f), where we have plotted the normalised transition width $\Delta T_c(H)/\Delta T_c(0)$ as a function of normalised perpendicular magnetic field H/H_{c2} for both $Tl_2Mo_6Se_6$ and $In_2Mo_6Se_6$. Both materials display a linear behaviour in $\Delta T_c(H)/\Delta T_c(0)$ as the field increases, with the gradient for $Tl_2Mo_6Se_6$ $\sim$ 30% larger than that of $In_2Mo_6Se_6$.

The width of a superconducting transition is governed by two parameters: the intrinsic homogeneity of the superconductor and the narrow thermal fluctuation-dominated critical region which surrounds any phase transition. In the case of inhomogeneity contributions, the width is field-independent. For 3D fluctuations the width of the critical region is given by the Ginzburg parameter

$$G_{3D} = (k_b T_c/\sqrt{2}\xi_\perp^2 \xi_\parallel H_c(0)^2)^2 \tag{4.1}$$

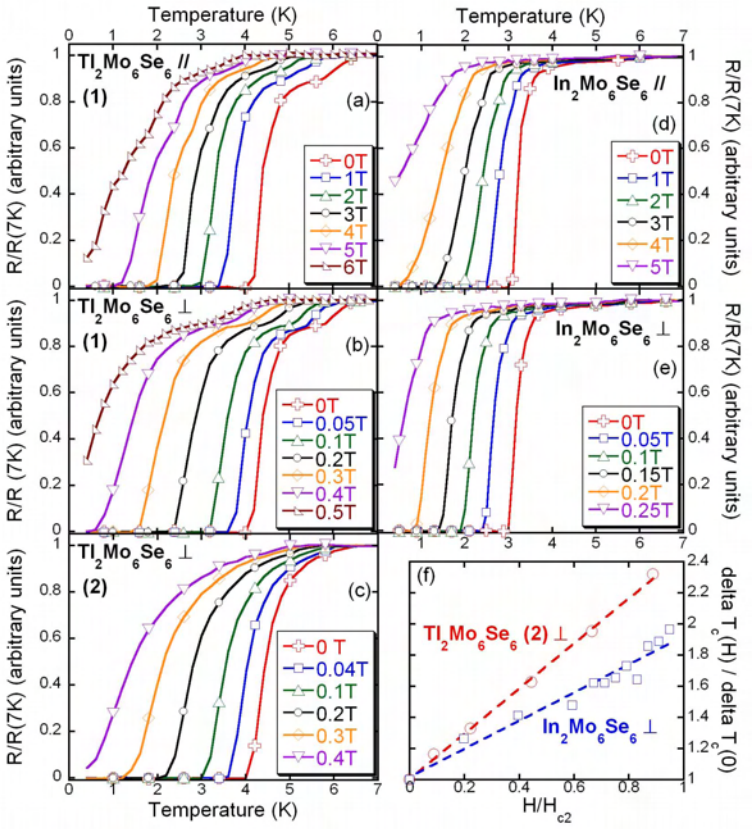

Figure 4.3: (a)-(e): Resistive transitions in $Tl_2Mo_6Se_6$ and $In_2Mo_6Se_6$ with field both parallel and perpendicular to the z axis. Two samples of $Tl_2Mo_6Se_6$ are shown: Sample (1) displaying a double transition indicating an inhomogeneous Tl content and Sample (2) with a single broad transition. (f): Normalised transition widths $\Delta T_c(H)/\Delta T_c(0)$ as a function of normalised magnetic field H/H_{c2}. For a transition in magnetic field H, ΔT_c is defined as the temperature difference between resistivities of 5% and 95% of the saturated normal-state value at 7 K.

multiplied by T_c. This is weakly field-dependent, since

$$G_{3D}(H) \approx G_{3D}^{1/3}(H/H_{c2})^{2/3} \tag{4.2}$$

This clearly cannot explain our data, since we observe ΔT_c to increase

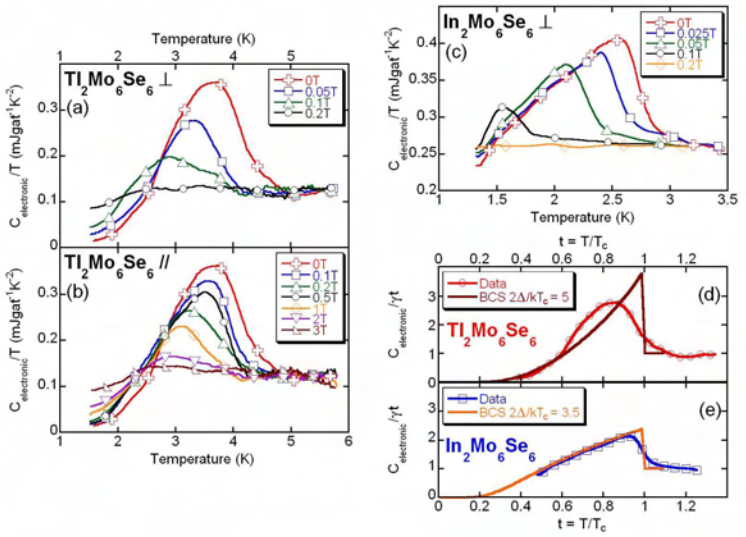

Figure 4.4: (a)-(c): Superconducting transitions in $Tl_2Mo_6Se_6$ and $In_2Mo_6Se_6$ seen by specific heat with field both parallel and perpendicular to the z axis. (d),(e): BCS fits of the zero-field transition in $Tl_2Mo_6Se_6$ and $In_2Mo_6Se_6$.

linearly as H increases. However, Mishonov *et al.* [112] derived a quasi-1D Ginzburg parameter for a superconducting nanowire:

$$G_{1D} = \frac{k_B}{8\sqrt{\pi}\Delta C \xi(0) S} \tag{4.3}$$

where ΔC is the specific heat jump at T_c, S is the cross-sectional area of the nanowire and we only consider longitudinal fluctuations so $\xi(0) \equiv \xi_{\parallel}(0)$. Modelling $M_2Mo_6Se_6$ as a weakly-coupled assembly of superconducting filaments, each with the radius of a single Mo_6Se_6 chain, we calculate critical region widths $G_{1D}T_c$ = 1.5 K and 2.0 K for $Tl_2Mo_6Se_6$ and $In_2Mo_6Se_6$ respectively.

Similar trends are also seen in the electronic contribution to the heat capacity (Fig. 4.4), with $Tl_2Mo_6Se_6$ and $In_2Mo_6Se_6$ behaving very differently in a magnetic field. The onset temperature T_{ons} of the specific heat jump in $In_2Mo_6Se_6$ is rapidly and uniformly displaced to lower temperature with increasing H, whereas regardless of the applied field strength or orientation, T_{ons} does not drop below $\sim$ 4K in $Tl_2Mo_6Se_6$. It should

be noted that $In_2Mo_6Se_6$ shows an abnormally large electronic contribution to the specific heat γ in proportion to its specific heat jump, suggesting that only around 50% of the electrons at the Fermi level become superconducting. This scenario could be explained by a slight variation in the sample stoichiometry leading to a CDW coexistent with superconducting regions in the same crystal, hence also supporting our observation that $In_2Mo_6Se_6$ is more anisotropic than $Tl_2Mo_6Se_6$. Correcting for this anomaly in $In_2Mo_6Se_6$, we estimate a Sommerfeld constant $\gamma \approx 0.13$ mJgat^{-1}K^{-2} for both $Tl_2Mo_6Se_6$ and $In_2Mo_6Se_6$, corresponding to a dressed density of states at the Fermi level D_{E_F} = 0.055 states eV^{-1} atom^{-1}.

We have attempted to fit the low-temperature electronic specific heat in $Tl_2Mo_6Se_6$ and $In_2Mo_6Se_6$ using a standard BCS s-wave single-band α-model, as shown in Fig. 4.4 (d) and (e). Our band structure calculations indicate that only a single band (the 1D Mo d helix) crosses the Fermi level, thus eliminating any possibility of multi-band superconductivity in $M_2Mo_6Se_6$. Although the jump we measure at T_c is thermally broadened in each case, this yields an excellent fit for $In_2Mo_6Se_6$ with a gap value of 0.4 meV corresponding to $2\Delta_0/k_BT_c$ = 3.5, just below the standard weak-coupling BCS value 3.52. An unusual hump on the back of the peak in $Tl_2Mo_6Se_6$ renders the fit more difficult in this compound, but by using entropy conservation it is still possible to estimate a gap $\Delta_0 \geq 1.1$ meV and $2\Delta_0/k_BT_c \geq 5$, placing it in the extreme strong-coupling regime. Although the quality of our fit in $In_2Mo_6Se_6$ does not appear to favour the presence of low-lying excitations, we were not able to accurately measure to sufficiently low temperatures in $Tl_2Mo_6Se_6$ to conclusively rule out the existence of d-wave superconductivity in this material. However, it is clear that $Tl_2Mo_6Se_6$ has a significantly less conventional superconducting ground state than $In_2Mo_6Se_6$, an astonishing difference considering the close similarity between the compounds.

Completing the analysis of our data using anisotropic Ginzburg-Landau theory [51], we summarise the superconducting parameters of both $Tl_2Mo_6Se_6$ and $In_2Mo_6Se_6$ in Table 4.1. The large calculated values for κ highlight both the extreme type II nature of these superconductors and their enormous anisotropy. $H_{c2}^{\parallel}$ and $\xi^{\parallel}$ should be regarded as minima, due to the high sensitivity of these materials to the field orientation [91]. We estimate a sample alignment better than $\pm$ 2 $^\circ$ with the field; however non-parallel crystalline intergrowths may exist within a single needle-like sample which would reduce our measured $H_{c2}^{\parallel}$. The measured $H_{c2}^{\parallel}$ = 4.35 T in $In_2Mo_6Se_6$ approaches the Clogston

Table 4.1: Measured and derived anisotropic superconducting parameters in $Tl_2Mo_6Se_6$ and $In_2Mo_6Se_6$

	$Tl_2Mo_6Se_6$		$In_2Mo_6Se_6$	
	$\parallel$	$\perp$	$\parallel$	$\perp$
	Measured			
T_c	4.2 K		2.85 K	
$H_{c2}(0)$	5.9 T	0.47 T	4.35 T	0.25 T
$H_c(0)$	0.0207 T		0.0119 T	
	Derived			
ϵ	12.6		17.2	
$\xi(0)$	940 Å	75 Å	1500 Å	87 Å
$\lambda(0)$	0.12 μm	1.5 μm	0.13 μm	2.2 μm
κ	202	1.3	260	0.87
G_{3D}	3.3 10^{-6}		3.0 10^{-6}	
G_{1D}	0.36		0.69	
γ_n	0.13 mJ K^{-2} gat^{-1}		0.13 mJ K^{-2} gat^{-1}	
BCS gap Δ_0	$\geq$ 0.9 meV		0.4 meV	
$2\Delta_0/k_BT_c$	$\geq$ 5		3.5	
$H_P = \Delta_0/\sqrt{2}\mu_B$	11 T		4.9T	

limit H_P = 4.9 T and it would be instructive to re-measure the resistivity of a small single crystal in a high-accuracy goniometer in order to verify the possibility of Pauli-limited superconductivity occurring in this compound.

4.3 Normal-State Properties

4.3.1 Specific heat and phonon density of states

Two features are immediately apparent in a plot of C_{tot}/T vs. T: a strong peak at $T\sim$ 80 K and a shoulder at $T\sim$ 20 K, indicating two dominant phonon energies.

The high-temperature specific heat data measured on larger polycrystalline samples are sufficiently noise-free to permit an inversion of the phononic contribution $C_{ph}(T)$ to the total heat capacity, hence obtaining the PDoS $F(\omega)$. We stress that this method does not provide a detailed PDoS $\omega(q)$ map of the type revealed by neutron scattering, but rather produces a smoothed phonon distribution function $\widetilde{F}(\omega)$. The specific heat and low-temperature features of the PDoS are accurately

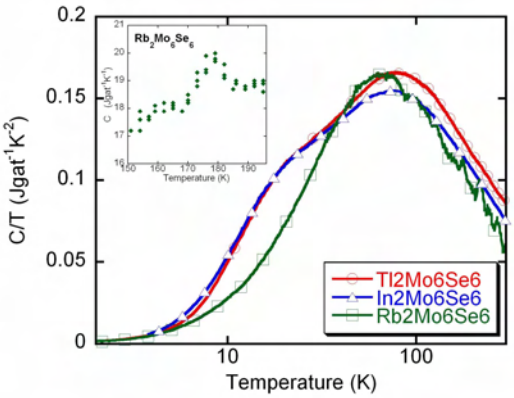

Figure 4.5: Total specific heat divided by temperature C/T for $Tl_2Mo_6Se_6$ (circles), $In_2Mo_6Se_6$ (squares) and $Rb_2Mo_6Se_6$ (diamonds). Inset: zoom on $Rb_2Mo_6Se_6$ showing a small blurred anomaly at 175 K

reproduced by $\widetilde{F}(\omega)$, but it does not give a high-precision representation of the PDoS at high temperature. We model $F(\omega)$ as a series of logarithmically-spaced Einstein modes with fixed energies and adjustable weights:

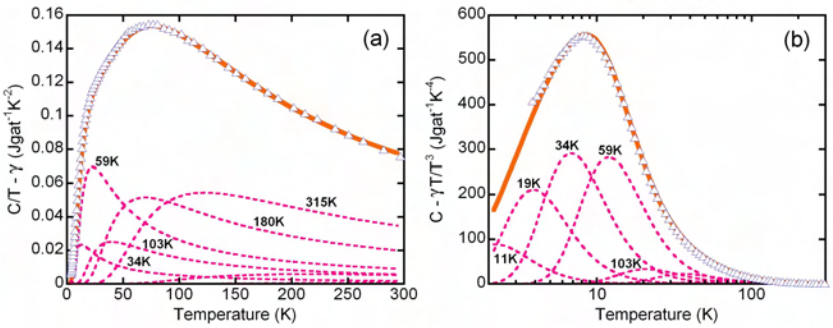

Figure 4.6: (a) Lattice specific heat divided by temperature $C/T - \gamma$ for $In_2Mo_6Se_6$ (triangles) fitted (solid line) by an assembly of Einstein modes (dashed lines). (b) Lattice specific heat normalised by temperature cubed $C - \gamma T/T^3$ (triangles), highlighting the quality of our low temperature fit (solid and dashed lines) and the dominant contribution from the optical mode generated by the In ion.

$$F(\omega) = \sum_k F_k \delta(\omega - \omega_k) \tag{4.4}$$

Using this representation, the lattice specific heat is then given by

$$C(T) = 3R \sum_k F_k \frac{x_k^2 e^{x_k}}{(e^{x_k} - 1)^2} \tag{4.5}$$

where $x_k = \omega_k / T$ and $\omega_{k+1}/\omega_k = 1.75$ to limit the number of modes and provide a stable solution. A least-squares fit of the measured specific heat for each compound was performed and the decomposition into Einstein modes shown for $In_2Mo_6Se_6$ as an example in Fig. 4.6. The fitting technique for $Tl_2Mo_6Se_6$ and $Rb_2Mo_6Se_6$ is identical and the results of a similarly high quality, accurately reproducing our experimental data over the entire temperature range.

The fitted PDoS are shown for each compound in Fig. 4.7 and the results obtained compare very favourably with previous neutron scattering data. [104] All three compounds clearly display the two key features already identified in the C/T plots: a strong narrow peak below $\sim$ 10 meV and a broader distribution of phonons from $\sim$ 10-30 meV. The low-energy peak corresponds to an optical mode formed by the cations "rattling" in the tubes formed between the Mo_6Se_6 chains, whereas the broader maximum is mainly due to intra-chain modes.

Comparing the PDoS of each compound measured, the two superconductors are very similar with a slight spectral weight shift to higher energy in the optical cation mode for $In_2Mo_6Se_6$. This can be explained by considering the smaller atomic mass of In compared to Tl. However, the intensity of the optical mode in $Rb_2Mo_6Se_6$ is significantly reduced and its frequency has been shifted to $\sim$ 8 meV, compared with $\sim$ 4-6 meV in $Tl_2Mo_6Se_6$ and $Rb_2Mo_6Se_6$. Neutron scattering data also showed extensive hybridization of the cation mode with the chain modes in $Rb_2Mo_6Se_6$, thus inducing a deformation in the PDoS from 10-30 meV which can also be seen in our data.

4.3.2 Resistivity and electron-phonon coupling

The resistivity curves from 0.35-300 K for each compound are shown in Fig. 4.8. $Tl_2Mo_6Se_6$ and $In_2Mo_6Se_6$ both show linear metallic behaviour in the normal state. There is no evidence for any negative curvature resulting from strong correlations or the Luttinger liquid electronic ground state predicted to exist in the extreme one-dimensional

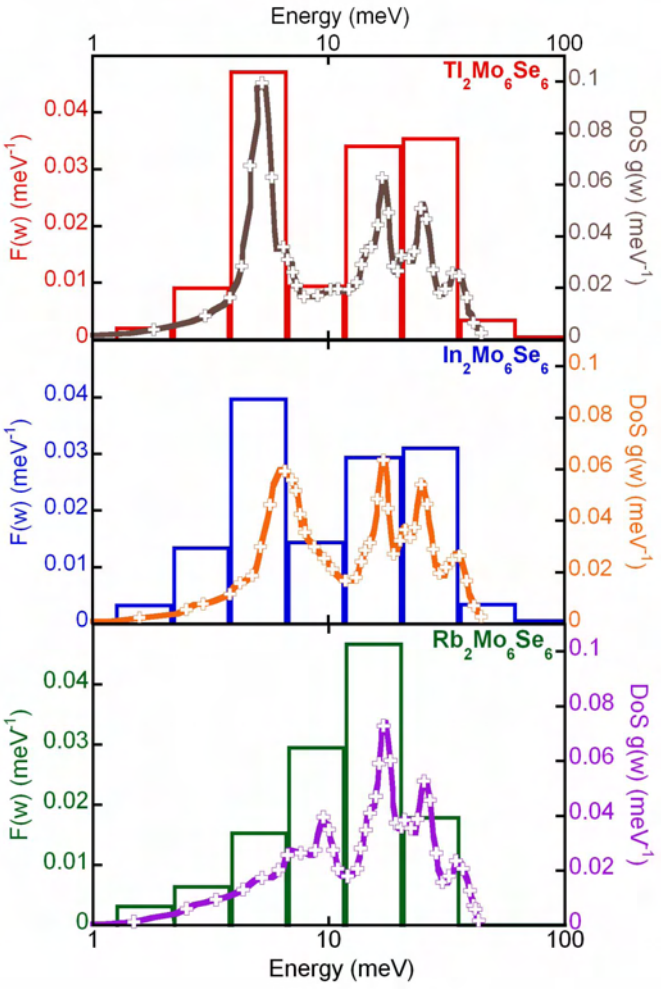

Figure 4.7: Measured phonon density of states for $Tl_2Mo_6Se_6$, $In_2Mo_6Se_6$ and $Rb_2Mo_6Se_6$ (histograms) plotted on a logarithmic energy scale with PDoS data from neutron scattering (crosses).

limit [113]. A saturation in the resistivity is observed for $T < 15$ K in $Tl_2Mo_6Se_6$ and $In_2Mo_6Se_6$, with residual resistivity ratios of 10.1 and 8.8 respectively. Conversely, $Rb_2Mo_6Se_6$ undergoes a broad metal-insulator transition with a minimum at T_c = 170 K and an activation

energy E_A = 173K.

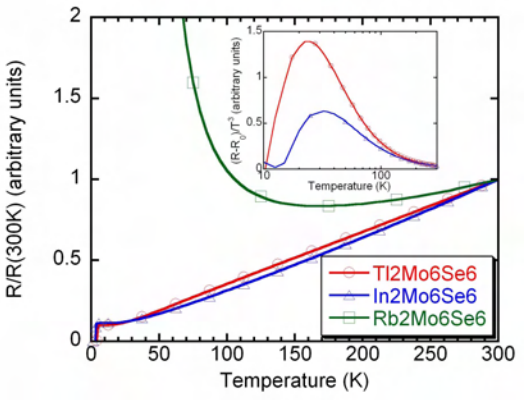

Figure 4.8: Resistivity in $M_2Mo_6Se_6$ normalised to 300K. Inset: low-temperature resistivity in $Tl_2Mo_6Se_6$ and $In_2Mo_6Se_6$ normalised to T^3 after residual subtraction, highlighting the large contribution from low-energy phonons in $Tl_2Mo_6Se_6$.

Using the same phonon frequency bins as those used to calculate the PDoS, we may now evaluate the electron-phonon coupling from the normal-state resistivity data for $Tl_2Mo_6Se_6$ and $In_2Mo_6Se_6$. It is not possible to perform this analysis on $Rb_2Mo_6Se_6$, due to the metal-insulator transition. This procedure has been successfully used to obtain the electron-phonon coupling in ZrB_{12} [114] and YB_6 [115] and a more detailed account of the method can be found in the references. Our departure point is the generalised Bloch-Grüneisen formula [116]:

$$\rho_{BG}(T) = \rho(0) + \frac{4\pi m^*}{ne^2}\int_0^{\omega_{max}} \alpha_{tr}^2 F_\omega \frac{xe^x}{(e^x-1)^2 d\omega} \tag{4.6}$$

where $x \equiv \omega/T$ and $\alpha_{tr}^2 F_\omega$ is the electron-phonon "transport coupling function" which can be decomposed into Einstein modes to give

$$\alpha_{tr}^2 F_\omega = \frac{1}{2}\sum_k \lambda_{tr,k}\omega_k \delta(\omega - \omega_k) \tag{4.7}$$

Substituting this back into equation 4.6 yields the discrete version of the Bloch-Grüneisen equation:

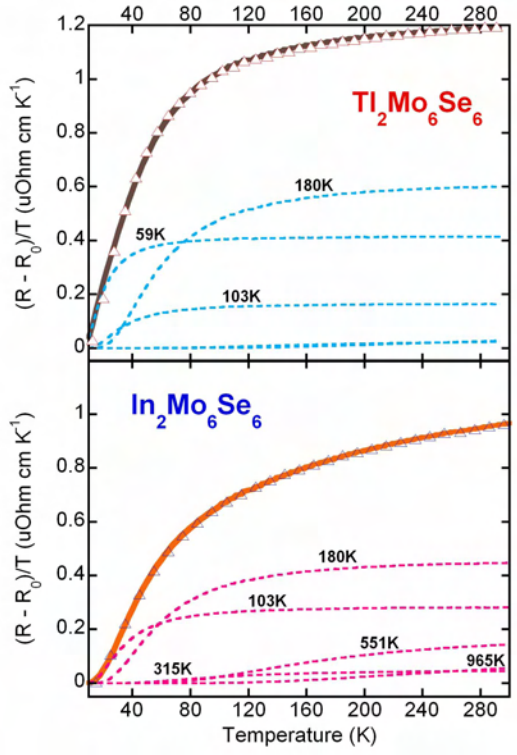

Figure 4.9: Resistivity (with residual subtracted) normalised by T and fitted with the same Einstein mode energies used for the PDOS determination from our specific heat data.

$$\rho_{BG}(T) = \rho(0) + \frac{2\pi}{\epsilon_0 \Omega_p^2} \sum_k \lambda_{tr,k} \omega_k \frac{x_k e^{x_k}}{(e^{x_k} - 1)^2} \tag{4.8}$$

where the mode weighting parameters are the dimensionless constants $\lambda_{tr,k}$. The residual resistivity $\rho(0)$ is determined separately from the raw data, equalling 39.5 $\mu\Omega$ cm for $Tl_2Mo_6Se_6$ and 37.2 $\mu\Omega$ cm for $In_2Mo_6Se_6$.

Our fits are shown in Fig. 4.9 and display a clear difference between $Tl_2Mo_6Se_6$ and $In_2Mo_6Se_6$. The initial slope of $(R - R_0)/T$ is much steeper in $Tl_2Mo_6Se_6$, due to a large contribution from a mode with energy 52 K. In contrast, the lowest energy mode contributing to

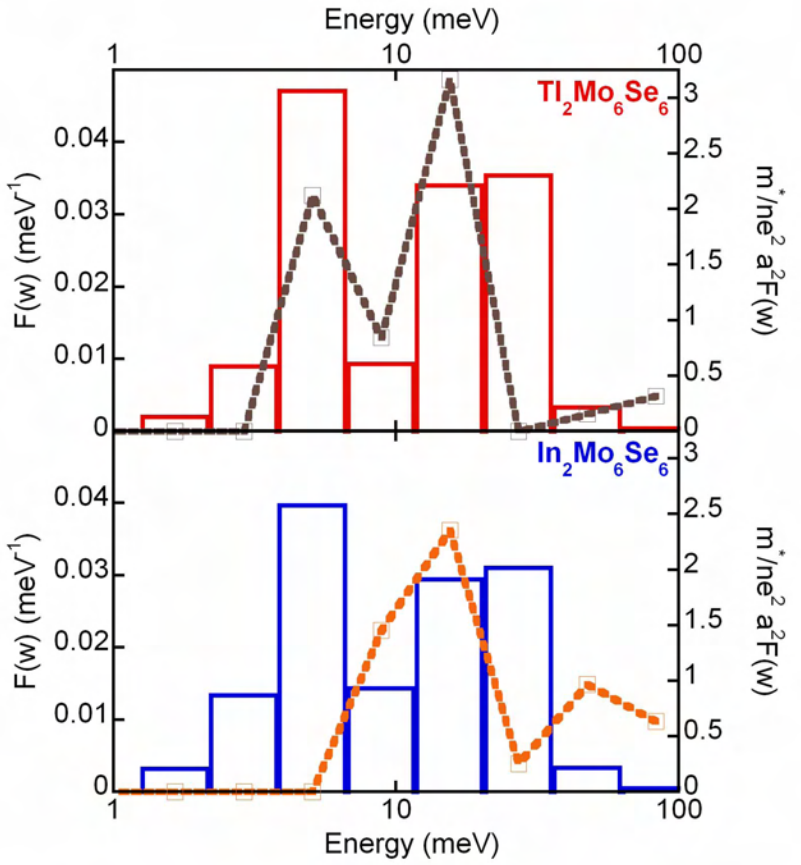

Figure 4.10: Phonon density of states (histogram) and normalised electron-phonon transport coupling function $\alpha^2_{tr}F_\omega$ (line) for $Tl_2Mo_6Se_6$ and $In_2Mo_6Se_6$.

the resistivity in $In_2Mo_6Se_6$ is centred at 91 K, with the first significant contribution only arriving at 160 K. In the absence of any data in the literature for the carrier density n, we decompose the unscreened plasma frequency $\Omega_p^2 = ne^2/\epsilon_0 m^*$ and express our fitted values for $\alpha^2_{tr}F_\omega$ normalised by ne^2/m^*. These are displayed in Fig. 4.10, superimposed on the PDoS.

The principal electron-phonon coupling for each compound occurs in the 10-18 meV frequency window. However, $Tl_2Mo_6Se_6$ also ex-

hibits a major coupling in the 3.5-6 meV region, in direct contrast with $In_2Mo_6Se_6$, which shows no coupling at all below 6 meV. $\alpha^2_{tr}F_\omega$ is intimately related to α^2F_ω, the electron-phonon coupling function governing superconductivity [117], implying an additional electronic coupling to the low-energy rattling phonon in $Tl_2Mo_6Se_6$.

4.4 Discussion

4.4.1 Superconducting transitions

$Tl_2Mo_6Se_6$ and $In_2Mo_6Se_6$ both display an anomalous broadening of their resistive superconducting transitions, whose amplitude and variation under applied field is not compatible with conventional 3D thermal fluctuation models. This suggests that the quasi-1D nature of these compounds has a significant influence on the size of the critical region around T_c. In 3D systems, the broadening of a superconducting transition under applied magnetic field is due to a finite size effect [69]: the vortex-vortex separation limits the divergence of the correlation length at T_c, hence reducing the coherence volume and increasing the importance of thermal fluctuations. In contrast, a perfect 1D system cannot undergo a phase transition due to insufficient degrees of freedom. $Tl_2Mo_6Se_6$ and $In_2Mo_6Se_6$ lie in the crossover regime between these two extremes.

Developing a theoretical model for this transition region is a difficult task; however, we may consider the Peierls transition as an analogous crossover from a quasi-1D system to a quasi-3D ordered state. Theory predicts a suppression of T_c by a factor of up to 4, together with a light smearing of the transition [118] and certain Peierls systems indeed exhibit significantly broadened "jumps" in their resistivity as a result of quasi-1D fluctuations [119]. It therefore seems reasonable to attribute the broadening in $Tl_2Mo_6Se_6$ and $In_2Mo_6Se_6$ to the extreme low-dimensional nature of the compound.

Explaining why this effect is so much more noticeable in $Tl_2Mo_6Se_6$ than $In_2Mo_6Se_6$, particularly in the specific heat jump, is rather harder especially given that $In_2Mo_6Se_6$ is more anisotropic. The calculated 3D Ginzburg number G_{3D} for $Tl_2Mo_6Se_6$ is only 10% larger than that of $In_2Mo_6Se_6$ and, in any case, $G_{3D}T_c$ is several orders of magnitude too small to explain the observed broadening. Calculating the 1D Ginzburg parameters G_{1D} from the Mishonov model yields more realistic transition width amplitudes, although the fact that the measured transition

width for $Tl_2Mo_6Se_6$ is larger than that of $In_2Mo_6Se_6$ implies that this sample was less intrinsically homogeneous.

The evolution of G_{1D} with applied magnetic field has not yet been calculated for a superconducting nanowire and we were hence unable to track the broadening of the resistive transition using a low-dimensional model. However, we expect that a field-induced finite size effect similar to that seen in 3D systems should control the transition widths. The crucial factor here is the difference in coherence volumes $\xi_\perp^2\xi_\parallel$ between the two superconductors: 5290 nm^3 for $Tl_2Mo_6Se_6$ and 11400 nm^3 for $In_2Mo_6Se_6$. It is well known that low-dimensional fluctuations play an increasingly important rôle upon the reduction of coherence length in a material; the smaller coherence volume in $Tl_2Mo_6Se_6$ must therefore outweigh its lower anisotropy relative to $In_2Mo_6Se_6$. Even still, the scale of the deformation of the specific heat jump in $Tl_2Mo_6Se_6$ is unexpectedly large, given that its coherence volume is roughly only twice as small as that of $In_2Mo_6Se_6$.

It is clear that our understanding of low-dimensional fluctuations at a superconducting transition would greatly benefit from a detailed theoretical analysis. In particular, the reproducible deformation of the specific heat jump in $Tl_2Mo_6Se_6$ (which presumably results from a displacement of states from above T_c to the back of the jump) is a remarkable phenomenon which has not been seen in any other quasi-1D superconductor and merits further attention.

4.4.2 Electron-phonon coupling

Our BCS s-wave fits of the specific heat below T_c display conventional weak coupling ($2\Delta_0/k_BT_c$ = 3.4) for $In_2Mo_6Se_6$ and extremely strong coupling ($2\Delta_0/k_BT_c \geq 5$) for $Tl_2Mo_6Se_6$. In fact, $Tl_2Mo_6Se_6$ may well have usurped the throne of the β-pyrochlore KOs_2O_6 ($2\Delta_0/k_BT_c \geq 5$) as the strongest-coupling phonon-mediated superconductor currently known. It should be noted that abnormally strong coupling (ranging up to $2\Delta_0/k_BT_c \sim 25$) is a characteristic of several quasi-1D CDW systems such as $NbSe_3$ and $(TaSe_4)_2I$ [120, 121], due to the transition temperature being suppressed below its mean-field value. However, given that $In_2Mo_6Se_6$ is more anisotropic than $Tl_2Mo_6Se_6$, we do not believe that the strong coupling in $Tl_2Mo_6Se_6$ originates from its low dimensionality.

Deconvolving the normal-state resistivity shows that the predominant electron-phonon coupling for $Tl_2Mo_6Se_6$ and $In_2Mo_6Se_6$ lies in the 10-18 meV range, implying that superconductivity is mediated by the internal chain modes which (according to neutron diffraction experi-

ments [104]) range from 12-40 meV and peak strongly at 17 meV. This interpretation is supported by a tentative report of superconductivity under pressure in Mo_6Se_6 [108]. The additional coupling to the low-energy optical mode in $Tl_2Mo_6Se_6$ moves this superconductor into the extreme strong-coupling regime, increases T_c by nearly 2 K and reduces the coherence volume $\xi_\perp^2 \xi_\parallel$, rendering the superconducting transition more susceptible to broadening through quasi-1D fluctuations.

Our observation immediately begs the question why $In_2Mo_6Se_6$ does not enjoy a similar coupling to its optical In^+ mode. There are two reasons for this: firstly, consider the variation of the hexagonal lattice parameter a and the Pauling radii R_p of the Tl^+, In^+ and Rb^+ monovalent cations. Values for a measured by X-ray diffraction [32, 100] in $Tl_2Mo_6Se_6$, $In_2Mo_6Se_6$ and $Rb_2Mo_6Se_6$ are given in Table 4.2, together with standard R_p values from the literature. Each cation is located at $a/\sqrt{3}$ from three equidistant Mo_6Se_6 chains and, since the chain radius is invariant with respect to the cation, the ratio $a/\sqrt{3}R_p$ gives a good measure of the freedom of the respective cations to vibrate in their interchain tunnels.

Table 4.2: Lattice parameters a and cation radii R_p in $M_2Mo_6Se_6$

	a (Å)	R_p (Å)	$a/\sqrt{3}R_p$
$Tl_2Mo_6Se_6$	8.94	1.15	4.48
$In_2Mo_6Se_6$	8.85	1.04	4.90
$Rb_2Mo_6Se_6$	9.26	1.48	3.61

It can clearly be seen that the In^+ ion is less geometrically constrained than Tl^+ and that Rb^+ is at considerably less liberty to vibrate than either of its "superconducting" counterparts. This is evident in the neutron scattering data: as pointed out by Brusetti *et al.*, $Rb_2Mo_6Se_6$ displays significant hybridisation of the low-energy Einstein phonon, with the higher-energy internal chain modes corresponding to a $\sim$40% increase in the M-ion force constants. Upon closer examination, the neutron-imaged PDOS of $In_2Mo_6Se_6$ has a slightly deeper trough at $\sim$11 meV than $Tl_2Mo_6Se_6$, implying marginally less phonon hybridisation, which is consistent with our estimate above. We therefore believe that the interchain tunnel diameter in $In_2Mo_6Se_6$ is simply too large relative to the In^+ ion to allow its low-energy phonon to effectively couple to the Mo d electrons at the Fermi level in the chains.

Secondly, the intrinsic electron-phonon coupling strength λ is proportional to $1/\omega^2$, where ω is the characteristic phonon frequency [116].

Due to its smaller mass, the In^+ mode is shifted to higher energy as can be seen both in our PDOS histograms and the neutron data from Brusetti in Fig. 4.7. Using the Tl^+ = 5.2 meV and In^+ = 6.3 meV mode energies from ref. [104], we calculate $\omega^2_{\mathrm{In}}/\omega^2_{\mathrm{Tl}}$ = 1.47; i.e. the coupling to the Tl^+ mode should be nearly 50% stronger than that to the In^+ mode. To make a very crude comparison, we sum our measured α^2F_ω from Fig. 4.10 in the relevant energy range 5.1 - 8.9 meV, obtaining $\Sigma\ \alpha^2F_\omega(\mathrm{Tl})/\Sigma\ \alpha^2F_\omega(\mathrm{In})$ = 2.04. This suggests that the frequency-dependent variation in coupling strength and the geometric constraints on the guest ion mode have a roughly equal importance in determining the coupling in $M_2Mo_6Se_6$.

Naively, we might expect an enormous electron-phonon coupling and ultra-strongly-coupled superconductivity in $Rb_2Mo_6Se_6$ due to its narrow effective tunnel diameter. However, the recent band structure calculations detailed in section 3.3.2 [97] indicate that it is not the geometric constraints on the M-atom in $M_2Mo_6Se_6$ which determine its anisotropy, but rather the degree of warping in its Fermi sheets, i.e. the linewidth of the d band at the Fermi level as illustrated in Fig. 3.8.

This warping arises from a hybridisation of the Mo d band with M ion electronic states lying above the Fermi level: p states for Tl, In and s states for Rb and the rest of the Group IA ions. The degree of hybridisation is inversely proportional to the electropositivity of the M ion. Group IA metals are much more electropositive than Group III, causing $Rb_2Mo_6Se_6$ to undergo a high-temperature metal-insulator transition rather than a superconducting transition at low temperature. In a similar fashion, In is more electropositive than Tl, leading to the increased anisotropy of $In_2Mo_6Se_6$ compared to $Tl_2Mo_6Se_6$. Despite the lack of any indications of a high-temperature Luttinger ground state, the quasi-1D nature of these compounds is in strong evidence due to the wide fluctuation-dominated regions around both superconducting and metal-insulator transitions.

Having explained the T_c variation between $Tl_2Mo_6Se_6$ and $In_2Mo_6Se_6$, it now remains for us to elaborate on the reasons for the lack of superconductivity observed in $Rb_2Mo_6Se_6$. A deeper examination of the metal-insulator transition will therefore constitute the focus of the next chapter. In particular, we clarify the competition between superconducting and insulating phases, identifying the critical rôle of the Fermi surface warping in determining the groundstate of $M_2Mo_6Se_6$.

Chapter 5

Anomalous Metal-Insulator Transitions in $M_2Mo_6Se_6$

Shortly after their discovery, it was realised that the M = Group IA ion members of the $M_2Mo_6Se_6$ family did not become superconducting at low temperature [93, 107]. From DC transport measurements - one of relatively few appropriate experimental probes available at that time - a broad minimum was observed in the resistivity at temperatures ranging from 80 - 200 K for M = Na, K, Rb, followed by an exponential resistive increase at low temperature reminiscent of semiconducting behaviour.

However, band structure calculations have indicated that there is a half-filled band at the Fermi level, as suggested by the high-temperature metallic resistivity. This leads to questions over the nature of the metal-insulator (MI) transition. There are several candidate mechanisms available: some exotic, others more conventional. Due to the one-dimensional nature of these compounds, the most obvious choice is a charge density wave (Peierls) transition with associated phonon softening and a characteristic doubling of the c axis lattice parameter due to the $2k_F$ structural modulation [122]. Nevertheless, on the basis of several rather limited transport measurements it is not possible to conclusively identify the nature of the MI transition and clarify its coexistence or competition with superconductity. In this chapter, we therefore combine the data in the literature with new transport, tunnelling and low-temperature X-ray diffraction experiments in the hope

of solving the last mystery of $M_2Mo_6Se_6$.

5.1 The Case for a Charge Density Wave

All work on $M_2Mo_6Se_6$ in the literature has automatically assumed (with minimal experimental justification) that the low-temperature insulating phase is either a charge density wave (CDW) or a spin density wave (SDW), resulting from the one-dimensional nature of the crystal structure. We feel it is safe to rule out a SDW as being responsible for the MI transition, given that the magnetic susceptibility is small and weakly diamagnetic from room temperature down to 2 K for all compounds [93, 98]. However, given the observation of broadband noise in differential resistance measurements [109], the CDW scenario deserves careful attention.

5.1.1 Electrical transport

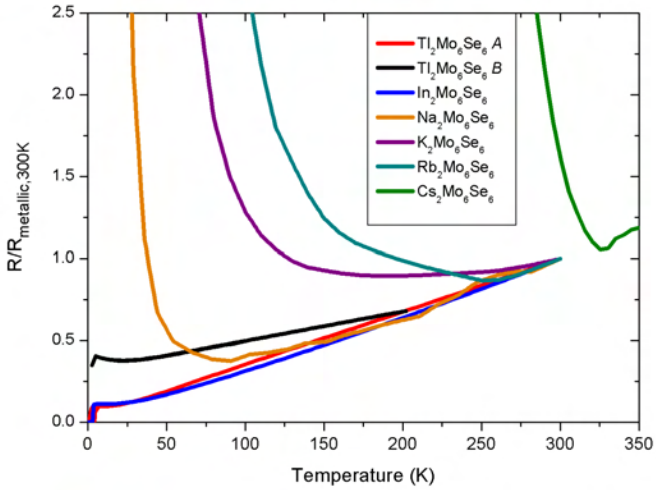

Figure 5.1: AC Resistivity in MMoSe. Values are normalised to the metallic resistivity at 300 K (extrapolated for $Cs_2Mo_6Se_6$)

In Fig. 5.1 we display the normalised resistivity $\rho(T)$ in $M_2Mo_6Se_6$, measured using our standard four-wire AC technique in the PPMS. Both A and B phases of $Tl_2Mo_6Se_6$ are shown for comparison. We

identify T_{MI} as the temperature corresponding to the minimum in the normal-state resistivity. Activation energies are calculated using

$$E_a = \frac{dlnR}{dT^{-1}} \tag{5.1}$$

for the initial exponential growth at T < T_{MI}. In a semiconductor, E_a is proportional to the gap value. The values obtained are summarised in Table 5.1.

Table 5.1: Metal-insulator transition temperatures T_{MI} and activation energies E_a in $M_2Mo_6Se_6$

	T_{MI} (K)	E_a (K)
$Tl_2Mo_6Se_6$	22 ± 1	0.7 ± 0.1
$Na_2Mo_6Se_6$	91 ± 1	45 ± 5
$K_2Mo_6Se_6$	189 ± 1	88 ± 10
$Rb_2Mo_6Se_6$	252 ± 1	122 ± 10
$Cs_2Mo_6Se_6$	330 ± 2	203 ± 20

It is immediately obvious that the metal-insulator transition seen in $M_2Mo_6Se_6$ is very broad and continuous compared with the distinct steps seen in other CDW materials such as $NbSe_3$ or TaS_2 [119, 123]. Tarascon [93] and Hor [107] have also performed resistivity measurements on $Rb_2Mo_6Se_6$, obtaining $T_c \sim$ 125 K, 104 K and E_a = 87 K, 145 K respectively, which are rather smaller than our values $T_c \sim$ 252 K and E_a = 122 K. We attribute these differences in T_c to variations in sample anisotropy, resulting from slight differences in the stoichiometries. It is well-known that $Tl_2Mo_6Se_6$ is not a perfectly stoichiometric compound [111], with the highest superconducting T_c occurring in $Tl_{1.95}Mo_6Se_6$. Similar non-stoichiometric behaviour occurs in the rest of the $M_2Mo_6Se_6$ family, for example producing occasional batches of $In_2Mo_6Se_6$ which are non-superconducting [99, 100].

Playing devil's advocate for a moment, let us assume that a CDW is indeed present at low temperature in $M_2Mo_6Se_6$. In this case, it would arise due to the significant degree of nesting of the warped planar Fermi surface (FS) described in section 3.3.2. As we move down Group IA from *M* = Na → Cs, the FS becomes progressively less warped and more plate-like due to the increasing electropositivity of *M*. The nesting factor therefore increases, with the majority of the two Cs Fermi planes linked by a single $2k_F$ wavevector as illusrated in Fig. 5.2.

Following this trend, we would expect to see CDW transition temperatures rise as we move from Na → Cs. As shown in Fig. 5.1 and

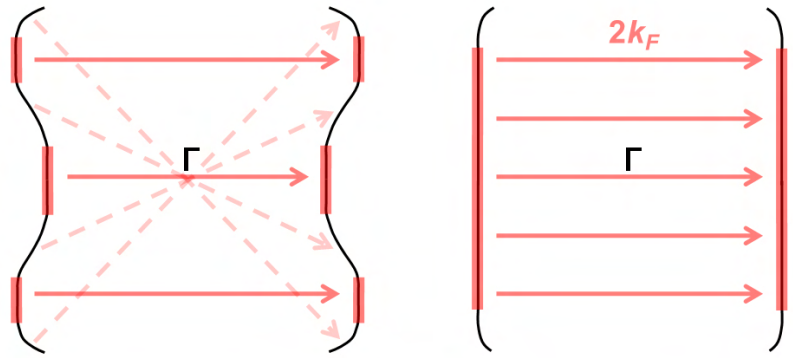

Figure 5.2: Nesting schematics for quasi-one-dimensional Fermi surfaces in *M* = Group III ion (left) and *M* = heavy Group IA ion (right). The increasing nesting factor as *M* moves down Group IA renders $M_2Mo_6Se_6$ more susceptible to a CDW transition.

Table 5.1, this is indeed observed. Assuming a universal Peierls-mode electron-phonon coupling in $M_2Mo_6Se_6$, the gap resulting from the formation of any CDW should also increase with T_{MI}. Once again, this agrees with our data since E_a increases down the group. It should be noted that E_a cannot give an absolute measure of the gap size since it is derived from a transport experiment and will be influenced by several other factors. In particular, with such a low-dimensional crystal structure any defects will act to couple the chains, thus increasing the local conductivity. As in a semiconductor, impurities will also contribute electrons or holes to the system, increasing its conductivity.

Re-examining the literature, Tarascon *et al.* reported $Cs_2Mo_6Se_6$ to have a higher T_{MI} than $Rb_2Mo_6Se_6$ [93], which is in line with the CDW hypothesis. Hor *et al.* [107] have shown that hydrostatic pressure (leading to an enhanced interchain coupling and reduced anisotropy) suppresses T_{MI} to lower temperatures, also suggesting that T_{MI} simply scales with the area of the FS available for CDW nesting. However, Mo_6Se_6 (the extreme low-dimensional limit of the $M_2Mo_6Se_6$ family) remains metallic down to 5 K, [94] implying that quasi-1D fluctuations may suppress the CDW transitions in $M_2Mo_6Se_6$ below their mean-field values.

5.1.2 Tunnelling spectroscopy

Any density wave transition should create a symmetric gap around the Fermi level in the electronic density of states. Furthermore, the structural modulation associated with a CDW may be visible as an atomic displacement on the surface. Tunnelling spectroscopy is therefore an excellent weapon in the hunt for density waves, since it is capable of probing both the topography and LDoS of a sample.

Unfortunately, conventional STS on $M_2Mo_6Se_6$ is a considerable challenge owing to a generally sub-optimal surface quality. Due to the q1D crystal structure, any attempt to cleave the crystals results at best in a "forest" of loose fibres above a flat (100) surface and at worst in an incoherent mess. Surface mechanical instabilities lead to an interaction between the sample and tip, producing a large oscillation in the scanner height z and rendering any measurement impossible. After numerous failed attempts at measuring the (100) plane of $Tl_2Mo_6Se_6$ (the most mechanically stable member of $M_2Mo_6Se_6$) using an Ir tip, a change of tactic was required. Rather than tunnel into the sample, we use the sample as the STM tip and tunnel parallel to the chain axis (001) into an Au(111) thin film. While this approach obviously removes any spatial resolution and hence rules out topographic investigations, it circumnavigates the problem of poorly-oriented or unstable surfaces.

Although this is an ongoing topic of research, several very preliminary results on $K_2Mo_6Se_6$ and $Rb_2Mo_6Se_6$ are illustrated in Fig. 5.3. As is conventional in semiconductor spectroscopy, the differential conductance $\frac{dI}{dV}$ is normalised by $\frac{I}{V}$ to facilitate the measurement of any gap. Although we are able to obtain a stable tunnel junction with this configuration, our measurements are highly susceptible to the semiconducting impurities which persist despite cleaning the as-grown surfaces with hydrochloric acid, acetone and ethanol. In particular, it is difficult to distinguish a semiconducting gap or pseudogap which is superimposed on a similar background. For this reason, we normalise our low-temperature data to the semiconducting spectra measured at room temperature.

Referring to equation 1.5, the tunnel current is proportional to the convolution of the tip DoS and the sample LDoS. Since the LDoS of the Au(111) film should be constant close to E_F, in this configuration we should be directly probing the DoS of the tip. However, equation 1.5 was derived by approximating the tip wavefunction as being spherically symmetric. It is clear that such an approximation is no longer valid for q1D $M_2Mo_6Se_6$ and hence we must reconsider the tunnelling matrix

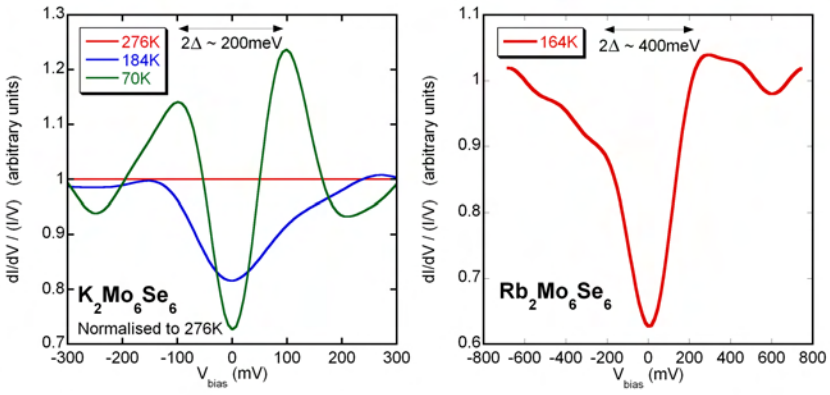

Figure 5.3: Preliminary tunnelling spectra obtained in $K_2Mo_6Se_6$ (left) and $Rb_2Mo_6Se_6$ (right) using single crystals as STM tips and tunnelling into a Au(111) film. $K_2Mo_6Se_6$ spectra are normalised to the 276 K data and the $Rb_2Mo_6Se_6$ data is normalised at 750 meV.

element. This problem is far from straightforward and we tentatively propose a very crude analysis, assisted by the highly one-dimensional nature of the $M_2Mo_6Se_6$ "helix" band at E_F. Assuming a single tunnelling channel into an isolated Mo_6Se_6 chain, the matrix element $|T_{ts}|$ should remain proportional to the modulus of the tip wavefunction at the Au(111) surface $|\psi_t(z)|$. This scenario is reminiscent of the planar junction geometry studied by Harrison [46]; we therefore consider our spectra to be proportional to the local density of states.

A pseudogap clearly opens in $K_2Mo_6Se_6$ as the temperature is reduced below T_{MI}, developing peaks at the gap edges at low temperature. These peaks are particularly unusual and warrant further attention: similar features have been observed in colossal-magnetoresistant manganites, where they were interpreted as signatures of coherent polaronic transport [124]. A depression in the DoS around E_F is also visible in $Rb_2Mo_6Se_6$ below T_{MI}. Although it is difficult to make a quantitative assessment given the semiconducting background and high measurement temperature, the zero-bias conductance (ZBC) seems too high for the FS to be fully gapped, implying an imperfect nesting as would be expected for warped Fermi planes. In order to verify this, a systematic tunnelling study of all $M_2Mo_6Se_6$ would be required: in principle, the ZBC should decrease moving down Group IA. Nevertheless, the pseudogap imaged in this preliminary data is entirely compatible

with a CDW scenario.

Recent ARPES measurements have indicated a depletion in spectral weight around E_F in the Group IA members of $M_2Mo_6Se_6$ upon cooling below T_{MI} [125]. While these results are "even more preliminary" than the STM spectra shown above, they are qualitatively in agreement with the formation of a pseudogap. A more extensive investigation is planned imminently.

5.2 The Case Against a $2k_F$ Charge Density Wave

Some of the most elegant and irrefutable observations of CDWs have been made by directly measuring the structural modulation occurring below T_{MI}, which for a $2k_F$ CDW should result in a doubling of the c-axis lattice parameter. X-ray diffraction (XRD) provides the easiest method of structural determination and we have therefore performed extensive XRD sample characterisations using the Swiss-Norwegian Beamline at the European Synchrotron Radiation Facility at Grenoble.

5.2.1 Low-temperature X-ray diffraction

Initial room-temperature tests were carried out on high quality single micro-crystals (typical dimensions $1.5 \times 0.1 \times 0.05$ mm using a KUMA κ-CCD detector. We obtain the same crystal structure with space group $P6_3/m$ as originally determined by Potel and co-workers [92] for all $M_2Mo_6Se_6$. Using a helium blower, the Group IA compounds were then cooled to 20 K: a photograph of the experimental configuration is shown in Fig. 5.4.

In a $P6_3/m$ crystal, the (00n) (n odd) Bragg reflections should not be visible due to destructive interference from the crystal mirror symmetry. However, if a CDW transition takes place then the lattice parameter is doubled and (00n) diffraction peaks should be clearly visible. No (00n) were consistently observed at 20 K in any Group IA compound for n = 1-7 (the limit of our resolution). Several isolated (001) and (003) peaks were occasionally observed, but after careful rotation of the crystal these could always be ascribed to Renninger Umweganregung reflection effects rather than any phase transition.

One of the few theoretical treatments of this subject suggests that transition temperatures may be suppressed to as little as 25% of their mean field value in CDW systems due to the impact of low-dimensional

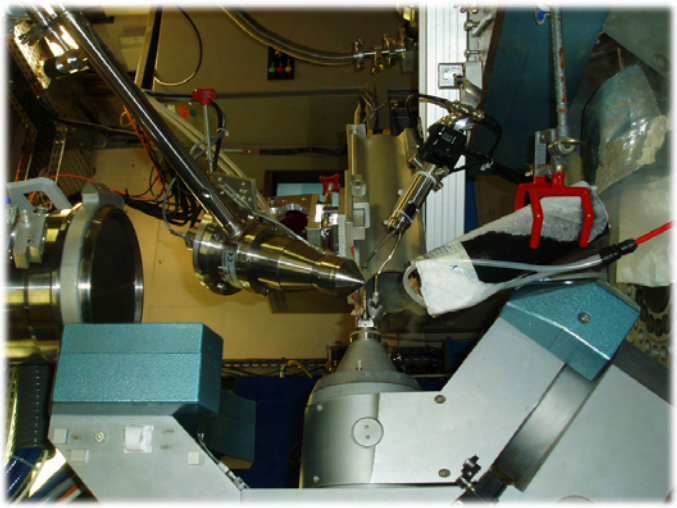

Figure 5.4: Low-temperature single-crystal diffraction at the Swiss Norwegian Beamline, ESRF Grenoble. The crystal is glued to a glass fibre with epoxy just below the centre of the photo, then mounted in a goniometer attached to a κ-geometry arm. The helium blower nozzle is visible to the left of centre, with a low vacuum exhaust to the right in order to limit ice build-up on the crystal.

fluctuations [118]. At 20 K, we are at 6% of T_{MI} in $Cs_2Mo_6Se_6$ (the most one-dimensional member of $M_2Mo_6Se_6$) and still no structural transition has taken place. Unfortunately, it was not possible to perform a full structural determination at 20 K, due to excessive accumulation of ice on the sample during long measurements. Raising the temperature to 82 K, a full structural analysis of $Cs_2Mo_6Se_6$ was performed. In Fig. 5.5, we have superposed the crystal structures resolved at 82 K and 450 K (attained using a hot nitrogen blower).

Apart from the expected thermal expansion (which is too small to be visible on the diagram), there is no change in the c-axis lattice parameter over the entire 368 K temperature range. The a-axis display a larger thermal expansion, as is logical considering the weak bonding of the chains, but once again no structural modulation takes place.

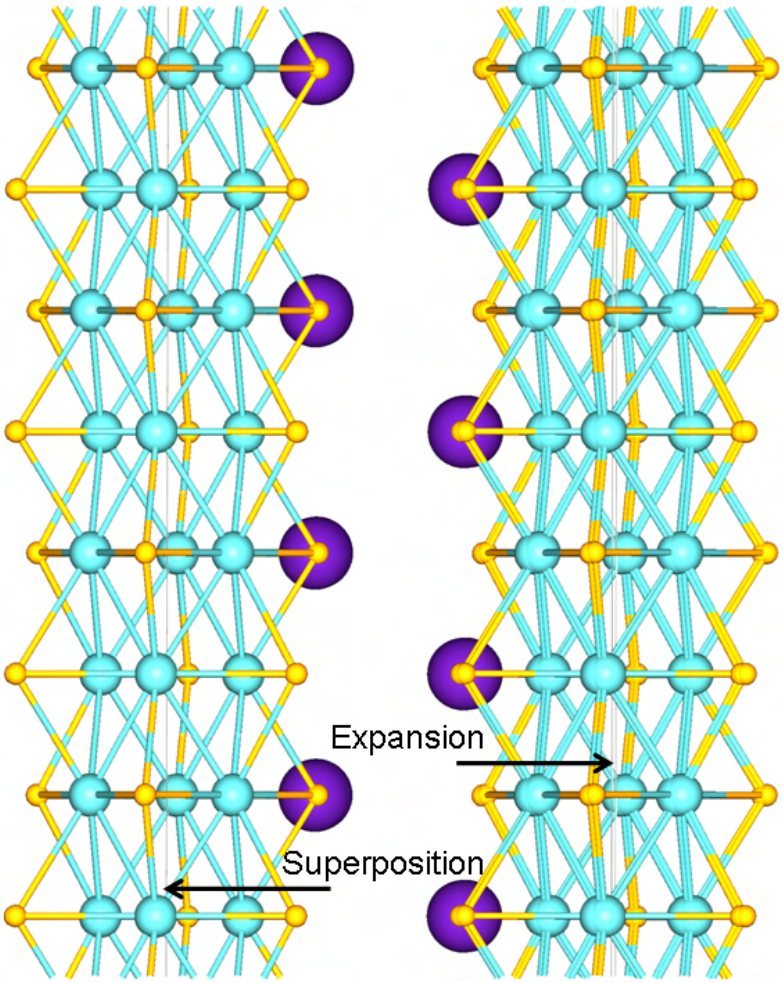

Figure 5.5: $Cs_2Mo_6Se_6$ crystal structures at 82 K and 450 K, obtained by single-crystal X-ray diffraction. Cs ions are purple, Mo blue and Se yellow. The two structures are superposed and centred on the left-hand cluster chain; the small increase in a may hence be seen in the offset in the right-hand chains. The thermal variation in c is too small to be distinguished.

5.2.2 Thermal expansivity from powder diffraction

To further illustrate the lack of any superstructural modulation, powder diffraction experiments were performed using a MAR image plate

detector and nitrogen stream from 80 K to 300 K (450K for $Cs_2Mo_6Se_6$). This permitted a rapid extraction of the variation of the a and c-axis lattice parameters with temperature for all $M_2Mo_6Se_6$, except $Tl_2Mo_6Se_6$ where an unidentifiable parasitical or impurity phase thwarted our data analysis. In Fig. 5.6 we plot the variation of the ratio of the lattice parameters $a/2c$ with temperature, normalised to the 300 K value. As expected from the weak interchain coupling, the gradient is positive throughout. Any structural transition would produce a step in $a/2c$: no discontinuity is observed in any $M_2Mo_6Se_6$ compound and $a/2c(T)$ remains linear for all temperatures studied. This is further confirmation of the lack of any conventional CDW in these materials.

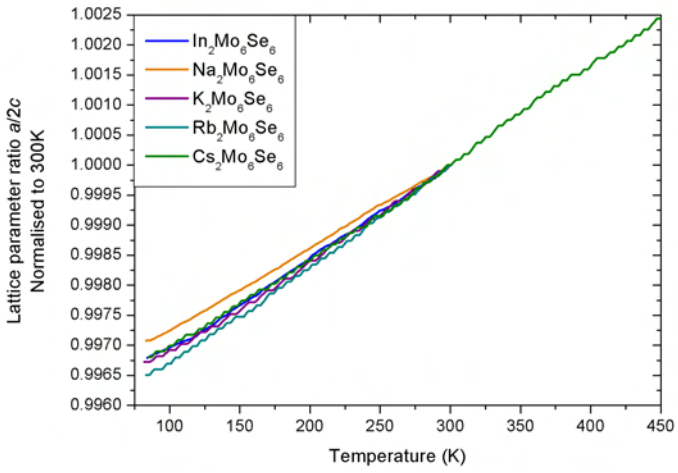

Figure 5.6: Lattice parameter variation with temperature in $M_2Mo_6Se_6$ measured by powder X-ray diffraction.

We note that $a/2c(T)$ is noisier for K, Rb and Cs than for In and Na. The minimum temperature in this experiment was 80 K, which is above T_{MI} in $Na_2Mo_6Se_6$ (and, presumably, B-type $In_2Mo_6Se_6$). Such noise could indicate time-averaged fluctuations of c over the time-scale of a single diffraction measurement (several minutes). Therefore, these data do not rule out a rapidly fluctuating structural instability in $M_2Mo_6Se_6$.

The linear thermal expansivity of a crystal is given by

$$\alpha_i = \frac{1}{l_i}\frac{dl_i}{dT} \tag{5.2}$$

where l is the lattice parameter for crystal axis i. Similar to the heat

capacity, α_i is a second derivative of the free energy and should hence be expected to display a peak at a first order phase transition or a discontinuity at a second order transition. Although this property is more commonly measured using high-resolution capacitance dilatometers (see ref. [114] for an example), as an experiment we have attempted to extract this from our diffraction measurements. An example of the (smoothed) data from $Rb_2Mo_6Se_6$ is shown in Fig. 5.7.

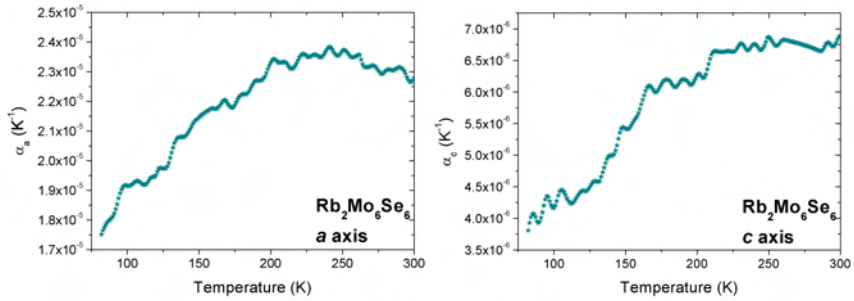

Figure 5.7: Anisotropic thermal expansivities α_a (left) and α_c (right) in $Rb_2Mo_6Se_6$, obtained by numerical derivation.

Unfortunately the results are extremely noisy, due to the limited number of data-points taken during the temperature sweep. There may also be small fluctuating thermal gradients between the thermocouple and the actual sample temperature. The numerical differentiation procedure further accentuates the existing noise in a and c; hence no statistically dependable conclusions may be drawn from these data. However, the discontinuity in α_c at $\sim$ 210 K may possibly be intrinsic and lies in the correct temperature range for T_{MI} in $Rb_2Mo_6Se_6$, which has ranged from $\sim$ 170-260 K [93, 107]. Although this cannot be evidence for a conventional CDW due to the structural arguments already outlined, it may nevertheless be a signature of the MI transition and warrants future experimental attention.

5.3 Unconventional Fluctuating Density Waves

With transport and tunnelling measurements suggesting CDW formation yet XRD seemingly ruling out any CDW with a structural phase transition, we are forced to seek an alternative physical scenario.

It is of course possible for a material to undergo a MI transition in a

band with commensurate filling without any accompanying structural phase transition at low temperature: one example of this is the well-known Mott insulator scenario in which a strong Coulomb repulsion results in on-site electronic localisation [126]. We do not believe this is the case in $M_2Mo_6Se_6$ for three reasons:

- The groundstate of a Mott insulator should be magnetically ordered, either a ferromagnet or an antiferromagnet depending on the exchange interaction. The weak diamagnetic susceptibility observed in $M_2Mo_6Se_6$ conclusively rules out any ferromagnetic ordering. Although low-dimensional fluctuations could in principle suppress antiferromagnetic ordering, at low temperature these effects should be negligible; however $M_2Mo_6Se_6$ remains diamagnetic even at 2 K.

- The bandstructure of $M_2Mo_6Se_6$ is incompatible with the one-dimensional Mott Hubbard model: the separation between the Fermi level and the nearest states above it ($\sim$ 0.2 eV) is much smaller than the typical Coulomb repulsion ($\sim$ 1 eV). On-site electronic localisation hence cannot occur.

- Although bandstructure calculations predict that $M_2Mo_6Se_6$ should be half-filled, the slight M deficiency means that the actual filling will be less than 0.5. In a Mott insulator, incommensurate filling allows charge transport via mobile holes; this tends to suppress any insulating behaviour. Taking high-T_c cuprates as an example, the 2D antiferromagnetic Mott state is able to extend to around 1.5 % hole-doping, compared with a typical 2 % departure from stoichiometry in $M_2Mo_6Se_6$. This alone is insufficient to justify the absence of a Mott scenario. However, as we add holes to cuprates they become more conducting; in contrast as we move further from stoichiometric filling in $M_2Mo_6Se_6$ by removing M ions, the materials become increasingly one-dimensional and insulating. This proves that the driving force behind the M-I transition in $M_2Mo_6Se_6$ is unrelated to the Mott instability.

Another model for the MI transition which initially seems plausible is the excitonic insulator [127]. This has been extended to the q1D limit [128] and is appealing due to its depiction of a transition from semi-metallic to semiconducting régimes. However, upon closer examination the $M_2Mo_6Se_6$ bandstructure is again incompatible with exciton formation, which requires either limited band overlap between valence and conduction bands or an a actual band gap. The broad half-filled

band at E_F in $M_2Mo_6Se_6$ is in principle far too metallic to permit exciton condensation.

It is logical to assume that the low-dimensionality of this system is in some way responsible for the MI transitions, particularly as we have observed that T_{MI} scales with the linewidth at E_F (see Fig. 3.8). In the extreme one-dimensional limit, electrons switch from Fermi liquid to Luttinger liquid behaviour [129]. Within the Luttinger model, free electrons are replaced by collective modes and phase transitions are completely suppressed due to the insufficient degrees of freeom. However, the predicted power-law resistivity [130] is at odds with our observed exponential decay in $\rho(T)$ as T increases.

While considering the nature of the MI transition, one should also bear in mind the possibility of superconductivity in $Tl_2Mo_6Se_6$ and $In_2Mo_6Se_6$ arising from a semiconducting ground state, as suggested by the Hall effect results from Brusetti *et al.* [111] and the $\rho(T)$ behaviour of B-type samples. In order to explain the Hall data in $Tl_2Mo_6Se_6$, a partial CDW gradually depleting the Fermi surface as temperature decreases could be envisaged. This model could explain the observed crossover from electron-like to hole-like carriers, yet it would still require a corresponding (and unphysical) increase in carrier mobility below 80 K to explain the linear metallic resistivity.

Remaining with $Tl_2Mo_6Se_6$ and $In_2Mo_6Se_6$ for a moment, if we postulate that the inter-chain coupling is sufficiently strong for q1D fluctuations to be negligible then a theoretical CDW model may be invoked [131] which defines two separate transition temperatures: T_{cu} at which the CDW distortion occurs and T_{cl} at which an energy gap opens over the entire Fermi surface and a metal-insulator transition occurs. Despite the presence of a structural modulation, metallic behaviour persists in the intermediate temperature range $T_{cl} < T < T_{cu}$ whose width is acutely dependent on the anisotropy. Using this model and the Brusetti Hall coefficient crossover data [111], we could identify T $\sim$ 80 K as T_{cu} in $Tl_2Mo_6Se_6$ and assume that the superconducting transition takes place at $T_c > T_{cl}$.

However, this model incorporates an obligatory structural transition: any attempt to apply it to the Group IA compounds would force us to conclude that T_{cu} $>$ 300 K for the entire group. This is clearly incompatible with our resolved crystal structures. More importantly we cannot justify disregarding quasi-1D fluctuations (as required by the model) when they are manifested so clearly in the deformation of the specific heat jump below T_c in the least one-dimensional compound $Tl_2Mo_6Se_6$ (Fig. 4.4 (a), (b), (d)).

Recent work on $(TaSe_4)_2I$ has suggested the existence of so-called unconventional CDWs (UCDWs) with an average gap of zero at the Fermi surface due to a wave-vector-dependent CDW order parameter [132]. The related theoretical model suppresses the Peierls transition temperature well below its mean-field value, with the energy gap (the order parameter) fluctuating in time and space between these temperatures [133]. This scenario is supported by photoemission data on the quasi-1D compounds $K_{0.3}MoO_3$ and $(TaSe_4)_2I$ [134]. Two types of UCDW may be distinguished: phonon-mediated (which should combine a homogeneous electronic distribution with a lattice modulation) and electronic UCDWs (which do not have any lattice modulation). A pseudogap should open in the DoS, thus accounting for the rise in resistivity. This pseudogap is in qualitative agreement with our STS measurements in $K_2Mo_6Se_6$ and $Rb_2Mo_6Se_6$; our observed lack of any structural transition is also supportive of an electronic UCDW model.

Another type of electronic CDW exists: the $4k_F$ density wave. A full mathematical derivation of this instability requires the introduction of long-range interactions into the Luttinger liquid (LL) model and is far beyond the scope of this discussion: more details can be found in chapter 4 of ref. [130]. Essentially, a $4k_F$ density wave is a one-dimensional Wigner crystal; microscopically it is identical to a half-filled Mott insulator although the physical origin of each phase is different. The progressive electronic localisation expected with such a Wigner crystallisation in a strongly-fluctuating 1D system perfectly explains the Hall crossover from electron to hole transport, does not have an associated lattice modulation and should generate a pseudogap around E_F, thus agreeing with all our observations.

After careful reflection, we therefore believe that a fluctuating electronic charge density wave is the most likely candidate to be responsible for the MI transition in $M_2Mo_6Se_6$. All other theoretical MI models fail to reproduce one or more aspects of our experimental data or bandstructure calculations. The groundstate of this phase should be antiferromagnetic; however we believe that any spin correlations will be suppressed by low-dimensional fluctuations.

Despite the electronic (U)CDW being a direct consequence of the strong electronic anisotropy and the repulsive Coulomb interaction, it should be noted that the existence of such a phase does not violate our assertion that strong LL correlations and a Mott instability are both absent in $M_2Mo_6Se_6$. Unlike a classic $2k_F$ CDW, it does not rely on strong electron-phonon coupling and a Peierls phonon to provoke the MI transition. Inelastic X-ray scattering measurements have

so far failed to reveal any evidence for a softening of the Peierls mode in the Mo_6Se_6 chains [106], supporting our electronic CDW scenario. Should any phonon softening effects be detected, it will be necessary to reassess the likelihood of a fluctuating Peierls transition, not to mention re-evaluating our understanding of the rôle of fluctuations in CDW systems.

5.4 A Generalised $M_2Mo_6Se_6$ Phase Diagram

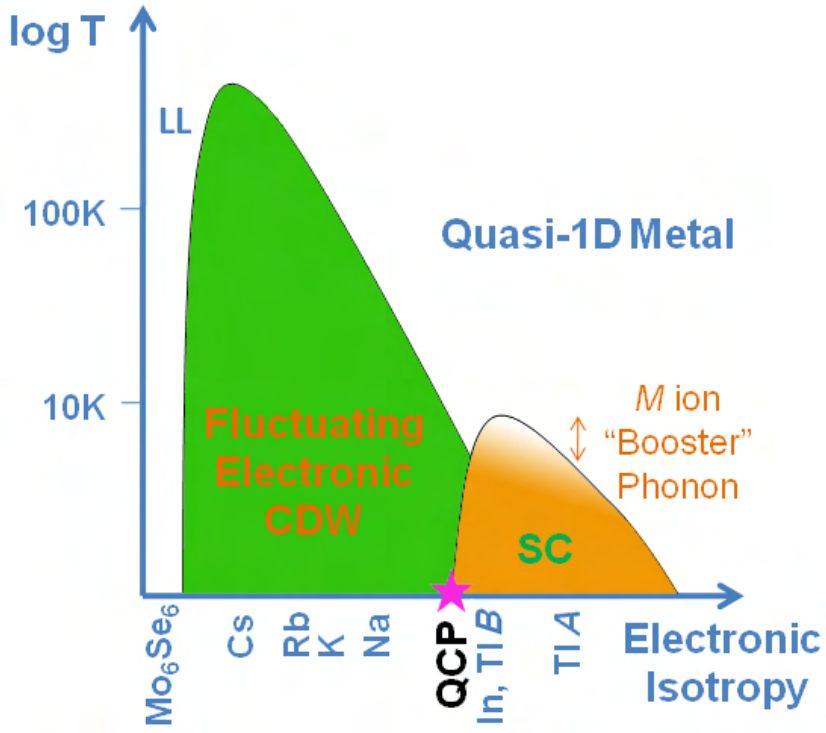

Figure 5.8: Proposed phase diagram for $M_2Mo_6Se_6$. The rather unconventional x-axis "Electronic Isotropy" variable is directly proportional to Fermi surface warping, i.e. the electronic linewidth reported in Fig. 3.8.

Assembling all our data from chapters 4 and 5, we display a combined phase diagram for the entire $M_2Mo_6Se_6$ family in Fig. 5.8. Rather

than a directly experimentally variable quantity, we have chosen the electronic isotropy as the x-axis "control parameter": this is proportional to the linewidth at E_F derived from the bandstructures discussed in section 3.3.2. By changing *M*, we may make step changes along this axis. In principle, applying hydrostatic pressure should allow the experimentalist to smoothly increase the isotropy (i.e. move to the right along the x axis), while uniaxial strain should have the opposite effect, increasing the anisotropy and moving back to the left along x.

We have included Mo_6Se_6 as the logical extreme one-dimensional limit of $M_2Mo_6Se_6$, since it has been shown to exhibit Luttinger behaviour [135]. However, the Fermi level lies lower in Mo_6Se_6 due to the reduced electron count; care must therefore be taken when comparing its physical properties with those of $M_2Mo_6Se_6$.

There appears to be a critical anisotropy lying between $Na_2Mo_6Se_6$ and B-type $Tl_2Mo_6Se_6$. This separates two distinct groundstates at T = 0: the electronic CDW for higher anisotropy and superconductivity for lower anisotropy. It is therefore a quantum critical point (QCP) and quantum fluctuations of each order parameter should be visible at higher temperature in its vicinity. The apparent coexistence of superconductivity and the MI groundstate in B-type or strained $Tl_2Mo_6Se_6$ is already suggestive of such fluctuations. Future experiments are planned in the millikelvin temperature range in order to probe this QCP more closely.

Chapter 6

Meissner State Spectroscopy and Heat Capacity Studies in the Chevrel Phases

Among the vast zoo of poorly-understood unconventional superconductors, Chevrel Phases stand out for their elevated upper critical field values H_{c2} (reaching $\sim$ 60 T in $PbMo_6S_8$), despite relatively modest transition temperatures which do not exceed $T_c \sim 15$ K. Unfortunately, the advent of the high-T_c cuprates largely swept Chevrel Phases under the laboratory carpet, despite no explanation for the large H_{c2} values having been given. The upper critical field in these materials does not follow the standard single-band Werthamer-Helfand-Hohenberg (WHH) model [136]: calculations have shown that neither strong-coupling effects nor enhanced spin-orbit scattering is able to describe $H_{c2}(T)$ [33]. A multi-band scenario was suggested as an explanation [137], but until now this hypothesis has remained unexplored.

Multi-band superconductivity was first proposed 50 years ago as a potential avenue for increasing critical temperatures [57]. Interband scattering between non-degenerate bands at the Fermi level enables superconductivity to be induced in bands which do not participate in the pairing mechanism, thus increasing the effective density of states (DoS) and hence T_c. However, with the exception of some transition metal calorimetric data [58] and a tunnelling experiment in

doped $SrTiO_3$ [59], multi-band superconductivity remained a largely theoretical concept until the discovery of MgB_2 in 2001 [138]. In this material, superconductivity in the quasi-2D σ-band induces coherence in the quasi-3D π-band with an unprecedentedly high T_c of 39 K. The two gaps have been imaged using a variety of techniques, including local spectroscopic [60] and bulk thermodynamic approaches [139]. Recently, evidence has been found for multi-band superconductivity in borocarbides [140], sesquicarbides [141], skutterudites [142] and, perhaps most interestingly, pnictides [31].

Chevrel Phases and pnictides share similar anomalously large values of H_{c2} and do not follow Werthamer-Helfand-Hohenberg theory; however the basic Mo_6X_8 (X = S, Se) Chevrel cluster does not exhibit any intrinsic magnetism (unlike most pnictides). Furthermore, recent bandstructure calculations have indicated the existence of two Mo d bands at the Fermi level E_F in $PbMo_6S_8$ [35]. With these characteristics, Chevrel Phases are ideally suited to the search for multi-band superconductivity.

In this chapter we present a detailed STS study of $SnMo_6S_8$ and $PbMo_6S_8$, together with complementary heat capacity measurements. As we will discover, these data provide solid and indisputable evidence for the existence of a two-band order parameter in Chevrel Phase superconductors.

6.1 STS in $SnMo_6S_8$ and $PbMo_6S_8$

We have chosen to principally focus on $SnMo_6S_8$ and $PbMo_6S_8$ since these two materials have the highest values for T_c and H_{c2} within the Chevrel Phase family: 14.2 K, $\sim$ 40 T and 14.9 K, $\sim$ 60 T respectively. Single crystals of each compound with typical volume 1 mm^3 were grown in Rennes at 1600 °C by a chemical flux transport method using sealed molybdenum crucibles. Their high purity was confirmed by AC susceptibility (ACS) yielding ΔT_c = 0.1 K for $SnMo_6S_8$ and 0.3 K for $PbMo_6S_8$. All STS measurements were performed in high-vacuum using the Aurora with a lock-in amplifier technique (as detailed in section 2.1.4).

6.1.1 Cleaved surface topography

Previous experiments indicated the importance of measuring cleaved rather than as-grown sample surfaces in order to probe bulk Chevrel

Phase properties [74]. This is due to a frequent *M* ion deficit (a consequence of the growth procedure) resulting in a drop in T_c close to the surface layers, with $PbMo_6S_8$ being affected more than $SnMo_6S_8$ due to the higher vapour pressure of Pb. We therefore cleave our samples in air at room temperature, before loading them directly into the STM and pumping to high vacuum. Cleaving is performed parallel to as-grown crystal mirror surfaces using a sterile scalpel. This approach relies on fortune rather than science but can occasionally produce clean mirror-plane zones of size up to 300 $\times$ 300 μm.

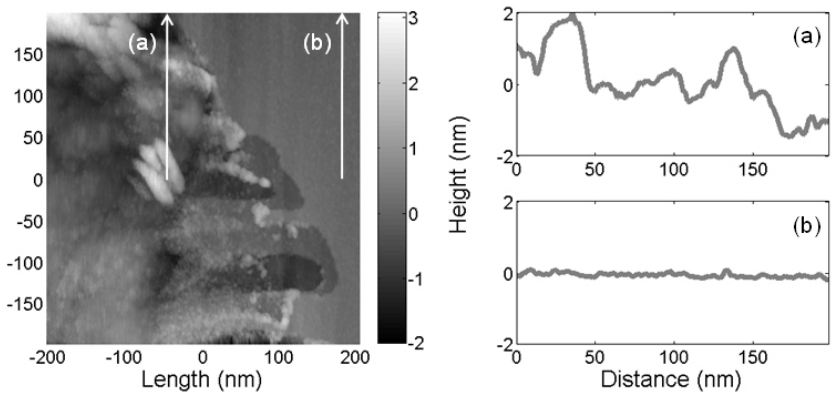

Figure 6.1: 400 $\times$ 400 nm topography on $SnMo_6S_8$ together with traces (a
from a disordered granular surface zone and (b) from an atomically flat surface.

Figure 6.1 displays a typical 400 $\times$ 400 nm topography on $SnMo_6S_8$, together with two 200 nm topographic traces. Two distinct surface styles may be seen: the left of the image has granular and disordered surface features, with no immediate correlation with the molecular structure of Sn as illustrated by trace (a). In contrast, the right of the image is comprised of wide flat terraces with less than 1 Å root mean square (RMS) topographical corrugation as shown in trace (b). Several single-unit-cell steps between terraces are also visible (see Fig. 6.3). All spectroscopic data in this work is taken on atomically flat terraces and the clean steps between them.

In principle, such a low surface noise level should enable us to obtain atomic resolution images. However, it should be noted that to obtain atomic resolution with an STM the material under study must

have a characteristic spatial modulation of the electronic LDoS. Not all materials possess such an intrinsic electronic modulation and hence the absence of atomic resolution should in no way detract from the quality of our results. Previous STM studies of Chevrel Phases also failed to resolve atoms, implying that this is a material property rather than an experimental defect.

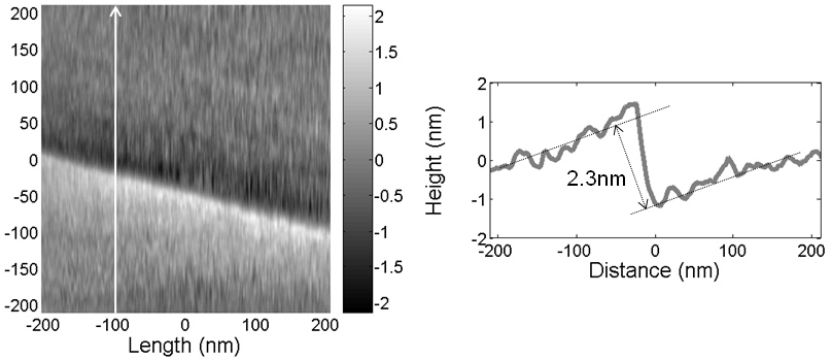

Figure 6.2: 400 $\times$ 400 nm topography on $PbMo_6S_8$ together with a trace across a large four unit cell step.

The cleaved surfaces of $PbMo_6S_8$ are typically of slightly lower quality, with an example shown in Fig. 6.2. The RMS corrugation here is $\sim$ 3 Å. This may not necessarily be due to a poor cleave: the Pb ion is more volatile than Sn (partially due to its lower vapour pressure) and can escape relatively easily from the surface. A large step-like feature runs across the map, with the 400 nm topographic trace on the right of Fig. 6.2 revealing this to be of height 2.3 $\pm$ 0.4 nm. Dividing by four, we obtain 5.75 $\pm$ 1.0 Å, which agrees well with the 5.5 Å measured lattice parameter [83]. Single unit cell steps have also been identified in $PbMo_6S_8$ (see for example Fig. 6.4), although they are generally broad and poorly-resolved compared with those seen in $SnMo_6S_8$.

It should be noted that our single crystals have not been oriented by X-ray diffraction and hence we have no means of identifying whether we are tunnelling into the (100) or (001) plane. However, due to the q3D crystal structure this should not have a significant effect, although we will return to this point while discussing the Fermi surface in section 6.2.3.

6.1.2 Sub-Kelvin spectroscopy

Having identified clean and flat areas on cleaved samples, the next step is to obtain one-dimensional spectroscopic traces across these surfaces. Figure 6.3 displays spectroscopic traces over several tens of nanometers in $SnMo_6S_8$, together with their topographic variation. $SnMo_6S_8$ features large atomically flat terraces separated by steps of size 12 ± 1Å, which compares favourably with twice the rhombohedral unit cell parameter 6.5 Å. Spectra taken on the terraces are homogeneous with a gap of 2.95 meV and a marked lack of any quasiparticle excitations within the gap, e.g. Fig. 6.3 (a)2 and (b)1, (b)3. In contrast, spectra taken on the steps between terraces display additional peaks at lower energy which are suggestive of a second gap, shown in Fig. 6.3 (a)1, (a)3 and (b)2.

Let us pause for a moment to consider this observation. As the STM tip scans along a flat surface, it consistently probes a single superconducting band with Δ_1 = 2.95 meV. These spectra are remarkably homogeneous, as can be seen from the maps in Fig. 6.3(a)(i) and (b)(i). Upon reaching a unit cell step on the surface, the STM (operating in constant-current topographic imaging mode) will raise its tip vertically as it climbs over the step. At this point, the tunnelling matrix between tip and sample changes and we briefly probe a second superconducting band with a smaller gap Δ_2.

Such spectroscopic changes upon modifying the tunnelling matrix element are not unusual: in MgB_2 the two-dimensional σ band is only visible upon tunnelling perpendicular to the c-axis. However, this is achieved by manually rotating the crystal and tunnelling "on-edge". $SnMo_6S_8$ is the first instance of a multi-band superconductor where such anisotropic behaviour has been observed on a single crystal surface.

It is natural to suggest that the isolated appearance of these multi-gap signatures at unit cell steps could be due to a surface bound state or defect. However, a localised state would not display the particle-hole symmetry of the peaks we observe. We have imaged a large number of separate unit cell steps and the opening of a second gap is consistently observed upon scanning across the step. Another possible explanation for the double-gap behaviour could be the proximity effect inducing weak superconductivity in a metallic surface layer [143]. However, the small gap induced would vary strongly with the thickness of the surface metallic layer. Not only is the deposition of such a metallic layer on our freshly-cleaved samples implausible, but it would also not be

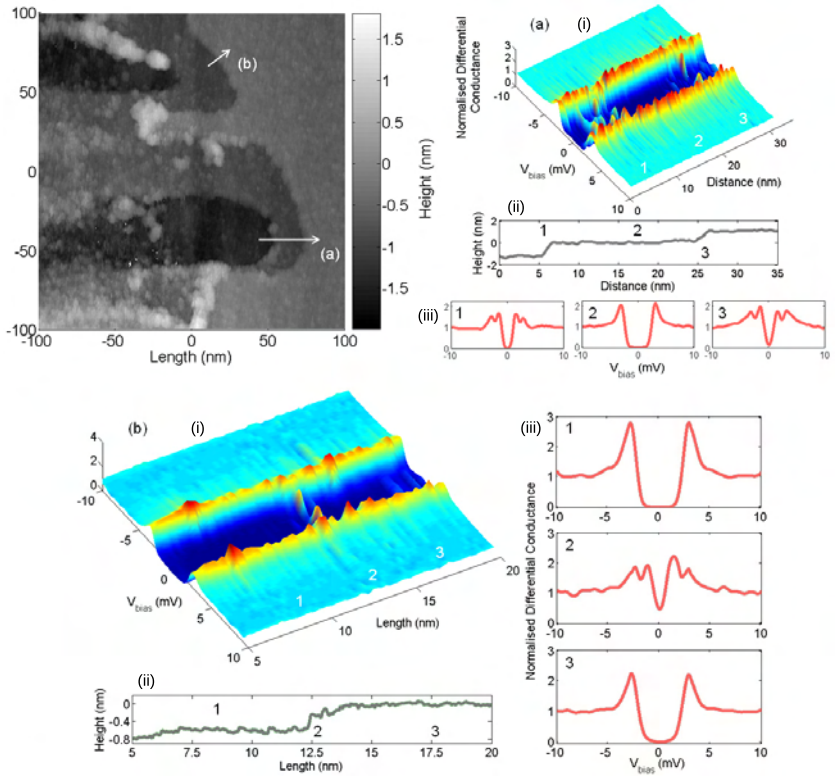

Figure 6.3: Spectral traces of length (a) 35 nm and (b) 25 nm taken across unit-cell-sized steps in $SnMo_6S_8$ (as depicted in the topographic image at top right). For (a) and (b), (i) depicts the spectra along the trace as a 3D surface map, (ii) shows the topographic variation along the trace and (iii) shows individual spectra taken at points 1, 2 and 3 along the trace.

expected to have a uniform thickness. This would cause substantial variation in the size of the induced gap and an extremely high zero-bias conductance (ZBC), which are clearly incompatible with our data.

In Fig. 6.4 we display a spectral trace across a cleaved surface of $PbMo_6S_8$ with an RMS roughness of $\sim$ 1.5 Å, featuring two broad and poorly-resolved unit-cell steps. Due to the lower surface quality and lack of clean unit-cell steps, there is no distinct spectral modulation upon crossing a step as in $SnMo_6S_8$. However, Fig. 6.4(iii) reveals nu-

merous spectra with a minor contribution from a small gap Δ_2, superposed on a larger homogeneous gap $\Delta_1 \sim 3$meV. Furthermore, the average spectrum (Fig. 6.4(iv)) displays a kink at $\sim \pm$ 1.4 meV and a V-shaped dispersion around E_F. This confirms the presence of states within the large gap, indicating an anisotropic order parameter and multi-band superconductivity.

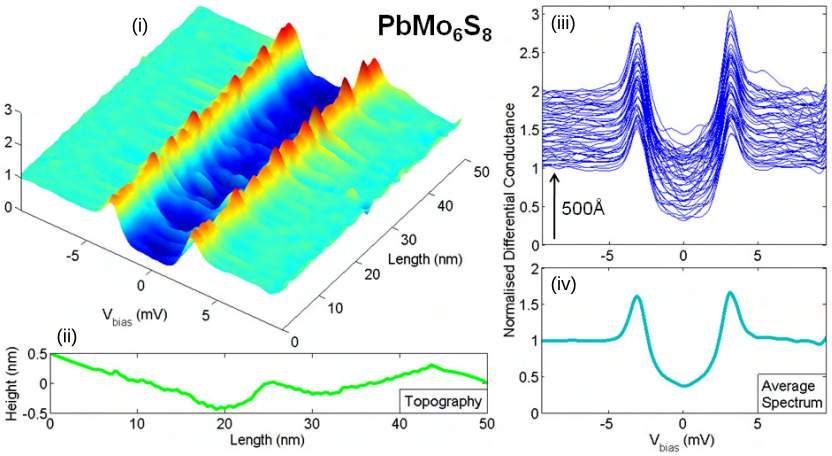

Figure 6.4: 50nm spectral trace in $PbMo_6S_8$. (i) depicts the spectra along the trace as a 3D surface map, (ii) illustrates the topographic variation along the trace, (iii) plots all the spectra with a small vertical offset and (iv) shows the average spectrum.

6.1.3 Multi-band BCS spectral fitting

Following the approach outlined in section 1.1.3, we write the generalised Bardeen-Cooper-Schrieffer (BCS) quasiparticle density of states for an anisotropic s-wave n-band superconductor as

$$N(\omega) = \sum_{j=1}^{n} \frac{N_j}{2\pi} \int_0^{\pi} \mathrm{Re}\left[\frac{(\omega + i\Gamma_j)\mathrm{sign}(\omega) d\theta}{\sqrt{(\omega + i\Gamma_j)^2 - \Delta_j^2 F_j^2(\theta)}} \right] \tag{6.1}$$

where N_j is the relative weighting of band j at E_F, Γ_j the scattering rate due to lifetime effects, Δ_j the magnitude of gap j and $F_j(\theta) = a_j + (1 - a_j)\cos\theta$ measures the anisotropy of gap j with $0.5 < a_j <$

1. We convolve this model with the derivative of the Fermi function (to account for thermal broadening) and a Gaussian of width 0.2 meV (to simulate experimental smearing from the lock-in) before performing least-squares fits to our data with N_j, Δ_j, F_j and Γ_j as free parameters. Note that the spectral backgrounds between $\pm$ 5-10 meV are rather poorly-fitted, which is indicative of strong coupling to a low-energy phonon. However, a full Eliashberg analysis of the spectra is beyond the scope of this work.

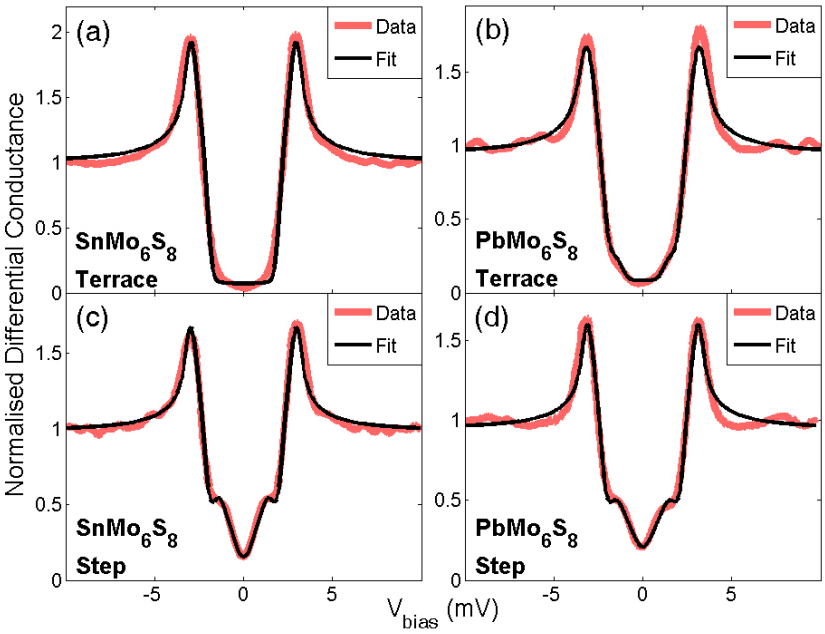

Figure 6.5: Chevrel phase tunnelling spectra and fits, taken on flat terraces ((a),(b)) and above unit-cell steps ((c),(d)). $SnMo_6S_8$ spectra were taken at 0.4 K, R_T = 0.03 GΩ; $PbMo_6S_8$ spectra were taken at 0.5 K, R_T = 0.015 GΩ. See text for details and table 6.1 for fit parameters.

In Figure 6.5 we display a range of spectra from both $SnMo_6S_8$ and $PbMo_6S_8$, together with fits using a multi-band model from equation 6.1. Atomically flat surfaces in $SnMo_6S_8$ (Fig 6.5 (a)) produce homogeneous spectra (Fig 6.5 (a)) which may be fitted using only a single gap, i.e. n=1 in equation 6.1. There is a slight deterioration in the fit quality at low energy, whch is attributed to a very small contribution

from the second band. In contrast, Fig. 6.5(c) shows averaged spectra from a 1 nm^2 zone above a unit cell step. There is clearly a significant contribution from the smaller gap, necessitating a two-band fit.

Similar fits have been carried out on spectra from a flat zone (shown in Fig. 6.5 (b)) and a broad step (Fig. 6.5 (d)) on $PbMo_6S_8$; the parameters obtained are listed in Table 6.1. Δ_1 displays a similar anisotropy in $PbMo_6S_8$ and $SnMo_6S_8$, but there is a larger relative contribution from Δ_2 in $PbMo_6S_8$. A small anisotropy in H_{c2} (ϵ^2 = 0.67) has been observed in $PbMo_6S_8$ [137], but with the present data we are unable to judge whether this is due to the small anisotropy in Δ_1 or the larger anisotropy in Δ_2.

We believe it unwise to draw quantitative conclusions on the degree of anisotropy in Δ_2, since our experiment has a finite resolution imposed by a 0.2 meV broadening from the lock-in. Furthermore, for small gap values Γ_j and F_j have a similar smearing effect and one parameter may therefore compensate another during the fitting procedure. However, our results discourage a d-wave or more exotic order parameter for the smaller gap, since it should not be possible to mix pairing symmetries for non-zero interband scattering.

Table 6.1: Superconducting gap parameters and relative DoS contributions from fits to STS and heat capacity data. Both gaps $\Delta_{1,2}$ are measured in meV.

	$SnMo_6S_8$		**$PbMo_6S_8$**	
	Terrace	Step	Terrace	Step
T_c (ACS)	14.2 ± 0.05 K		14.9 ± 0.15 K	
H_{c2} (HC)	∼ 40 T		∼ 70 T	
H_{c2} ($\gamma(H)$)	∼ 43 ± 1 T		∼ 86 ± 5 T	
Δ_1 (STS)	2.92 ± 0.1	2.95 ± 0.1	3.14 ± 0.1	3.06 ± 0.1
Δ_2 (STS)	–	1.05 ± 0.2	1.42 ± 0.2	1.38 ± 0.2
a_1 (STS)	0.85 ± 0.02	0.87 ± 0.02	0.85 ± 0.02	0.89 ± 0.02
a_2 (STS)	–	0.91 ± 0.05	0.92 ± 0.05	0.61 ± 0.05
N_1 (STS)	–	62 ± 4%	90 ± 4%	66 ± 4%
N_2 (STS)	–	38 ± 4%	10 ± 4%	34 ± 4%
Δ_1 (HC)	3.06 ± 0.1		3.15 ± 0.1	
Δ_2 (HC)	0.86 ± 0.1		1.41 ± 0.1	
N_1 (HC)	96 ± 2%		90 ± 2%	
N_2 (HC)	4 ± 2%		10 ± 2%	
γ (HC)	6.4 ± 0.1 mJgat^{-1}K^{-2}		6.7 ± 0.1 mJgat^{-1}K^{-2}	

Previous STS experiments on $PbMo_6S_8$ also provided evidence for

low-energy excitations within the superconducting gap, but lacked sufficient resolution to distinguish two separate gaps. This is due to two factors: measurement temperature and sample environment. In ref. [35], measurements were performed at 1.9K in an exchange gas, compared with 0.4-0.5 K and high vacuum in the present work. The increased thermal broadening at 1.9 K blurs the two gaps, though this should not be sufficient to render the smaller gap invisible. The major factor here is a deterioration in the sample surface due to the exchange gas environment.

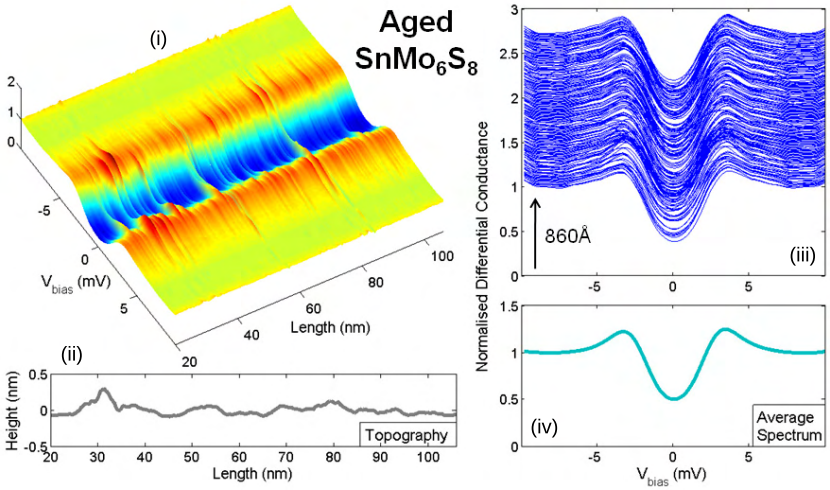

Figure 6.6: 86 nm spectral trace in aged $SnMo_6S_8$ (after 3 months in STM chamber). (i) depicts the spectra along the trace as a 3D surface map, (ii) illustrates the topographic variation along the trace, (iii) plots all the spectra with a small vertical offset and (iv) shows the average spectrum.

It is well-known that in a two-band superconductor, interband scattering due to impurities mixes the two gaps and reduces T_c, resulting in an effective single-band anisotropic superconductor in the dirty limit. This was first predicted for MgB_2 [144, 145] and later observed in irradiated samples [61]. However, due to extremely weak scattering between σ and π bands, the single band limit is never reached in MgB_2.

This is not the case for Chevrel phases: Fig. 6.6 displays extremely homogeneous spectra from a $SnMo_6S_8$ terrace after three months of measurements comprising numerous thermo-magnetic cycles. These

are qualitatively similar to the results of Dubois *et al.* (shown in fig. 3.5), providing good evidence for low-energy states within the large gap, but do not display a distinct smaller gap. The ZBC is also rather high in both Fig. 6.6 and the Dubois results, which we attribute to a Dynes effect caused by inelastic tunnelling into a poor surface. The apparent "mixing" of large and small gaps is indicative of significant inter-band scattering in Chevrel phases. This is an important difference compared to MgB_2. Furthermore, since the band mixing effectively induces an anisotropy in both gaps, we have an additional reason to question the validity of our fitted anisotropy values.

6.1.4 Spectroscopic temperature scans

Figure 6.7 (a) and (b) display the spectra obtained in $SnMo_6S_8$ and $PbMo_6S_8$ upon increasing the experimental temperature. The large gap Δ_1 is gradually reduced and closes at the bulk T_c determined by ACS. No pseudogap is visible above T_c, confirming that superconductivity arises from a metallic ground state and hence justifying the use of a BCS model to fit the spectra. In Fig. 6.7 (c) and (d), we have plotted the variation of Δ_1 with temperature for each compound, together with the theoretical BCS weak-coupling s-wave curve for comparison. A small kink is visible within each curve (brown shaded areas).

Similar features have been observed for the π-band (smaller) superconducting gap in MgB_2 [146] and originate from inter-band scattering "stretching" the effective T_c of the weakly-coupled π band to the bulk T_c. It is unclear why such an effect should also be visible in the $\Delta_1(T)$ curve of the larger gap in a two-band superconductor: we postulate that in Chevrel phases a small contribution from a weakly-coupled band "stretches" the intrinsic T_c of a strongly-coupled band (which provides the majority of the DoS) to the measured bulk T_c. The position of the kink at higher energy and lower temperature in $PbMo_6S_8$ compared with $SnMo_6S_8$ is consistent with our observation that band 2 is more strongly-coupled and has a larger relative DoS contribution in $PbMo_6S_8$. We hypothesise that this may play some rôle in $PbMo_6S_8$ having a significantly higher H_{c2} than $SnMo_6S_8$, although further experiments will be required for confirmation.

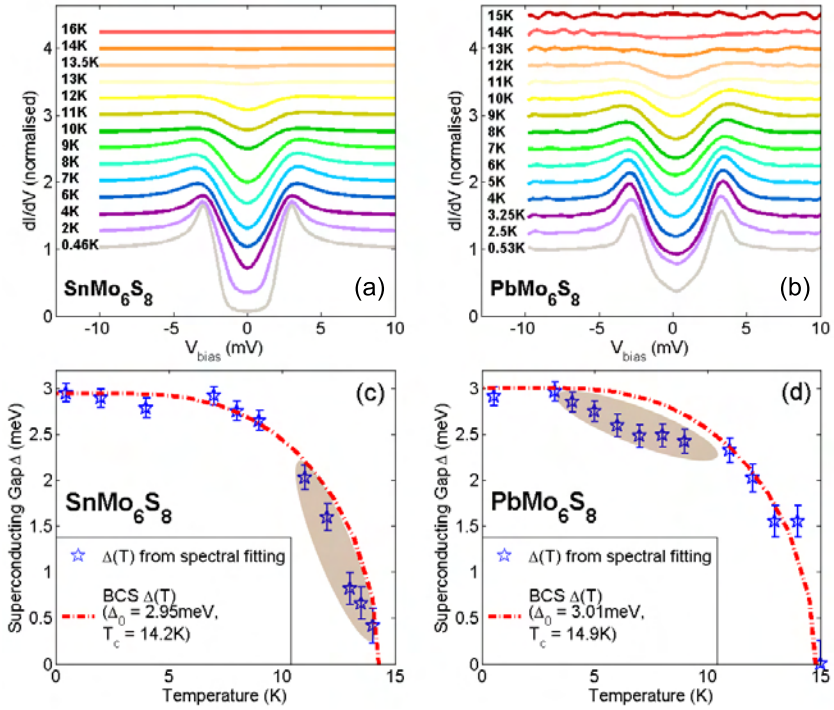

Figure 6.7: Variation of the large gap $\Delta_1(T)$ in (a) $SnMo_6S_8$ and (b) $PbMo_6S_8$. The gap was determined by fitting spectra with a BCS single-band anisotropic s-wave model for simplicity.

6.2 Specific Heat of $SnMo_6S_8$, $PbMo_6S_8$ and $LaMo_6S_8$

It is instructive to complement our STS measurements with bulk thermodynamic (HC) data, in order to conclusively rule out any spurious surface effects being responsible for Δ_2. Heat capacity measurements were therefore performed both at the Grenoble High Magnetic Field Laboratory with a high-resolution microcalorimeter (see section 2.2) using the "long relaxation" technique [147] and in Geneva using a Quantum Design^{TM} PPMS.

6.2.1 Electronic heat capacity from high-field data

In Fig. 6.8 we plot the total heat capacity $\frac{C(T)}{T}$ for a range of fields measured in Grenoble. As discussed in section 3.1.3, in Chevrel phases there is a large contribution to the lattice specific heat C_{latt} from a low-energy Einstein phonon due to vibrations of the cation between the Mo_6X_8 clusters: it is therefore not possible to calculate C_{latt} and hence extract C_{elec} using the conventional model detailed in equation 1.10. The large lattice contribution persisting to low temperatures is immediately obvious in Fig. 6.8 due to the strong negative curvature and the small jump at T_c relative to the absolute value of $\frac{C(T)}{T}$, especially in $PbMo_6S_8$ and $SnMo_6S_8$. We therefore calculate the electronic heat capacity by subtracting the normal-state data from our zero-field heat capacity. To eliminate the effect of fluctuations above T_c in high field, we limit our data to $T > 1.15\ T_c$(28T), where T_c(28T) = 4.4 K and 9.3 K in $SnMo_6S_8$ and $PbMo_6S_8$ respectively.

Figure 6.9 displays the electronic heat capacity C_{elec} in $PbMo_6S_8$, $SnMo_6S_8$ and $LaMo_6S_8$, together with fits using a two-band α-model [64]. Our results for $PbMo_6S_8$ and $SnMo_6S_8$ are summarised in Table 6.1: for both gaps, the values of $2\Delta/k_BT_c$ from our STS data agree perfectly with those from heat capacity experiments. While it is not possible to quantitatively compare N_j as measured by STS (which also depends on the tunnelling matrix element) with the bulk N_j, the trends observed by each technique ($N_1 > N_2$, N_2/N_1 greater in $PbMo_6S_8$ than $SnMo_6S_8$) are qualitatively in agreement.

Despite not being able to reveal the normal-state electronic heat capacity in $PbMo_6S_8$ and $SnMo_6S_8$ as $T \to 0$, we may still calculate the Sommerfeld constant γ using entropy considerations, as indicated in section 1.2.2. γ/T_c = 0.45 mJgat^{-1}K^{-3} for M = Pb, Sn compared with 0.42 mJgat^{-1}K^{-3} in $LaMo_6S_8$, suggesting that T_c scales with the DoS at E_F in the Chevrel phases (as originally predicted in the 1970s [148]).

We are also able to determine H_{c2} from Fig. 6.8. Identifying $T_{c2}(H)$ as the midpoint of each superconducting transition, we plot $H_{c2}(T)$ in Fig. 6.10. Simple linear extrapolations suggest that H_{c2} in $SnMo_6S_8$ and $PbMo_6S_8$ should approach 41 T and 75 T respectively. While single-band WHH theory states that $T_{c2}(H)$ should saturate at low temperature leading to a lower value of H_{c2} [136], two-band superconductivity is predicted to limit this saturation and hence H_{c2} should lie closer to the linearly extrapolated values [149]. Such high upper critical fields could be partially explained by a significant impurity content; however the narrow superconducting transitions measured by ACS indicate that

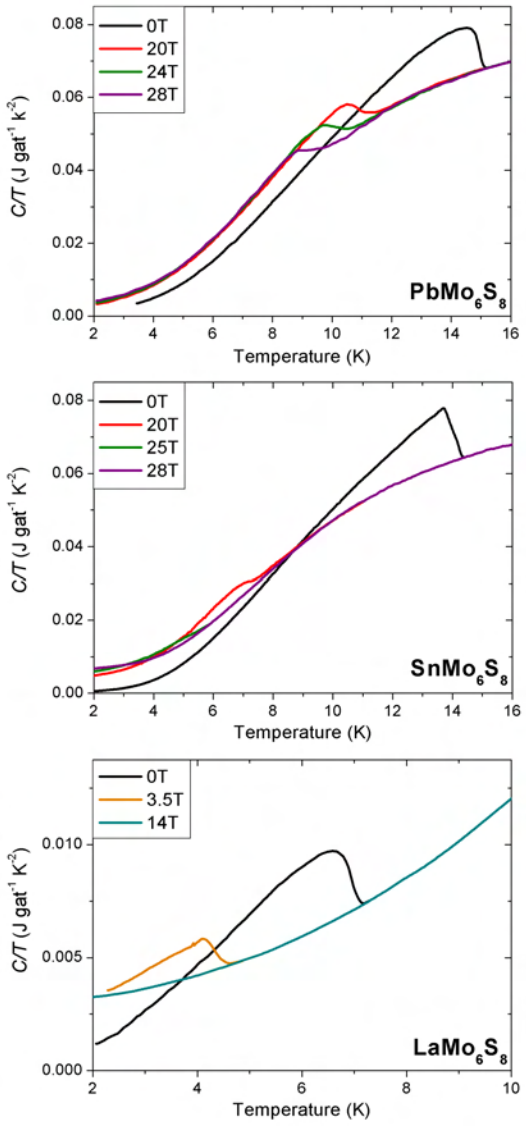

Figure 6.8: Total specific heat C/T in $PbMo_6S_8$, $SnMo_6S_8$ and $LaMo_6S_8$ in a range of fields from 0 - 28 T.

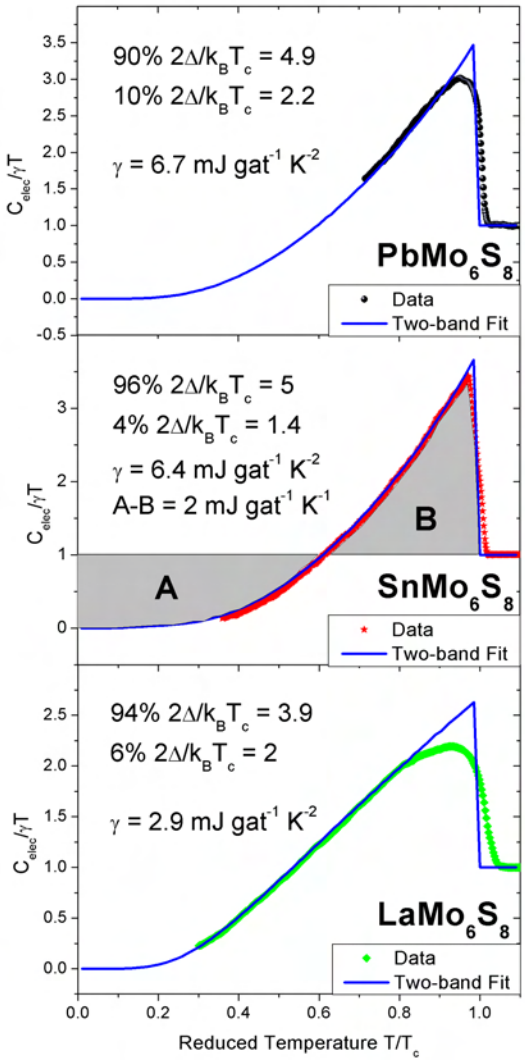

Figure 6.9: Electronic specific heat $C/\gamma T$ in $PbMo_6S_8$, $SnMo_6S_8$ and $LaMo_6S_8$ as a function of reduced temperature T/T_c. Two-band fits using the α model are shown in blue.

our samples are clean and H_{c2} is intrinsic.

In $LaMo_6S_8$, the coupling strength of the large gap is noticeably

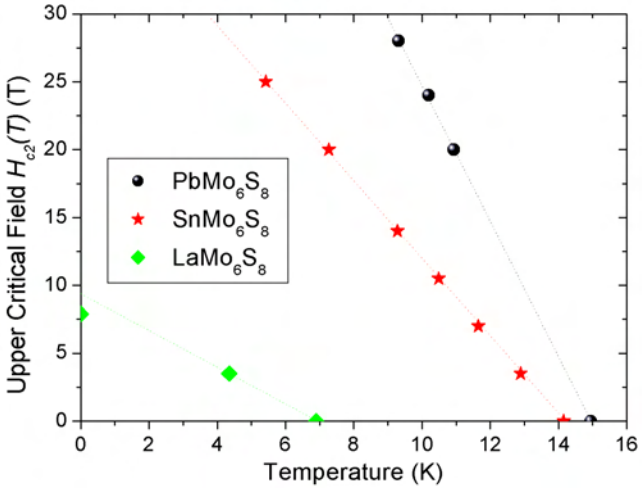

Figure 6.10: Variation of the upper critical field $H_{c2}(T)$ with temperature for $PbMo_6S_8$, $SnMo_6S_8$ and $LaMo_6S_8$. $SnMo_6S_8$ data from 3.5 - 14 T was measured in Geneva with a similar microcalorimeter; see section 7.3 for further details.

weaker than in $PbMo_6S_8$ and $SnMo_6S_8$. While the variation in T_c in the Chevrel phases seems to be explained by the DoS at E_F alone, the coupling strength has some impact on H_{c2}. Stronger electron-phonon coupling allows for smaller Cooper pairs, leading to a shorter coherence length and a larger H_{c2}. Variations in coupling strength may hence partially account for the difference in H_{c2} among the Chevrel phases. However, this is clearly not the sole contributory factor: H_{c2} in $PbMo_6S_8$ is over 50% larger than that of $SnMo_6S_8$, despite both materials having a similar coupling strength for Δ_1. The multi-band order parameter must therefore have a more subtle effect on H_{c2}.

6.2.2 Field-variation of the Sommerfeld constant

The final piece of compelling evidence for two-band superconductivity in the Chevrel phases is provided by the low-temperature variation of $C_{elec}(H)$. This is measured using the PPMS at 400 mK. As discussed in section 1.2.3, $\gamma(H)$ should be linear in a single-band BCS s-wave superconductor. In Fig. 6.11 we plot $\gamma(H)$ measured at 400 mK in both $SnMo_6S_8$ and $PbMo_6S_8$, with the magnetic field applied parallel to the

(100)/(001) mirror planes.

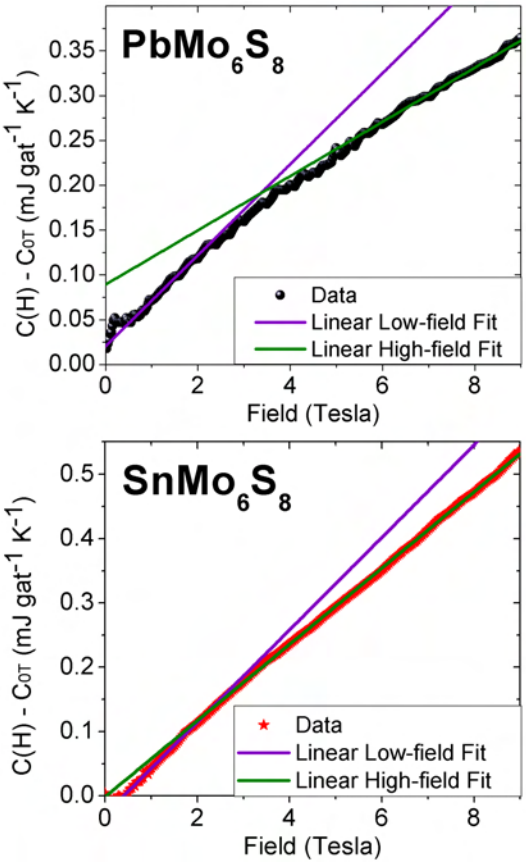

Figure 6.11: Chevrel phase electronic specific heat $\gamma(H) \equiv C(H) - C_{0T}$. Linear fits to the high-field data (above 7.5 T) and low-field data (below 1.5 T) are included as guides to the eye. Data taken below H = 0.5 T are susceptible to magnetoresistive fluctuations of the calorimeter and are hence unreliable; any offsets in this field range should be disregarded. Noise in the $PbMo_6S_8$ data is representative of the resolution limits of the calorimeter and is visible due to the $PbMo_6S_8$ crystal weighing less than the $SnMo_6S_8$ crystal by a factor of ~ 5.

Neither $PbMo_6S_8$ nor $SnMo_6S_8$ exhibit purely linear behaviour. In $SnMo_6S_8$, we observe a bend in $C_{elec}(H)$ at 2.8 T (T = 0.35 K), reminis-

cent of that observed at low field in MgB_2. The data then reverts to a linear relation at higher fields. Extrapolating the linear high-field data to $\gamma(H) = \gamma$ = 6.4 mJgat^{-1}K^{-2}, we obtain H_{c2} = 43 $\pm$ 1 T. For $PbMo_6S_8$, a larger bend may be seen to occur over a broader field range, roughly centred at 3.4 T but $\gamma(H)$ remains curved up to at least 6 T. By linearly extrapolating the high-field data to γ = 6.7 mJgat^{-1}K^{-2}, we estimate H_{c2} = 86 $\pm$ 5 T.

Let us consider the physical significance of this bend in $\gamma(H)$. In the zero-interband-scattering limit, as the applied field in a two-band superconductor is increased vortices will primarily occupy the more weakly-coupled band (with gap Δ_2) since its H_{c2} is lower. Once superconductivity has been destroyed in this band, vortices will start to populate the strongly-coupled band (with gap Δ_1). This crossover should lead to a distinct change in gradient in $\gamma(H)$. The ratio of the field at which this crossover occurs to H_{c2} yields the relative contributions to the DoS at E_F of each band.

There appears to be significant inter-band scattering in the Chevrel phases, which means that we cannot consider a vortex to purely occupy a single band. This leads to a blurring of the crossover in $\gamma(H)$; however, the low and high-field trends in $\gamma(H)$ remain representative of band 2 and band 1 respectively. Comparing this model to our data, we estimate N_1=93 $\pm$ 2%, N_2=7 $\pm$ 2% for $SnMo_6S_8$ and N_1=92 $\pm$ 4%, N_2=8 $\pm$ 4% for $PbMo_6S_8$. These figures are in good agreement with those in Table 6.1. We may also identify effective upper critical fields for the weakly-coupled bands: H_{c2}^{eff} = 36 $\pm$ 1 T for $SnMo_6S_8$ and 52 $\pm$ 4 T for $PbMo_6S_8$.

6.2.3 Effects of anisotropic Fermi surfaces

It is instructive to consider our results in light of the calculated Chevrel phase Fermi surfaces detailed in section 3.1.2. Firstly, the calculated two-band DoS at E_F is qualitatively in agreement with our spectroscopic and heat capacity measurements on $PbMo_6S_8$, $SnMo_6S_8$ and $LaMo_6S_8$ since two-band order parameters provide superior fits to single-band models in all our data. While our BCS fitting procedure models the Fermi surface as a sphere, it is clear that the true Fermi surface has a much more complex topology. In particular, there is no Fermi surface for the minority band in $PbMo_6S_8$ and $SnMo_6S_8$ over a significant fraction of k-space (see Fig. 3.3).

The absence of a Fermi surface for a given wave-vector implies that the tunnelling matrix element is zero in this direction. This explains

why the small gap is not seen in $SnMo_6S_8$ whilst tunnelling into (100) or (001) planes. Naively, from the calculated Fermi surface one would expect a maximal contribution from this gap when tunnelling parallel to (111).

However, it is unclear why our measured partial DoS do not agree with calculations. From our heat capacity data, we estimate a maximal contribution from the minority band of $\sim$ 10% of the DoS at E_F, compared with a calculated contribution of just under 40% in $PbMo_6S_8$ and $SnMo_6S_8$. Confusingly, our fits to the heat capacity of $LaMo_6S_8$ provide an excellent agreement with theory, reproducing the calculated partial DoS to within 1%. We do not see strong evidence in STM for a significant contribution from the minority band in either $PbMo_6S_8$ or $SnMo_6S_8$ (except for several isolated spectra directly above unit-cell steps), although this could be due to a vanishing tunnelling matrix element.

It is not immediately apparent how to resolve this mysterious discrepancy between theory and experiment. For now, we postulate that it is a consequence of strong inter-band scattering in $PbMo_6S_8$ and $SnMo_6S_8$; this concept will be explored further in chapter 8.

Chapter 7

Vortex Glass Imaging in Chevrel Phases and the Magnetic Phase Diagram of $SnMo_6S_8$

Twenty years after the first attempt to produce a generalised vortex phase diagram for type-II superconductors, there is still no general consensus on this subject. In particular, confusion remains over the nature and topology of the "vortex glass" phase [150, 151, 152] and its relation to the peak effect observed in DC magnetisation and AC susceptibility of numerous type-II systems. It has been claimed that the peak effect in low-T_c materials is associated with the transition from a Bragg glass to a vortex glass [153]. Other peak effect interpretations include the elastic lattice softening model [154] and a multi-dynamic vortex liquid scenario [155]. However, recent studies of Nb_3Sn do not give any indication of a phase transition from a Bragg glass to an intermediate disordered state within the peak regime: instead, the peak effect is interpreted as arising from the metastability of an underlying first-order vortex melting transition [156, 157]. It may therefore be considered as a zone dominated by strong thermal fluctuations and consequentially enhanced pinning.

Extended real-space vortex imaging is the best method of clarifying the extent of disorder in the (H,T) phase diagram. However, it remains a considerable challenge, with the inherent difficulties varying with the

choice of superconductor. In low-T_c materials the disordered vortex phase typically spans a narrow window of phase space, thus limiting experimental accessibility [156]. Images of the disordered phase have only been obtained in $NbSe_2$, where magnetic decoration reveals static disorder [158] and scanning tunnelling microscopy (STM) in the peak effect regime displays a crossover from collective vortex motion to positional fluctuations [159]. In contrast, disorder occupies a far greater portion of phase space in high-T_cs due to their small coherence volumes and hence increased influence of thermal fluctuations. Unfortunately high vortex mobility severely complicates the detection of any stable high-field vortex solid in these compounds [40].

The Chevrel phase $SnMo_6S_8$ is an attractive system to investigate since its extremely short coherence length $\xi \sim 3$ nm lies close to those of the high-T_cs, suggesting that disordered zones of its phase diagram may be more extensive and easily experimentally accessible. An additional advantage is its quasi-3D crystal structure which should help to stabilise any disordered solid phase against melting at non-zero temperature [150]. In this chapter, we explore the magnetic phase diagram of $SnMo_6S_8$, primarily by STS but also employing magnetic and thermodynamic techniques in order to interpret our spectroscopic discoveries. As we will discover, our STM data displays a crossover from a quasi-ordered vortex lattice (presumably the Bragg glass) to a disordered vortex glass. At 400 mK, this takes place between 2 T and 5 T. In contrast, the peak effect is found at much higher fields and temperatures in $SnMo_6S_8$. This implies that the peak effect phenomenon and vortex glass formation are not linked, as was previously widely believed.

7.1 Real-space Vortex Imaging by STS

Single crystals of $SnMo_6S_8$ (typical size 3.5 mm^3) were grown in sealed molybdenum crucibles at 1550 °C. Their high purity was verified by X-ray diffraction and AC susceptibility measurements, yielding T_c = 14.2 K with an unprecedentedly low transition width of 0.1 K. The sample preparation and characterisation was identical to that carried out for the experiments in chapter 6.

7.1.1 A vortex-hunter's recipe for lattice stabilisation

The low-temperature vortex structure (VS) was imaged on cleaved sample surfaces in our STM, operating in spectroscopic mode at 400 mK.

Previous experiments [74] have shown that obtaining a stable vortex lattice in $PbMo_6S_8$ is virtually impossible if the sample is zero-field cooled and the magnetic field applied once at base temperature. This is due to the surface barrier potential blocking vortex penetration. Instead, the samples must be field-cooled: we apply the magnetic field at 18 K, then cool to 1.8 K at roughly 14 K/hour. The sample is held at 1.8 K for 12 hours (during which time helium-3 can be condensed), then cooled to 400 mK and held for a further 36 hours prior to measurement. In the absence of any dedicated vortex shaking mechanism, this stabilisation procedure allows the VS to relax towards its low-temperature equilibrium state. No field gradients are present in our STM and we do not observe any vortex drift in our data.

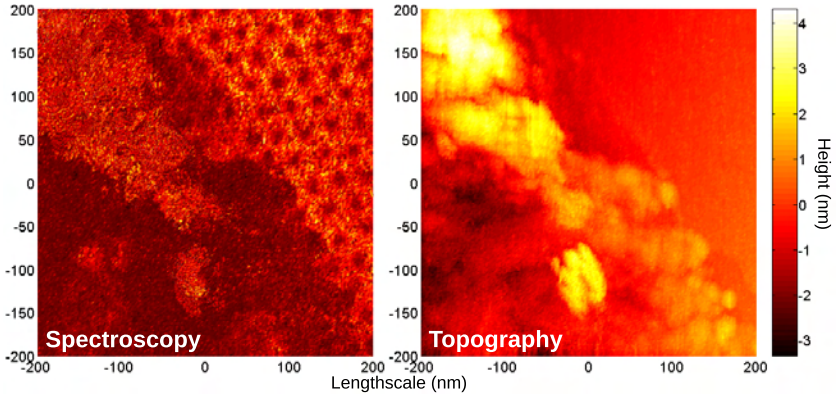

Figure 7.1: Vortex imaging in $SnMo_6S_8$ at 410 mK, H = 2 T. Left: 400 $\times$ 400 nm spectroscopic contrast σ_{pk}/σ_{ZBC} map, no colour-scale. Right: simultaneously acquired topographic map over the same area (height variation shown by colour bar). A vortex lattice is only observed on atomically flat regions of the surface.

Following the discussion in section 1.1.4, the vortex core may primarily be distinguished from the surrounding superconducting matrix by its higher zero-bias conductance. However, as we will discover in chapter 8 the vortex cores in $SnMo_6S_8$ exhibit an anomalous pseudogap. For the best resolution, it is therefore critical to image vortices as local minima in σ_{pk}/σ_{ZBC} conductance-contrast maps, with σ_{pk} the conductance at the Meissner state coherence peak energy (3 meV) and σ_{ZBC} the zero-bias conductance [40]. Optimal spectroscopic conditions for high-speed mapping are generally obtained at low-current

tunnelling conditions V_b = 15 mV, I_t = 0.25 nA, i.e. junction resistance R_t = 60 MΩ.

Figure 7.1 displays an early large-scale 400 $\times$ 400 nm vortex map, together with its surface topography. We immediately notice that vortices may only be distinguished on atomically flat areas of the surface: although traces of superconductivity remain in individual spectra from topographically disordered regions, no trace of a vortex lattice can be seen. It remains to be clarified whether this is due to the disorder creating a barrier effect and blocking field penetration, or an insufficient superconducting volume fraction in these areas inhibiting vortex formation. Atomically flat surfaces are therefore crucial to successful vortex imaging.

In contrast with previous reports on STM vortex imaging typically showing a few dozen vortices [40, 160], our images contain significantly more vortices ($\sim$ 100). This allows us to accurately study the field-evolution of the VS in $SnMo_6S_8$. Due to the substantial amount of time required for comprehensive measurements at a single magnetic field, coupled to the fact that the sample surfaces degrade over time as illustrated in section 6.1.2, we only present measurements at three magnetic fields: 2 T, 5 T and 9 T. Highly-disordered vortex lattices have also been imaged at 11 T; however the noise level is higher due to vibrations from the lambda-plate refrigerator necessary to cool the main bath to below 2.2 K for operation above 9T. Since these data do not make any additional contribution to our conclusions, we will not discuss them further here.

7.1.2 Correlation functions and Delaunay analysis

Figure 7.2 shows the vortex positions (blue spots) for applied fields of 2, 5 and 9T on an atomically flat surface. The topological properties of the $SnMo_6S_8$ VS change remarkably with field: the 2T VS is almost perfectly hexagonal whereas the 5 and 9T VS are much more disordered. This is evident from analysing the Delaunay triangulation [161] of the structures, a construction allowing the identification of nearest-neighbors and hence topological defects (non-six-fold coordinated vortices). The 2T VS lacks defects whereas the high-field VS (5 and 9T) present numerous dislocations (pairs of five and seven-fold coordinated vortices highlighted with orange triangles), their density increasing with field.

A more quantitative description of the topology of the VS is provided by the orientational and positional correlation functions [161,

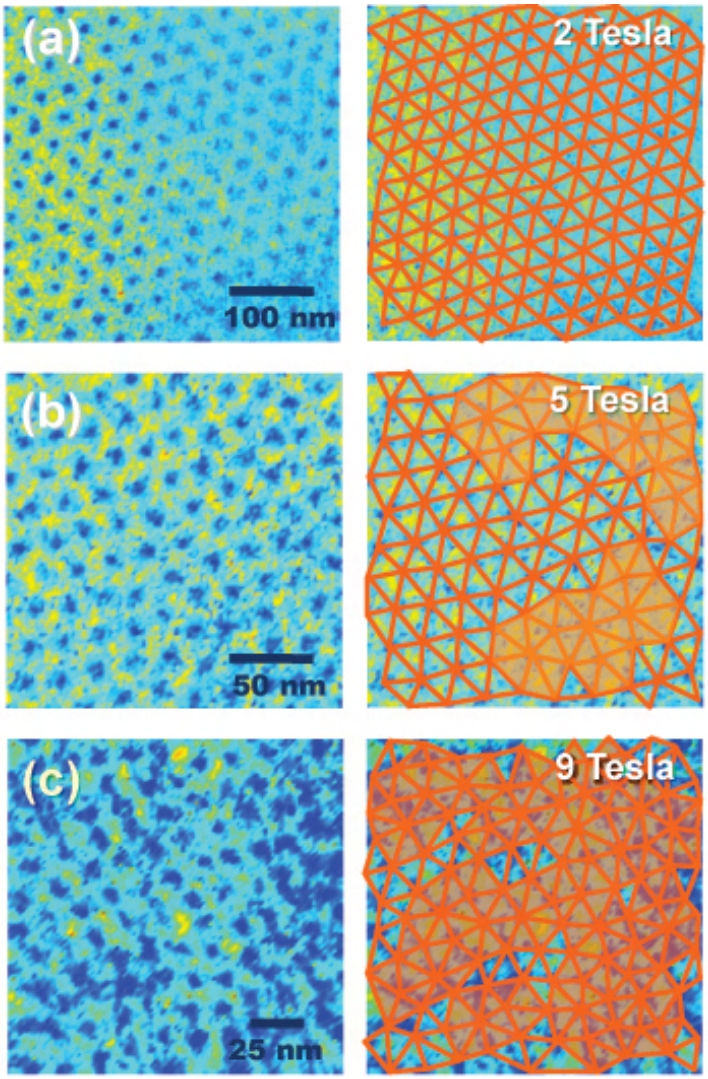

Figure 7.2: Vortex structure in $SnMo_6S_8$ at 400 mK imaged by STM at (a) 2, (b) 5 and (c) 9 T. Right panels: corresponding Delaunay triangulations with nearest-neighbors linked by orange lines and topological defects highlighted with orange triangles.

162]. Figure 7.3(a) shows the orientational correlation function $G_6(r) = <\Psi_6(0)\Psi_6^{\star}(r)>$ measuring the spatial evolution of the orientational order parameter $\Psi_6(r) = (1/n)\Sigma_{j=1}^{n} \exp 6i\theta_j(r)$ [162], a quantification of the angular misalignment of vortices with respect to the principal directions of a perfect triangular lattice. Within the field of view the 2 T VS presents quasi-long-range orientational order, whereas in higher fields the orientational order is short-ranged: for large r/a, $G_6(r)$ at 5 T is roughly 5 times smaller than that at 2 T and $G_6(r)$ at 9 T lies close to zero (for perfect orientational order $G_6(r) = 1$). The lower degree of orientational order in the high-field VS is mainly associated with the proliferation of dislocations.

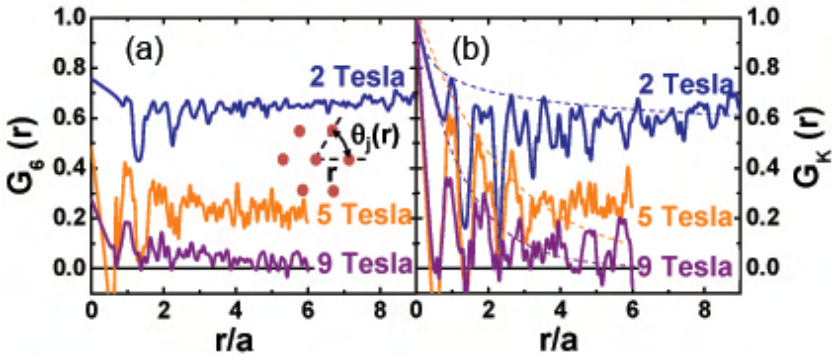

Figure 7.3: (a) Orientational correlation functions of the structures and a schematic of the angles considered for the calculation. (b) Positional correlation functions and fits of the envelope using power-law (blue-dashed line, 2 T) and exponential (orange and purple-dashed lines, 5 and 9 T) decays. The maps were acquired with a 60 MΩ junction using a lock-in technique [40].

Figure 7.3(b) shows the spatial evolution of $G_K(r)$, the average of the positional correlation functions $G_{\mathbf{k_i}}(\mathbf{r})$ evaluated in the three principal directions of the vortex structure ($\mathbf{k_i}$ are obtained from the peak positions in the VS Fourier transform). Each $G_{\mathbf{k_i}}(\mathbf{r}) = <\Psi_{\mathbf{k_i}}(0)\Psi_{\mathbf{k_i}}{}^{\star}(\mathbf{r})>$, where the positional order parameter $\Psi_{\mathbf{k_i}}(\mathbf{r}) = \exp i\mathbf{k_i} \cdot \mathbf{r}$, measures the spatial evolution of the vortex displacements with reference to the sites of a perfect hexagonal lattice [161, 162]. In the 2 T VS the envelope of $G_K(r)$ exhibits a power-law decay, a dependence consistent with the quasi-long-range positional order characteristic of Bragg glasses [163, 164]. However, for the high-field VS the envelope of $G_K(r)$ is

better described by an exponential decay, indicative of short-range positional order. The positional order deteriorates with increasing field: for the 9 T VS $G_K(r)$ decays faster and tends to a value close to zero at large r/a.

The considerable number of dislocations present in the high-field VS at temperatures as low as 400 mK contrasts strongly with the defect-free 2 T VS, indicating that the 5 and 9 T VS depict a vortex glass [150] whilst the 2 T image most probably represents a Bragg glass [163, 164]. In order to confirm the latter, shaking experiments should be performed: this is not possible with our current experimental setup although should be difficult to implement in the future by adding a small coil beneath the sample holder. Since the vortex interaction energy grows in increasing magnetic field, the observation of a less ordered 5 T VS suggests that a disorder-induced topological transition takes place in $SnMo_6S_8$ between 2 and 5 T.

7.2 SQUID and Vibrating Sample Magnetometer studies

Magnetic loops $M(H)$ at constant temperature provide an easy and reliable way of identifying the region of the $H-T$ phase diagram in which the peak effect may be found. A hysteretic (i.e. irreversible) region of $M(H)$ corresponds to a non-zero critical current J_c and hence pinned vortices: any increase in the hysteresis therefore indicates an increase in the critical current and pinning strength. The peak effect generally manifests itself as a small hysteretic "bubble" within the reversible region of a magnetisation loop.

In order to locate the peak effect, we primarily obtain such loops using a Lakeshore Model 7300 vibrating sample magnetometer (VSM) due to its larger maximum field (9 T) and high speed of measurement. However, we turn to a Quantum Design SQUID magnetometer for high-sensitivity low-field measurements at temperatures just below T_c. While performing these experiments, we are also able to extract the variation of J_c with applied field since within the Bean model [165] J_c is proportional to the separation of the up and downward sweeps in a closed $M(H)$ loop. This provides us with valuable information concerning the nature of the vortex pinning.

7.2.1 From the individual pinning limit...

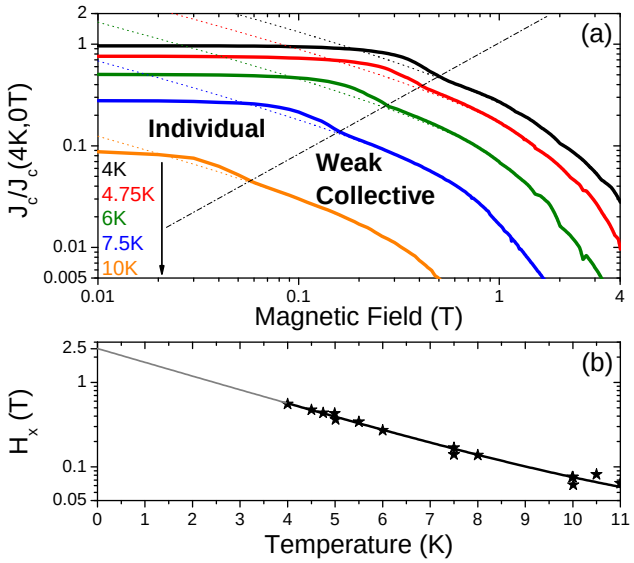

Figure 7.4: (a) Critical current versus field in $SnMo_6S_8$ (solid lines) obtained from magnetisation loops at different temperatures. The crossover from individual to collective vortex pinning is identified as a kink in the curves. Dashed lines: visual guides extrapolating the high-field $J_c(H)$. (b) Pinning crossover field $H_x(T)$. An exponential decay $ae^{-bT} + c$ extrapolates the fit to $T = 0$.

It is instructive to examine the nature of vortex pinning within the phase space probed by STM, since in certain high-T_c cuprates the low-temperature vortex order-disorder transition accompanies a crossover from individual to collective pinning [166]. In Fig. 7.4(a) we plot the evolution of the critical current density $J_c(H, T)$ (estimated from SQUID magnetisation loops). Two zones are immediately visible: a low-field region where J_c remains roughly constant (characteristic of individual vortex pinning [167]) and a high-field region in which J_c decreases with increasing field. A distinct kink separates the two regions and we identify this as the crossover field H_x between individual and weak collective pinning.

Although we are not able to measure our sample magnetisation at 400 mK, $H_x(T)$ is well-fitted by a simple exponential decay (Fig. 7.4(b)).

Extrapolating this fit, we estimate $H_x \sim 2.2 \pm 0.30$ T at 400 mK. One possible explanation for our STM-imaged order-disorder transition could therefore be the crossover from individual to weak collective pinning between 2 and 5 T. However, we stress that there is no simple relationship between pinning strength and topology due to the different lengthscales governing each property: the pinning potential ranges over $\sim \xi$, whereas topological disorder is exhibited over lengthscales of the order of the vortex lattice constant $a \gg \xi$.

7.2.2 ...to the peak effect régime

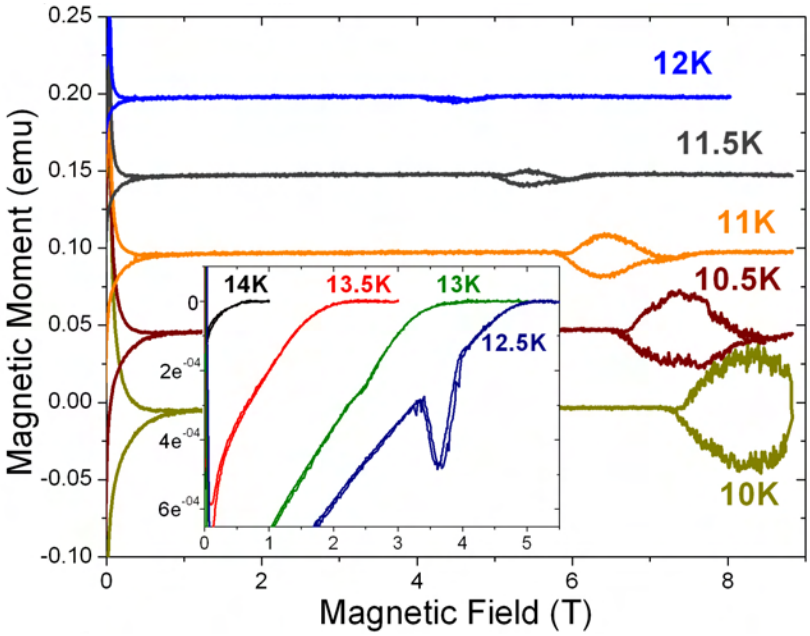

Figure 7.5: Magnetisation hysteresis loops at T = 10-12 K using a VSM. Inset: Hysteresis loops from 12.5-14 K using the more sensitive SQUID.

Order-disorder transitions in solid vortex matter are typically indicated by a peak effect, i.e. a jump in J_c due to enhanced pinning, accompanied by a strongly hysteretic zone in the sample magnetisation [168]. Compared with the cuprates, the peak effect in low-T_c superconductors is generally located at much higher fields and tempera-

tures just below $T_{c2}(H)$. Since ξ in $SnMo_6S_8$ lies between those found in low-T_cs and cuprates it is important to verify the existence and location of any peak effect.

Figure 7.5 displays magnetisation loops from 10 - 14 K: a clear peak effect may be seen below 14 K, broadening and moving linearly to higher fields as the temperature is reduced. $H_x(T)$ is located at far lower fields than this local hysteresis, i.e. the peak effect and the order-disorder transition imaged by STM are two separate phenomena.

7.3 High-field Heat Capacity Measurements

In common with most experimental probes, magnetisation data are sensitive to irreversible contributions from flux pinning. Conclusive information on the nature of any phase transition(s) underlying the peak effect may therefore only be obtained from a purely thermodynamic quantity, such as the specific heat. We have therefore carried out precise measurements of the electronic heat capacity in fields of up to 28T, focussing on the "back" of the jump just below $T_{c2}(H)$ since our magnetisation data reveal this to be the approximate location of the peak effect in phase space. As in section 6.2.1, all data was acquired using a high-resolution micro-calorimeter using the "long-relaxation technique" [147].

In Fig. 7.6 we show both the total (C) and electronic (C_{elec}) heat capacities of $SnMo_6S_8$ close to $T_{c2}(H)$. It should be noted that there is no evidence for any phase transition in the field or temperature ranges compatible with the onset of the magnetisation peak effect. However, at low fields a small lambda anomaly superimposed on the jump at $T_{c2}(H)$ is clearly visible, which is broadened and smeared out at higher fields. The transition and anomaly exhibit good 3D lowest-Landau-level (3D-LLL) scaling [169], as expected for the field range measured, thus confirming the fluctuation origin of the anomaly.

The situation in $SnMo_6S_8$ appears to be identical to that in Nb_3Sn, where a similar lambda anomaly has been shown to be representative of a metastable first order vortex melting transition [156, 157]. We therefore identify the peaks in C/T as approximate vortex lattice melting temperatures T_{VM}. At very high fields the lattice melting transition is blurred due to the increasing influence of thermal fluctuations and in particular the magnetic finite-size effect [69] broadening the neighbouring transition at $T_{c2}(H)$. The lambda anomaly is hence smeared out due to the large ΔT_c; however we may still approximate its loca-

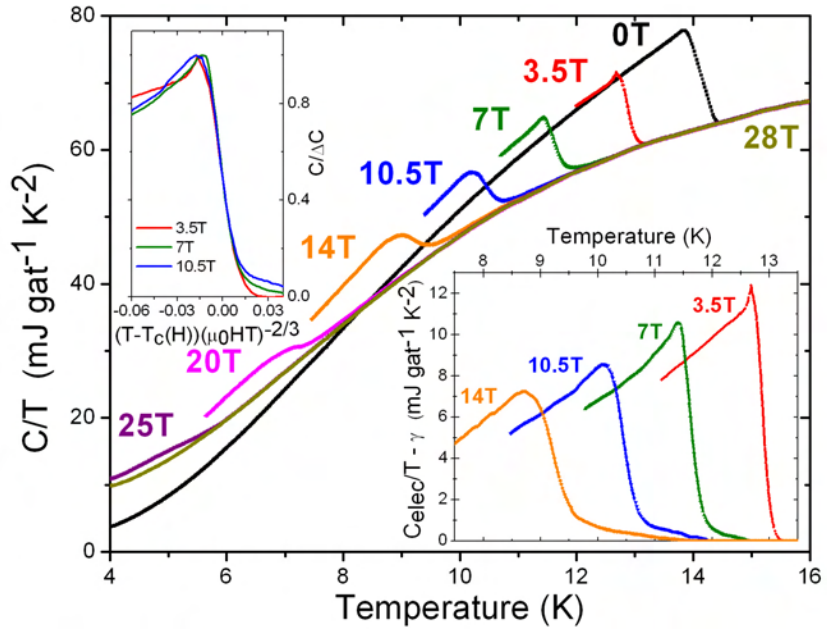

Figure 7.6: Total specific heat in $SnMo_6S_8$ from 0-28 T (the sample remains in the normal state at 28T above 4 K). The superconducting transition temperature $T_{c2}(H)$ is defined at the midpoint of the heat capacity jump. Right inset: Electronic specific heat C_{elec} = $C(H)/T$ - C(28T)/T for 3.5-14 T. Left inset: 3D-LLL scaling (see text) of C_{elec} for 3.5-10.5 T.

tion by observing the temperature at which C/T deviates from linear behaviour as we approach T_{c2} from below.

7.4 Vortex Phase Diagram

Combining data from bulk and local probes, we summarise the $SnMo_6S_8$ vortex phase diagram in Fig. 7.7.

The majority of phase space is occupied by a vortex glass, a remarkable result which at first glance is unexpected for a low-T_c material. However, our specific heat data provides an explanation for this prevalence of disorder. The absence of any latent heat (which would manifest itself as a spike in C/T at T_{VM}) implies that a kinetic glass tran-

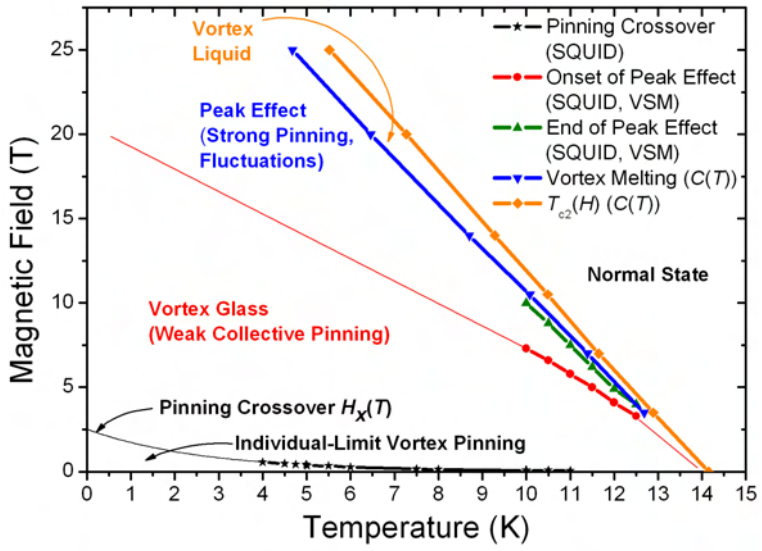

Figure 7.7: Vortex phase diagram of $SnMo_6S_8$. Measured data are displayed by points, extrapolated zones with thin lines.

sition takes place: the vortex liquid has been undercooled and frozen into a disordered solid (the vortex glass). This disorder persists beyond the peak effect region (which is merely the zone in which fluctuations from the melting transition enhance the pinning strength) down to low temperatures, except in the low-field limit where a quasi-ordered lattice (the Bragg glass) is stable. The defect-free structure observed at 2 T and 400 mK presents a positional order consistent with a Bragg glass, whilst the positionally and orientationally disordered high-field VS clearly indicate a vortex glass.

The possibility that the order-disorder transition between low and high-field phases coincides with the crossover from individual to collective pinning deserves further investigation. In the event that these two phenomena are linked, both the topology of the vortex glass and $H_x(T)$ are expected to vary with the speed of undercooling through T_{VM}. Ideally, future experiments should compare samples with different thermal histories to accurately probe the limits of disorder in the $SnMo_6S_8$ phase diagram.

Chapter 8

Vortex Core Spectroscopy in $PbMo_6S_8$ and $SnMo_6S_8$

Vortex cores in a type II superconductor present perhaps the ultimate spectroscopic test for any STM. Not only is the observation of a stable vortex lattice a serious experimental challenge, but the electronic states lying within the vortex cores are highly localised and susceptible to impurity scattering. However, the rewards are rich, with the potential for direct access to the normal-state spectra, Bogoliubov quasiparticle scattering and associated Fermiology [170], as well as the order parameter symmetry using s-wave [25] or d-wave models [171] for the bound states, if observable.

Previous STS experiments on $PbMo_6S_8$ at 2 K suggested the presence of an anomalous depression in the LDoS within the vortex cores: a pseudogap. Up until now, these experiments remained unrepeated and in the intervening period no reasonable explanation for the existence of such a pseudogap could be found. Perhaps the scans through the vortices had missed the true core centres due to vortex drift, thus creating an illusion of a gapped core? Alternatively, maybe there was a hidden phase transition opening a normal-state gap at $T^\star$, where $0 < T^\star < T_c$? The physics of Chevrel phase vortex cores remained shrouded in a cloak of uncertainty.

In this chapter we present new sub-Kelvin STS analysis of vortex cores in both $PbMo_6S_8$ and - for the first time - $SnMo_6S_8$. We confirm the existence of a pseudogap in the cores of each material. Our discovery of the two-band order parameter in Chevrel phase superconductors leads us to interpret this pseudogap as a consequence of strong inter-

band scattering.

8.1 Vortex Core Imaging

Both hexagonal Abrikosov lattices and disordered glassy vortex solids have been imaged in $SnMo_6S_8$ (as detailed in section 7.1.1) and $PbMo_6S_8$. The lattice stabilisation procedure is identical for each compound. We observe a similar reliance on high-quality flat surface topography for vortex imaging in $PbMo_6S_8$ as for $SnMo_6S_8$; the marginally lower surface quality in $PbMo_6S_8$ does not correlate with any vortex lattice defects, suggesting that the pinning is of a bulk 3D nature rather than originating from q2D surface effects.

8.1.1 $SnMo_6S_8$

Following the initial acquisition of a static vortex map at 5 T (fig. 7.2(b)), an attempt was made to fit the ZBC data using single-band s-wave theory, leaving both the vortex positions and the coherence length ξ as free parameters. The ZBC as a function of position $\mathbf{r}$, $\sigma(\mathbf{r})$, is given by

$$\sigma(\mathbf{r}) = \sigma(0) + \Lambda \sum_i \left(\cosh \frac{|\mathbf{r} - \mathbf{r_i}|}{\xi} \right)^{-2/\pi} \tag{8.1}$$

where σ_0 is the residual ZBC, Λ is a scaling factor and $\mathbf{r_i}$ is the location of the i^{th} vortex. The experimental data and fitted map are shown in fig. 8.1.

Our map provides an excellent reproduction of the vortex locations and yields a coherence length ξ = 28 Å. Using Ginzburg-Landau theory, this corresponds to H_{c2} = 42 T which is in perfect agreement with our heat capacity data and confirms the quality of our spectroscopic data. However, closer examination reveals a discrepancy between theory and experiment. Within the dirty limit, the ZBC should reach 1 at the centre of a vortex core; in the clean limit a ZBC peak with $\sigma > 1$ is to be expected. In our data, the ZBC consistently lies below 1 within the cores, suggesting that a gap persists inside the vortices. A 20 nm spectroscopic scan was therefore taken through a single vortex and is displayed in fig. 8.2.

As we move from the superconducting matrix towards the centre of the core, the superconducting gap clearly becomes narrower and shallower, with the ZBC rising and the coherence peaks being suppressed.

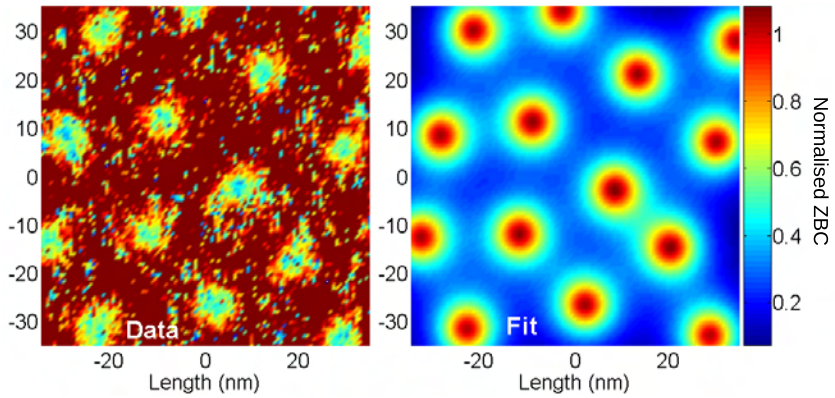

Figure 8.1: Left: Vortex contrast map in $SnMo_6S_8$ taken at 5 T. Right: Simulated ZBC map, generated using equation 8.1 and a least-squares fitting technique. Note that the colourbar values only correspond to the simulated map.

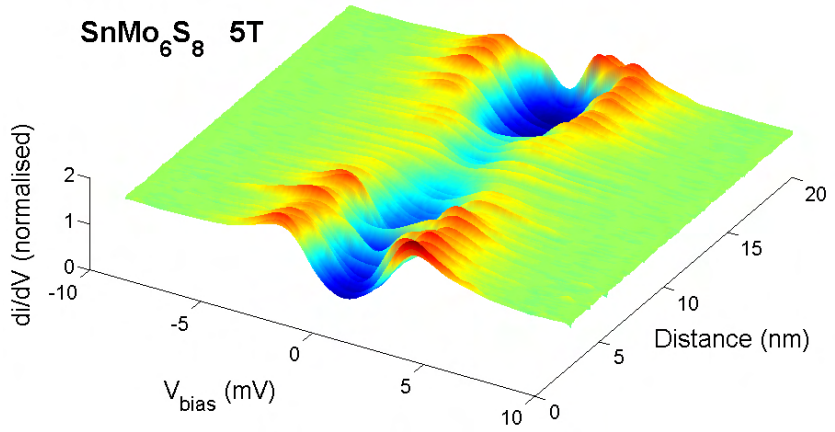

Figure 8.2: 20 nm spectroscopic trace through a vortex core in $SnMo_6S_8$ at H = 5 T.

However, it does not completely vanish at the centre of the core: the gap maintains a finite depth and width with σ_{ZBC} roughly 90% of σ_{peak} at maximum. A pseudogap therefore appears to be present within the vortex cores of $SnMo_6S_8$.

To confirm the existence of this pseudogap, it is necessary to verify that the spectrosopic trace probes the true centre of the vortex core. If the vortex moves prior to or during data collection, we will "miss" the core centre and thus create a false illusion of a pseudogapped core. This scenario was eliminated as follows: in order to increase the vortex separation (reducing the inter-vortex repulsive forces) and minimise field gradients, the magnetic field was reduced to 2 T. Following the imaging of a stable lattice at 400 mK, a single vortex was selected and mapped using a quick contrast scan (a procedure taking roughly 3 hours). On the basis of this map, a spectroscopic trace was immediately taken through the centre of the vortex. A typical trace requires 10-12 hours for data acquisition: given that our large-scale vortex maps have shown no signs of drift on timescales of up to 48 hours, we may be certain that we are penetrating the true centre of the core. The vortex core at 2 T is shown in fig. 8.3.

A pseudogap is indisputably present within the 2 T core. Just as seen at 5 T, the gap becomes both shallower and narrower towards the core centre, with σ_{ZBC} reaching a maximum at 65% of σ_{peak}. This suggests that the gap is gradually filled in as the applied field increases.

Let us now consider the spectral trends observed upon varying the magnetic field. By filtering vortex core areas out of a large-scale ZBC map, in principle it is possible to measure the ZBC variation with applied field in order to probe $\gamma(H)$ as detailed in section 1.2.3. Zero-field measurements yield a normalised ZBC of 0.17, while vortex maps at 5 T taken two weeks later have a higher value of 0.27. Using $H_{c2} \sim 40$ T from table 6.1 and assuming a normal-state ZBC of 1, within a crude approximation the rise in ZBC from 0 to 5 T roughly corresponds to what would be expected for a linear $\gamma(H)$ trend.

However, vortex maps at 2 T taken on the same surface one month later have a ZBC of around 0.36, rather than the expected value of ~ 0.21. Zero-field studies have already shown that the ZBC increases over time due to enhanced interband scattering resulting from surface deterioration (see section 6.1.3). Any future ZBC studies using STS should therefore be performed in a UHV environment within a very short timescale in order to avoid these surface-related problems.

Subsequent vortex mapping was performed at 7 T and 9 T, with pseudogapped cores consistently observed and $\sigma_{ZBC}/\sigma_{peak} \sim 95\%$ in each case. Due to the sample "ageing" discussed above and in section 6.1.3, it is imprudent to place great faith in any observed systematics in the ZBC or core spectral variation with applied field. However, the rapid jump from a relatively deep (65%) gap at 2 T to a shallow gap

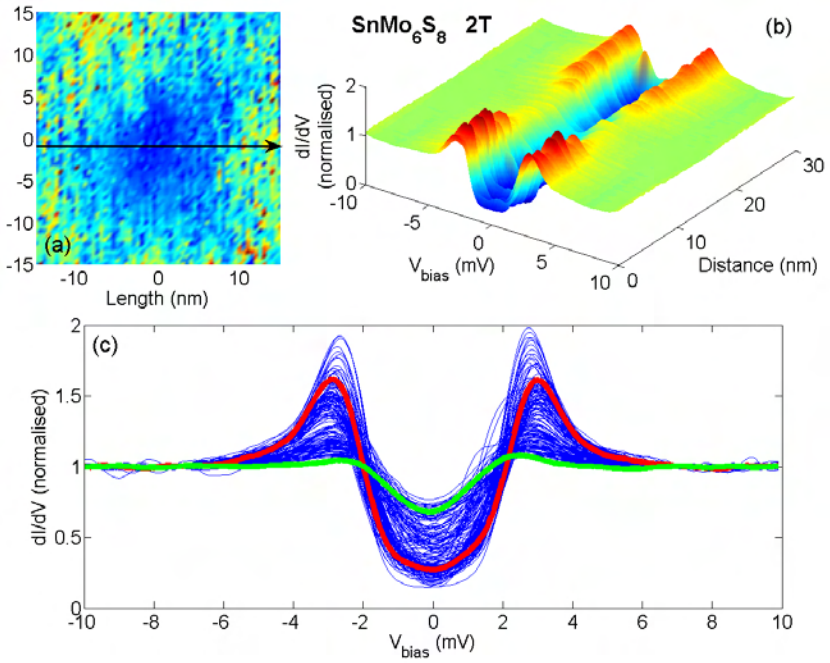

Figure 8.3: Vortex core spectroscopy in $SnMo_6S_8$ at 2 T. (a) Fast contrast map to pinpoint individual vortex, followed by (b) 30 nm spectroscopic scan through the centre of the core (trace depicted by arrow in (a)). (c) Superposition of spectra from the trace. A typical spectrum from the superconducting matrix outside the core is shown in red, while a spectrum from the centre of the core is highlighted in green.

saturating at 95% above 7 T should be considered in parallel with the crossover in $\gamma(H)$ measured by specific heat at 2.8 T (fig. 6.11). This is the first piece of evidence to link the pseudogap with multi-band superconductivity.

8.1.2 $PbMo_6S_8$

While far from straightforward, with a little practice vortex imaging in $SnMo_6S_8$ becomes relatively painless. Unfortunately the same cannot be said for $PbMo_6S_8$, due to the smaller crystals, poorer surface quality following cleavage and shorter coherence length (resulting in higher

vortex mobility). In fig. 8.4 we display a 250×250 nm image taken at 5 T, displaying a blurred and rather disordered vortex lattice. The map clearly has a lower resolution than similar data taken in $SnMo_6S_8$.

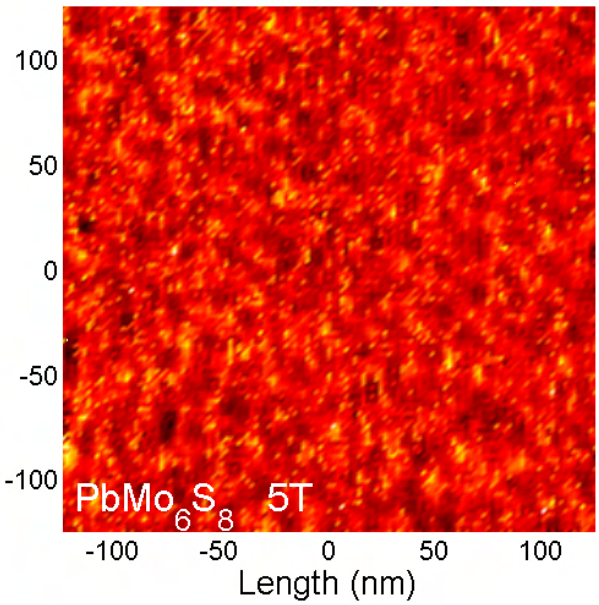

Figure 8.4: 250×250 nm vortex contrast map in $PbMo_6S_8$ measured at H = 5 T and T = 500 mK. Dark areas indicate vortex cores. A simpler yellow-red-black colourmap has been chosen to depict $PbMo_6S_8$ vortex data to avoid confusion due to the higher noise level.

However, the reason for these blurry images is not solely the lower surface quality. Fig. 8.5(a) displays a spectral trace through two vortices in $PbMo_6S_8$ at 5 T. Astonishingly, there is almost no change in the spectra when passing through a vortex core: the coherence peaks are partially suppressed as can be seen in fig. 8.5(c), but the ZBC remains almost unchanged. Therefore, the principal cause of vortex measurement difficulties in $PbMo_6S_8$ is simply that the vortices are almost indistinguishable from the surrounding superconducting matrix. This is well-illustrated by the contrast map in fig. 8.5(d), whose minimum value of 2.3 indicates that a deep gap persists throughout the entire vortex core.

It should be stressed that we find no evidence for anisotropic vor-

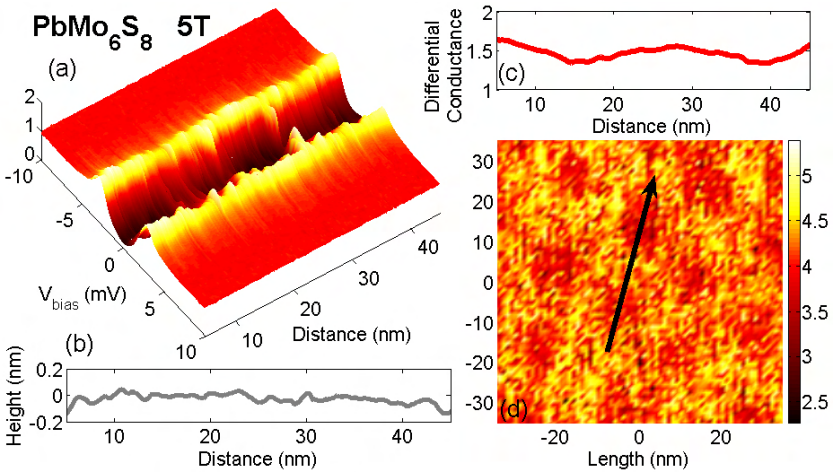

Figure 8.5: Vortex core spectroscopy in $PbMo_6S_8$ at 5 T. (a) 40 nm spectral trace, with topography shown in (b). (c) Variation of the differential conductance at the coherence peak energy, illustrating the depression of spectral weight characteristic of the vortex core. (d) Contrast map showing the path of the spectral trace in (a). The colourbar depicts the contrast $\sigma_{peak}/\sigma_{ZBC}$, with a minimum value of 2.3.

tex cores within our measurements. Anisotropic cores have previously been reported in $PbMo_6S_8$ [74]; however it was unclear whether these were intrinsic or merely a consequence of slow vortex drift at 2 K. An anisotropy in the coherence length of roughly 30% is expected from the angular variation dependence of H_{c2} [137] between parallel and perpendicular directions to the (111) ternary axis. However, considering the anisotropy of the minority band in the calculated Fermi surface in fig. 3.3, any anisotropy observed when tunnelling parallel to (100) or (001) should be small and have rotational symmetry of order 4, rather than order 2 as observed in [74]. Anisotropic vortices could conceivably be imaged by tunnelling parallel to (110), but since this is not a primary Chevrel phase cleavage plane it would be extremely difficult to obtain a sufficiently flat surface for any successful experiments.

8.2 Potential Origins of a Pseudogapped Core

Any mention of a pseudogap immediately evokes comparisons and parallels with high-T_c cuprates. However, we may quickly dismiss any such notions in the Chevrel phases for several reasons:

- The pseudogap in cuprates is a reflection of the normal state at low temperature in these materials. There is no reason to suspect that the normal state of q3D Chevrel phases should be anything other than a conventional ungapped Fermi liquid, since there are no known competing instabilities in these materials.

- If the STM-imaged pseudogap is due to non-phase-coherent pair formation, as postulated for high-T_c cuprates, it should be a precursor to superconductivity. This is a realistic scenario in the cuprates since the pseudogap opens above T_c. However, there is no pseudogap in Chevrel phase normal-state spectra above T_c (see fig. 6.7). The concept of a pairing pseudogap opening at $T^\star < T_c$ is unphysical, since pair formation and phase coherence must occur simultaneously at T_c.

- STM scans through vortex cores in cuprates indicate that the pseudogap is wider than the superconducting gap and lacks coherence peaks. In Chevrel phases the pseudogap is clearly smaller than the superconducting gap, decreasing to a minimum at the centre of the core, with blurred peaks still visible at the gap edges.

It is therefore necessary to seek a new and original explanation for the Chevrel pseudogap. Very few theoretical papers which treat the vortex cores of a two-band superconductor have been published and all of these have focussed on MgB_2 rather than a more general two-band system. However, a phenomenological model from Mourachkine has already predicted the existence of a pseudogap when probing the strongly-coupled band of a two-band superconductor [172]. Qualitatively, this is in excellent agreement with our results.

Nakai and coworkers were the first to consider the problem mathematically [173], calculating $\gamma(H)$ for MgB_2 and suggesting that in two-band superconductors $\gamma(H) \propto H^\alpha$. We note that such a model does not seem to be compatible with our results in chapter 6. Furthermore, no direct simulation of a vortex core was performed by the authors. An extension by the same group predicted anisotropic vortex cores for systems with anisotropic Fermi surfaces [174], but once again did not

consider inter-band scattering and concluded that the LDoS should be flat and ungapped within the cores (as is the case for MgB_2).

The next attempts were made by Koshelev and Golubov, who used coupled Usadel equations to extract characteristic length and energy scales for dirty two-band superconductors [175], closely followed by Gurevich who used a similar method to calculate the upper critical field [176]. Whilst able to perfectly reproduce and interpret tunnelling data on MgB_2 [55], once again these models assume negligible inter-band scattering and therefore cannot be applied to the Chevrel phases. A more promising approach is that taken by Tanaka and colleagues, who combine quasi-classical Eilenberger and Usadel equations to calculate the vortex LDoS in a two-band superconductor with one band ballistic and the other diffusive [177, 178]. It is hoped that this model should permit inter-band scattering to be incorporated relatively easily in order to test our results.

In the current absence of a theoretical model, we will make our own brief hypothesis as to the origin of the pseudogap. We have demonstrated beyond reasonable doubt that $PbMo_6S_8$ and $SnMo_6S_8$ are two-band superconductors, with one band contributing a majority of the density of states and enjoying a stronger coupling than the minority band. Whether this leads the majority band to feature ballistic electron transport and the minority band diffusive transport remains to be seen. The unique characteristic of Chevrel phase superconductors is the strong inter-band scattering between these two bands. Since two-band superconductors without inter-band scattering (such as MgB_2) have flat ungapped cores, regardless of the incident tunnelling direction [55, 60], we therefore propose that this inter-band scattering is responsible for the pseudogap in the vortex cores in Chevrel phases.

How can inter-band scattering produce such a gap? We tentatively suggest that the circulating current which generates the vortex is predominantly carried by the majority band, whilst the minority band remains superconducting, or at the very least retains a pairing gap if not phase coherence. This is presumably due to our tunnelling configuration and field orientation, which lead to the minority band not carrying any vortex current due to the anisotropy of its Fermi surface. The strong inter-band scattering consequently allows us to indirectly probe the density of states of this gapped band. This model explains why the pseudogap tends to a finite minimum within the cores and retains coherence peaks: it is approaching the value of Δ_2, the minority band superconducting gap.

However, it is unclear why the gap remains so deep when the minority band should only contribute as little as 10% of the DoS within our tunnelling configuration. In particular, why is the pseudogap so much deeper in $PbMo_6S_8$ than in $SnMo_6S_8$? There are two partial explanations for this: firstly, our $PbMo_6S_8$ crystals are dirtier than the $SnMo_6S_8$ samples and hence should have greater inter-band scattering. If the scattering is directly responsible for the opening of the pseudogap, increased scattering should produce a deeper gap. Secondly, the depth of the pseudogap may scale with H_{c2}, although no model currently exists to support or erode this hypothesis. Only one thing is clear: the world of superconductivity is in urgent need of a theoretical description of dirty two-band superconductors with strong inter-band scattering!

Conclusions

Superconductivity in $M_2Mo_6Se_6$

Our heat capacity and resistivity measurements have shown that superconductivity in $Tl_2Mo_6Se_6$ and $In_2Mo_6Se_6$ is principally mediated by an internal phonon from the Mo_6Se_6 chains, with an energy in the 12-18 meV range. It is hoped that theoretical calculations will soon identify the precise energy and nature of this vibrational mode. $Tl_2Mo_6Se_6$ exhibits an additional coupling to an optical mode at $\sim$5 meV due to a "rattling" motion of the Tl^+ ion between the chains.

The low-temperature specific heat of $In_2Mo_6Se_6$ is well-fitted by a standard single-gap isotropic s-wave BCS model with $2\Delta_0/k_BT_c = 3.5\pm0.1$. However, the additional interaction with the low-energy mode in $Tl_2Mo_6Se_6$ pushes it into the strong coupling régime with $2\Delta_0/k_BT_c \geq 5$. The specific heat jump at T_c also exhibits a significant deformation with a shift in states to low temperature, which we attribute to strong low-dimensional fluctuations. STM or similar tunnelling experiments would provide conclusive proof of the gap symmetry, as well as displaying the coupling to the low-energy phonon. Despite the challenging surface conditions, we feel that $Tl_2Mo_6Se_6$ is a good candidate for a future STM study on low-dimensional ultra-strongly-coupled superconductors.

Metal-Insulator Transitions in $M_2Mo_6Se_6$

Combining transport, tunnelling and XRD data, we argue that the observed metal-insulator transition in $M_2Mo_6Se_6$ (M= Group IA ion) is due to the onset of a fluctuating electronic charge density wave. The formation of this novel phase is driven by the strong electronic anisotropy in $M_2Mo_6Se_6$ resulting from two highly-nested Fermi planes. This anisotropy increases as we move down Group IA, explaining the

corresponding increase in T_{MI} and the electrical transport activation energy.

We propose a phase diagram consisting of two neighbouring domes, representing density wave and superconducting groundstates. These domes should be separated by a quantum critical point: $M_2Mo_6Se_6$ therefore offers enormous potential for studying quantum fluctuations on the boundary of two competing instabilities.

Multi-band Chevrel Phase Superconductivity

Sub-Kelvin scanning tunnelling spectroscopy in the Chevrel phases $SnMo_6S_8$ and $PbMo_6S_8$ reveals two distinct superconducting gaps with Δ_1 = 3 meV, $\Delta_2 \sim$ 1.0 meV and Δ_1 = 3.1 meV, $\Delta_2 \sim$ 1.4 meV respectively. The gap distribution is strongly anisotropic, with Δ_2 predominantly seen when scanning across unit-cell steps on the (001) sample surface. The spectra are well-fitted by an anisotropic two-band BCS s-wave gap function.

Our spectroscopic data are confirmed by electronic heat capacity measurements: two-gap fits to the specific heat provide similar couplings and DoS ratios to those measured by STM. The variation of the electronic heat capacity with field $\gamma(H)$ has a characteristic bend at low fields (2.8 T in $SnMo_6S_8$ and 3.4 T in $PbMo_6S_8$), indicative of a two-band superconducting order parameter. Together, these data provide conclusive and indisputable evidence for multi-band superconductivity in the Chevrel phases. A transition from double-gap to anisotropic single-gap spectra over a period of several months further hints at the significance of the high inter-band scattering in these materials.

Real-space Vortex Glass Imaging in $SnMo_6S_8$

Using scanning tunnelling microscopy at 400 mK, we have obtained maps of around 100 vortices in $SnMo_6S_8$ from 2 - 9 T. The orientational and positional disorder at 5 and 9 T show that these are the world's first large-scale images of a vortex glass. At lower fields, a quasi-ordered hexagonal lattice is observed, which presumably corresponds to the Bragg glass phase. Magnetic and thermodynamic data taken at higher temperature reveal a magnetisation peak effect, whose upper boundary coincides with a lambda anomaly in the specific heat. Our data favour a kinetic glass description of the vortex melting transition, indicating

that vortex topological disorder persists at fields and temperatures far below the peak effect in low-T_c superconductors.

This work therefore removes a large part of the confusion surrounding the peak effect, in particular the hypothesised order-disorder transition at its lower boundaries. We see no thermodynamic or topological evidence for such a transition and believe that the peak effect is merely a zone of enhanced pinning due to increasingly important thermal fluctuations as we approach the vortex lattice melting transition.

Vortex Core Spectroscopy in $SnMo_6S_8$ and $PbMo_6S_8$

Vortex core spectra in $SnMo_6S_8$ display a shallow pseudogap, whose depth decreases with increasing magnetic field. A much wider and deeper pseudogap is visible in $PbMo_6S_8$, with spectra scarcely changing as we enter the vortex core from the superconducting matrix. This is a totally new phenomenon, distinct from the pseudogap seen in high-T_c cuprates: no other superconductor has ever exhibited a similar pseudogapped vortex core. MgB_2 is the only remotely similar multi-band superconductor whose vortex cores have been investigated and no such pseudogap is observed in this compound.

One of the most important differences between MgB_2 and the Chevrel phases is the absence of inter-band scattering in the former and its presence in the latter. We therefore propose that the observed pseudogap in Chevrel phase vortex cores is a direct consequence of this scattering. Since the depth of the pseudogap appears to scale with H_{c2}, we also suggest that the inter-band scattering is largely responsible for such high H_{c2} values in $SnMo_6S_8$ and $PbMo_6S_8$. Perhaps the most important conclusion of this work is therefore that multi-band superconductivity with strong intrinsic inter-band scattering should be the first ingredient in any future recipe for a high critical field superconductor.

Bibliography

[1] H. Kamerlingh Onnes, *Leiden Comm.*, 120b, 122b, 124c, 1911.
[2] C.J. Gorter and H.B.G. Casimir, *Phys. Z.*, 35, 963, 1934.
[3] F. London and H. London, *Proc. R. Soc. A*, 149, 71, 1935.
[4] V.L. Ginzburg and L.D. Landau, *Zh. Eksp. Teor. Fis.*, 20, 1064, 1950.
[5] J. Bardeen, L.N. Cooper, and J.R. Schrieffer, *Phys. Rev.*, 108, 1175, 1175.
[6] L.P. Gor'kov, *Sov. Phys. - JETP*, 7, 505, 1958.
[7] G.M. Eliashberg, *Sov. Phys. - JETP*, 11, 696, 1960.
[8] R. Chevrel, M. Sergent, and J. Prigent, *J. Solid State Chem.*, 3, 515, 1971.
[9] F. Steglich, J. Aarts, C.D. Bredl, W. Lieke, D. Meschede, W. Franz, and H. Schäfer, *Phys. Rev. Lett.*, 43, 1892, 1979.
[10] D. Jérome, A. Mazaud, M. Ribault, and K. Bechgaard, *J. Phys. Lett.*, 41, L95, 1980.
[11] J.G. Bednorz and K.A. Müller, *Z. Physik B*, 64, 189, 1986.
[12] M. K. Wu, J. R. Ashburn, C. J. Torng, P. H. Hor, R. L. Meng, L. Gao, Z. J. Huang, Y. Q. Wang, and C. W. Chu, *Phys. Rev. Lett.*, 58, 908, 1987.
[13] L. Gao, Y. Y. Xue, F. Chen, Q. Xiong, R. L. Meng, D. Ramirez, C. W. Chu, J. H. Eggert, and H. K. Mao, *Phys. Rev. B*, 50, 4260, 1994.
[14] C. Panagopoulos, A. P. Petrović, A. D. Hillier, J. L. Tallon, C. A. Scott, and B. D. Rainford, *Phys. Rev. B*, 69, 144510, 2004.
[15] P.W. Anderson, P.A. Lee, M. Randeria, T.M. Rice, N. Trivedi, and F.C. Zhang, *J. Phys. Cond. Mat.*, 16, R755, 2004.
[16] R.B. Laughlin, *Phil. Mag.*, 86, 1165, 2006.
[17] C. Varma, *Phys. Rev. B*, 73, 155113, 2006.
[18] C. C. Tsuei, J. R. Kirtley, C. C. Chi, Lock See Yu-Jahnes, A. Gupta, T. Shaw, J. Z. Sun, and M. B. Ketchen, *Phys. Rev.*

Lett., 73, 593, 1994.
[19] K. Maki, G.-f. Wang, and H. Won, *J. Superconductivity*, 12, 551, 1999.
[20] A.T. Holmes, D. Jaccard, G. Behr, Y. Inada, and Y. Onuki, *J. Phys.: Condens. Matter*, 16, 1121, 2004.
[21] K. Izawa, H. Takahashi, H. Yamaguchi, Yuji Matsuda, M. Suzuki, T. Sasaki, T. Fukase, Y. Yoshida, R. Settai, and Y. Onuki, *Phys. Rev. Lett.*, 86, 2653, 2001.
[22] M. Kugler, Ø. Fischer, Ch. Renner, S. Ono, and Yoichi Ando, *Phys. Rev. Lett.*, 86, 4911, 2001.
[23] J.W. Loram, J.L. Luo, J.R. Cooper, W.Y. Liang, and J.L. Tallon, *Physica C*, 341-348, 831, 2000.
[24] Takeshi Kondo, Rustem Khasanov, Tsunehiro Takeuchi, Jörg Schmalian, and Adam Kaminski, *Nature*, 457, 296, 2009.
[25] François Gygi and Michael Schluter, *Phys. Rev. B*, 41, 822, 1990.
[26] V. Braccini *et al.*, *Phys. Rev. B*, 71, 012504, 2005.
[27] R. Flükiger, C. Senatore, M. Cesarette, F. Buta, D. Uglietti, and B. Seeber, *Supercond. Sci. Technol.*, 21, 054015, 2008.
[28] Y. Kamihara, T. Watanabe, M. Hirano, and H. Hosono, *J. Am. Chem. Soc.*, 130, 3296, 2008.
[29] Zheng Wei, HaiŠou Li, Wei-Li Hong, Zhangming Lv, Huiyan Wu, Xiufeng Guo, and Keqing Ruan, *J. Supercond. Nov. Magn.*, 21, 213, 2008.
[30] I.I. Mazin, D.J. Singh, M.D. Johannes, and M.H. Du, *Phys. Rev. Lett.*, 101, 057003, 2008.
[31] F. Hunte, J. Jaroszynski, A. Gurevich, D.C. Larbalestier, R. Jin, A.S. Sefat, M.A. McGuire, B.C. Sales, D.K. Christen, and D. Mandrus, *Nature*, 453, 903, 2008.
[32] M. Potel, R. Chevrel, M. Sergent, J.C. Armici, M. Decroux, and Ø. Fischer, *J. Solid State Chem.*, 35, 286, 1980.
[33] M. Decroux and Ø. Fischer, in *Superconductivity in Ternary Compounds II*, pages 57–98. Springer-Verlag: Berlin, Heidelberg, New York, 1982.
[34] Ø. Fischer, A. Treyvaud, R. Chevrel, and M. Sergent, *Solid State. Commun.*, 17, 721, 1975.
[35] C. Dubois, A.P. Petrović, G. Santi, C. Berthod, A.A. Manuel, M. Decroux, Ø. Fischer, M. Potel, and R. Chevrel, *Phys. Rev. B*, 75, 104501, 2007.
[36] Filipe J. Ribeiro, David J. Roundy, and Marvin L. Cohen, *Phys. Rev. B*, 65, 153401, 2002.
[37] A. Petrović, Y. Fasano, R. Lortz, M. Decroux, M. Potel, R. Chevrel,

and Ø. Fischer, *Physica C*, 2, 3, 2007.
[38] F. Pobell, D. Rainer, and H. Wühl, in *Superconductivity in Ternary Compounds I*, pages 251–276. Springer-Verlag: Berlin, Heidelberg, New York, 1982.
[39] G. Binnig and H. Rohrer, *Helv. Phys. Acta.*, 55, 726, 1982.
[40] Ø. Fischer, M. Kugler, I. Maggio-Aprile, C. Berthod, and Ch. Renner, *Rev. Mod. Phys.*, 79, 353, 2007.
[41] R. Wiesendanger, *Scanning Probe Microscopy and Spectroscopy - Methods and Applications*. Cambridge University Press, 1994.
[42] J. Bardeen, *Phys. Rev. Lett.*, 6, 57, 1961.
[43] C.J. Chen, *Phys. Rev. B*, 42, 8841, 1990.
[44] C.J. Chen, *Phys. Rev. Lett.*, 65, 448, 1990.
[45] A. Piriou, N. Jenkins, Y. Fasano, I. Maggio-Aprile, E. Giannini, A.A. Manuel, and Ø. Fischer. Manuscript in preparation, 2009.
[46] Walter A. Harrison, *Phys. Rev.*, 123, 85, 1961.
[47] P.W. Anderson and Ong. N.P., *J. Phys. Chem. Solids*, 67, 1, 2006.
[48] G. Levy, C. Berthod, A. Piriou, E. Giannini, A.A. Manuel, and Ø. Fischer. Manuscript accepted for publication in Phys. Rev. Lett., 2009.
[49] R. Dynes, V. Narayanamurti, and J. Garno, *Phys. Rev. Lett.*, 41, 1509, 1978.
[50] C. Dubois, G. Santi, I. Cuttat, C. Berthod, N. Jenkins, A.P. Petrović, A.A. Manuel, Ø. Fischer, S.M. Kazakov, Z. Bukowski, and J. Karpinski, *Phys. Rev. Lett.*, 101, 057004, 2008.
[51] J.R. Waldram, *Superconductivity of metals and cuprates*. Institute of Physics Publishing, 1996.
[52] A. Abrikosov, *Sov. Phys. JETP*, 5, 1175, 1957.
[53] C. Caroli, P. de Gennes, and J. Matricon, *Physics Letters*, 9, 307, 1964.
[54] H. F. Hess, R. B. Robinson, and J. V. Waszczak, *Phys. Rev. Lett.*, 64, 2711, 1990.
[55] M. R. Eskildsen, M. Kugler, S. Tanaka, J. Jun, S. M. Kazakov, J. Karpinski, and Ø. Fischer, *Phys. Rev. Lett.*, 89, 187003, 2002.
[56] Ch. Renner, A.D. Kent, Ph. Niedermann, and Ø. Fischer, *Phys. Rev. Lett.*, 67, 1650, 1991.
[57] H. Suhl, B.T. Matthias, and L.R. Walker, *Phys. Rev. Lett.*, 3, 552, 1959.
[58] L.Y.L. Shen, N.M. Senozan, and N.E. Phillips, *Phys. Rev. Lett.*, 14, 1025, 1965.
[59] G. Binnig, A. Baratoff, H.E. Hoenig, and J.G. Bednorz, *Phys. Rev. Lett.*, 45, 1352, 1980.

[60] M. R. Eskildsen, N. Jenkins, G. Levy, M. Kugler, Ø. Fischer, J. Jun, S. M. Kazakov, and J. Karpinski, *Phys. Rev. B*, 68, 100508, 2003.
[61] Y. Wang, F. Bouquet, I. Sheikin, P. Toulemonde, B. Revaz, M. Eisterer, H. Weber, J. Hinderer, and A. Junod, *J. Phys.: Condens. Matter*, 15, 883, 2003.
[62] C. Kittel, *Introduction to Solid State Physics*. John Wiley & Sons, Inc., 1996.
[63] B. Mühlschlegel, *Z. Physik*, 155, 313, 1959.
[64] H. Padamsee, J.E. Neighbor, and C.A. Shiffman, *J. Low Temp. Phys.*, 12, 387, 11973.
[65] F. Bouquet, Y. Wang, R.A. Fisher, D.G. Hinks, J.D. Jorgensen, A. Junod, and N.E. Phillips, *Europhys. Lett.*, 56, 856, 2001.
[66] R. Lortz, R. Viennois, A. Petrovic, Y. Wang, P. Toulemonde, C. Meingast, M.M. Koza, H. Mutka, A. Bossak, and A. San Miguel, *Phys. Rev. B*, 77, 224507, 2008.
[67] O.J. Taylor, A. Carrington, and J.A. Schlueter, *Phys. Rev. Lett.*, 99, 057001, 2007.
[68] G.E. Volovik, *JETP Lett.*, 58, 469, 1993.
[69] R. Lortz, C. Meingast, A.I. Rykov, and S. Tajima, *Phys. Rev. Lett.*, 91, 207001, 2003.
[70] J.W. Alldredge, Jinho Lee, K. McElroy, M. Wang, K. Fujita, Y. Kohsaka, C. Taylor, H. Eisaki, S. Uchida, P.J. Hirschfeld, and J.C. Davis, *Nature Physics*, 4, 319, 2008.
[71] J.G. Weisend, *Handbook of Cryogenic Engineering*. Taylor & Francis, Inc., 1998.
[72] C. Renner, PhD thesis, Université de Genève, 1994.
[73] M. Kugler, PhD thesis, Université de Genève, 2001.
[74] C. Dubois, PhD thesis, Université de Genève, 2005.
[75] Phasis Sàrl, Chemin des Aulx 18, CH-1228 Plan-les-Ouates, Geneva, Switzerland.
[76] L. Stark. *Datasheet Régulation STM*, 2004.
[77] STM Control Software, A. A. Manuel, Université de Genève 2002.
[78] S. Urazhdin, H. Tessmer, and R. Ashoori, *Rev. Sci. Instrum.*, 73, 310, 2002.
[79] A. Junod, in *Studies of High Temperature Superconductors*, volume 19, page 1. Nova Science Publishers, Commack, New York, 1996.
[80] B.T. Matthias, M. Marezio, E. Corenzwit, A.S. Cooper, and H.E. Barz, *Science*, 175, 1465, 1972.
[81] R. Odermatt, Ø. Fischer, H. Jones, and G. Bongi, *J. Phys. C*, 7,

13, 1974.
[82] Ø. Fischer, H. Jones, G. Bongi, M. Sergent, and R. Chevrel, *J. Phys. C*, 7, 450, 1974.
[83] M. Marezio, P.D. Dernier, J.P. Remeika, E. Corenzwit, and B.T. Matthias, *Mater. Res. Bull.*, 8, 657–68, 1973.
[84] J. Guillevic, O. Bars, and D. Grandjean, *Acta Cryst.*, B32, 1342, 1976.
[85] L. F. Mattheiss and C. Y. Fong, *Phys. Rev. B*, 15, 1760, 1977.
[86] O. K. Andersen, W. Klose, and H. Nohl, *Phys. Rev. B*, 17, 1209, 1978.
[87] S. D. Bader, G. S. Knapp, S. K. Sinha, P. Schweiss, and B. Renker, *Phys. Rev. Lett.*, 37, 344, 1976.
[88] U. Poppe and H. Wühl, *J. Low Temp. Phys.*, 43, 371, 1981.
[89] S. Picard, J. Saillard, P. Gougeon, H. Noël, and M. Potel, *J. Solid State. Chem.*, 155, 417–426, 2000.
[90] R. Brusetti, O. Laborde, A. Sulpice, R. Calemczuk, M. Potel, and P. Gougeon, *Phys. Rev. B*, 52, 4481, 1995.
[91] J.C. Armici, M. Decroux, Ø. Fischer, M. Potel, R. Chevrel, and M. Sergent, *Solid State Commun.*, 33, 607–611, 1980.
[92] M. Potel, R. Chevrel, and M. Sergent, *Acta Cryst.*, B36, 1545–1548, 1980.
[93] J.M. Tarascon, F.J. DiSalvo, and J.V. Waszczak, *Solid State Commun.*, 52, 227, 1984.
[94] L. Venkataraman and C.M. Lieber, *Phys. Rev. Lett.*, 83, 5334, 1999.
[95] P.J. Kelly and O.K. Andersen, in *Superconductivity in d- and f-Band Metals*, pages 134–140. Academic Press: New York, 1982.
[96] H. Nohl and O.K. Andersen, in *Superconductivity in d- and f-Band Metals*, pages 161–165. Academic Press: New York, 1982.
[97] L. Boeri, J. Kortus, and O. Andersen. Private communication, 2007.
[98] A. Petrović, R. Lortz, G. Santi, M. Decroux, H. Monnard, Ø. Fischer, L. Boeri, O. Andersen, J. Kortus, D. Salloum, P. Gougeon, and M. Potel. Manuscript submitted to Phys. Rev. B, 2009.
[99] R. Lepetit, P. Monceau, M. Potel, P. Gougeon, and M. Sergent, *Journal of Low Temperature Physics*, 56, 219, 1984.
[100] T. Mori, Y. Yokogawa, A. Kobayashi, Y. Sasaki, and H. Kobayashi, *Solid State Commun.*, 49, 249–252, 1984.
[101] M. Potel and P. Gougeon. Private communication, 2008.
[102] E. Bonjour, R. Calemczuk, Khoder. A.F., P. Gougeon, M. Potel, and M. Sergent, in *Proceedings of the 2nd International Confer-*

ence on Phonon Physics, Budapest, 1985, page 570. World Scientific, Singapore, 1985.
[103] R. Brusetti, P. Monceau, M. Potel, P. Gougeon, and M. Sergent, *Solid State Commun.*, 66, 181–187, 1988.
[104] R. Brusetti, A.J. Dianoux, P. Gougeon, M. Potel, E. Bonjour, and R. Calemczuk, *Phys. Rev. B*, 41, 6315, 1990.
[105] R. Brusetti, A.J. Dianoux, P. Gougeon, M. Potel, E. Bonjour, and R. Calemczuk, *Europhys. Lett.*, 10, 563, 1989.
[106] M. Hoesch, A. Petrović, D. Chernyshov, A. Bossak, D. Salloum, P. Gougeon, and M. Potel. Manuscript in preparation, 2009.
[107] P.H. Hor, W.C. Fan, L.S. Chou, R.L. Meng, C.W. Chu, J.M. Tarascon, and M.K. Wu, *Solid State Commun.*, 55, 231–235, 1985.
[108] P.H. Hor, R.L. Meng, C.W. Chu, J.M. Tarascon, and M.K. Wu, *Physica B+C*, 135, 245–247, 1985.
[109] G.X. Tessema, Y.T. Tseng, M.J. Skove, E.P. Stillwell, R. Brusetti, P. Monceau, M. Potel, and P. Gougeon, *Phys. Rev. B*, 43, 3434, 1991.
[110] R. M. Fleming and C. C. Grimes, *Phys. Rev. Lett.*, 42, 1423, 1979.
[111] R. Brusetti, A. Briggs, O. Laborde, M. Potel, and P. Gougeon, *Phys. Rev. B*, 49, 8931, 1994.
[112] T.M. Mishonov, G.V. Pachov, I.N. Genchev, L.A. Atanasova, and D.C. Damianov, *Phys. Rev. B*, 68, 054525, 2003.
[113] T. Giamarchi, *Phys. Rev. B*, 44, 2905, 1991.
[114] R. Lortz, Y. Wang, S. Abe, C. Meingast, Yu. B. Paderno, V. Filippov, and A. Junod, *Phys. Rev. B*, 72, 024547, 2005.
[115] R. Lortz, Y. Wang, U. Tutsch, S. Abe, C. Meingast, P. Popovich, W. Knafo, N. Shitsevalova, Yu. B. Paderno, and A. Junod, *Phys. Rev. B*, 73, 024512, 2006.
[116] G. Grimvall, *The Electron-Phonon Interaction in Metals*, pages 212–219. North-Holland: Amsterdam, 1981.
[117] P.B. Allen and R.C. Dynes, *Phys. Rev. B*, 12, 905, 1975.
[118] P.A. Lee, T.M. Rice, and P.W. Anderson, *Phys. Rev. Lett.*, 31, 462, 1973.
[119] N.P. Ong and P. Monceau, *Phys. Rev. B*, 16, 3443, 1977.
[120] A. Fournel, J.P. Sorbier, M. Konczykowski, and P. Monceau, *Phys. Rev. Lett.*, 57, 2199, 1986.
[121] D. Purdie, I.R. Collins, H. Berger, G. Margaritondo, and B. Reihl, *Phys. Rev. B*, 50, 222, 1994.
[122] S. Roth and D. Carroll, *One-dimensional metals*. Wiley-VCH, 2004.
[123] J.M.E. Harper, T.H. Geballe, and F.J. DiSalvo, *Phys. Rev. B*, 15,

2943, 1977.
[124] S. Seiro, Y. Fasano, I. Maggio-Aprile, E. Koller, O. Kuffer, and Ø. Fischer, *Phys. Rev. B*, 77, 020407, 2008.
[125] M. Hoesch, A. Petrović, H. Hedgeland, D. Salloum, P. Gougeon, and M. Potel. Manuscript in preparation, 2009.
[126] N.F. Mott, *Proc. R. Soc. London A*, 382, 1, 1982.
[127] D. Jérome, T. M. Rice, and W. Kohn, *Phys. Rev.*, 158, 462, 1967.
[128] G. Giuliani, E. Tosatti, and M.P. Tosi, *J. Phys. C*, 12, 2769, 1979.
[129] J.M. Luttinger, *J. Math. Phys.*, 4, 1154, 1963.
[130] T. Giamarchi, *Quantum Physics in One Dimension*. Clarendon Press, Oxford, 2004.
[131] C. Zhou and C. Gong, *J. Phys. C: Solid State Phys.*, 21, 561–566, 1988.
[132] B. Dóra, A. Ványolos, and A. Virosztek, *Phys. Rev. B*, 73, 125110, 2006.
[133] A. Ványolos, B. Dóra, and A. Virosztek, *Phys. Rev. B*, 73, 165127, 2006.
[134] B. Dardel, D. Malterre, M. Grioni, P. Weibel, Y. Baer, and F. Lévy, *Phys. Rev. Lett.*, 67, 3144, 1991.
[135] Latha Venkataraman, Yeon Suk Hong, and Philip Kim, *Phys. Rev. Lett.*, 96, 076601, 2006.
[136] N.E. Werthamer, E. Helfand, and P.C. Hohenberg, *Phys. Rev.*, 147, 295, 1966.
[137] M. Decroux, PhD thesis, University of Geneva, 1980.
[138] J. Nagamatsu, N. Nakagawa, T. Muranaka, Y. Zenitani, and J. Akimitsu, *Nature*, 410, 63, 2001.
[139] F. Bouquet, Y. Wang, I. Sheikin, T. Plackowski, A. Junod, S. Lee, and S. Tajima, *Phys. Rev. Lett.*, 89, 257001, 2002.
[140] B. Bergk, V. Petzold, H: Rosner, S.-L. Drechsler, M. Bartkowiak, O. Ignatchik, A.D. Bianchi, I. Sheikin, P.C. Canfield, and J. Wosnitza, *Phys. Rev. Lett.*, 100, 257004, 2008.
[141] S. Kuroiwa, Y. Saura, J. Akimitsu, M. Hiraishi, M. Miyazaki, K.H. Satoh, S. Takeshita, and R. Kadono, *Phys. Rev. Lett.*, 100, 097002, 2008.
[142] R.W. Hill, S. Li, M.B. Maple, and L. Taillefer, *Phys. Rev. Lett.*, 101, 237005, 2008.
[143] W. L. McMillan, *Phys. Rev.*, 175, 537, 1968.
[144] Amy. Y. Liu, I.I. Mazin, and Jens Kortus, *Phys. Rev. Lett.*, 87, 087005, 2001.
[145] I.I. Mazin, O.K. Andersen, O. Jepsen, O.V. Dolgov, J. Kortus, A.A. Golubov, A.B. Kuz'menko, and D. van der Marel, *Phys. Rev. Lett.*,

89, 107002, 2002.
[146] F. Giubileo, D. Roditchev, W. Sacks, R. Lamy, D. X. Thanh, J. Klein, S. Miraglia, D. Fruchart, J. Marcus, and Ph. Monod, *Phys. Rev. Lett.*, 87, 177008, 2001.
[147] R. Lortz, Y. Wang, A. Demuer, P.H. Böttger, B. Bergk, G. Zwicknagl, Y. Nakazawa, and J. Wosnitza, *Phys. Rev. Lett*, 99, 187002, 2007.
[148] D. W. Bullett, *Phys. Rev. Lett.*, 39, 664, 1977.
[149] A. A. Golubov and A. E. Koshelev, *Phys. Rev. B*, 68, 104503, 2003.
[150] Daniel S. Fisher, Matthew P. A. Fisher, and David A. Huse, *Phys. Rev. B*, 43, 130, 1991.
[151] Thierry Giamarchi and Pierre Le Doussal, *Phys. Rev. B*, 52, 1242, 1995.
[152] Grigorii P. Mikitik and Ernst Helmut Brandt, *Phys. Rev. B*, 64, 184514, 2001.
[153] S.S. Banerjee, A.K. Grover, M.J. Higgins, Gutam I. Menon, P.K. Mishra, D. Pal, S. Ramakrishnan, T.V. Chandrasekhar Rao, G. Ravikumar, V.C. Sahni, S. Sarkar, and C.V. Tomy, *Physica C*, 355, 39–50, 2001.
[154] A.I. Larkin and Yu. N. Ovchinnikov, *J. Low Temp. Phys.*, 34, 409, 1979.
[155] M.J. Higgins and S. Bhattacharya, *Physica C*, 257, 232, 1996.
[156] R. Lortz, F. Lin, N. Musolino, Y. Wang, A. Junod, B. Rosenstein, and N. Toyota, *'Phys. Rev. B*, 74, 104502, 2006.
[157] R. Lortz, N. Musolino, Y. Wang, A. Junod, and N. Toyota, *Phys. Rev. B*, 75, 094503, 2007.
[158] Y. Fasano, M. Menghini, F. de la Cruz, Y. Paltiel, Y. Myasoedov, E. Zeldov, M.J. Higgins, and S. Bhattacharya, *Phys. Rev. B*, 66, 020512, 2002.
[159] A.M. Troyanovski, M. van Hecke, N. Saha, J. Aarts, and P.H. Kes, *Phys. Rev. Lett.*, 89, 147006, 2002.
[160] To the best of our knowledge only one report on STS visualization of the vortex structure images more than 100 vortices as in our case: C. E. Sosolik *et al.*, Phys. Rev. B **68**, 140503 (2003).
[161] For a review on the techniques to analyze the topology of the vortex structure, see Y. Fasano and M. Menghini, Sup. Science and Tech. **21**, 023001 (2008).
[162] B. I. Halperin and David R. Nelson, *Phys. Rev. Lett.*, 41, 121, 1978.
[163] T. Nattermann, *Phys. Rev. Lett.*, 64, 2454, 1990.

[164] T. Giamarchi and P Le Doussal, *Phys. Rev. Lett.*, 72, 1530, 1994.
[165] C.P. Bean, *Phys. Rev. Lett.*, 8, 250, 1962.
[166] A. Piriou, Y. Fasano, E. Giannini, and Ø. Fischer, *Phys. Rev. B*, 77, 184508, 2008. and references therein.
[167] G. Blatter, M.V. Feigel'man, V.B. Geshkenbein, A.I. Larkin, and V.M. Vinokur, *Rev. Mod. Phys.*, 66, 1125, 1994.
[168] Y. Paltiel, E. Zeldov, Y.N. Myasoedov, H. Shtrikman, S. Bhattacharya, M.J. Higgins, Z.L. Xiao, E.Y. Andrei, P.L. Gammel, and D.J. Bishop, *Nature*, 403, 398, 2000.
[169] Z. Tešanović, *Phys. Rev. B*, 59, 6449, 1999.
[170] T. Hanaguri, Y. Kohsaka, M. Ono, M. Maltseva, P. Coleman, I. Yamada, M. Azuma, M. Takano, K. Ohishi, and H. Takagi, *Science*, 323, 923, 2009.
[171] M. Franz and Z. Tešanović, *Phys. Rev. Lett.*, 80, 4763, 1998.
[172] A. Mourachkine, *J. Supercond.*, 17, 771, 2004.
[173] N. Nakai, M. Ichioka, and K. Machida, *J. Phys. Soc. Jpn.*, 71, 23, 2002.
[174] M. Ichioka, K. Machida, N. Nakai, and P. Miranović, *Phys. Rev. B*, 70, 144508, 2004.
[175] A.E. Koshelev and A.A. Golubov, *Phys. Rev. Lett.*, 90, 177002, 2003.
[176] A. Gurevich, *Phys. Rev. B*, 67, 184515, 2003.
[177] K. Tanaka, D.F. Agterberg, J. Kopu, and M. Eschrig, *Phys. Rev. B*, 73, 220501(R), 2006.
[178] K. Tanaka, M. Eschrig, and D.F. Agterberg, *Phys. Rev. B*, 75, 214512, 2007.

Abbreviations

ACS	AC susceptibility
ARPES	Angle-resolved photo-emission spectroscopy
BCS	Bardeen-Cooper-Schrieffer (theory of superconductivity)
CDW	Charge density wave
DoS	Density of states
E_F	Fermi energy
k_F	Fermi wavevector
LDoS	Local density of states
LL	Luttinger liquid
MI	Metal-insulator
PDoS	Phonon density of states
q*n*D	Quasi-n-dimensional
RMS	Root mean square
SDW	Spin density wave
STM	Scanning tunnelling microscopy
STS	Scanning tunnelling spectroscopy
T_c	Zero-field superconducting transition temperature
T_{c2}	Superconducting transition temperature in a magnetic field
T_{MI}	Metal-insulator transition temperature
UCDW	Unconventional charge density wave
VL	Vortex lattice
VS	Vortex structure
W **WHH**	Werthamer-Helfand-Hohenberg (theory of upper critical fields)
XRD	X-ray diffraction
ZBC	Zero-bias conductance

Acknowledgements

It is half past five in the morning: armed with nothing but a pot of green tea and a rapidly-dwindling supply of patience I am baby-sitting the Aurora. For the past 60 hours it has led me on a merry dance from challenge to headache via catastrophe, in a pattern which has become all too familiar over the past few years. Why on earth would I want to thank anybody for this unique brand of torture?

At its worst, experimental condensed matter physics could be compared to one of those tragic mutually-destructive relationships which you read about in the tabloid press and think "That would never happen to me!" Although anybody looking at me this morning would probably disagree, the damage in this particular relationship has (thankfully) largely been confined to the apparatus. For this reason, I am indebted to the unfeasibly deep pockets and invariably good nature of Professor Øystein Fischer, not only for taking the gamble of employing me in the first place, but also for admirably bankrolling my quest for scientific breakthrough. It has been an unconventional, yet truly rewarding experience. My gratitude extends to Professors Hermann Suderow, Christoph Renner and Michel Decroux for agreeing to constitute my thesis jury.

Among all the people who have influenced and assisted me during this journey, several stand out for their exceptional contributions. Nobody has taught me more about experimental physics than Rolf Lortz, who not only shared his secrets of calorimetry and involved me in his own projects, but has always been ready to discuss and advise me on all aspects of our work, thus opening my eyes to the broader appeal of my research. I will always be grateful for this.

Whenever I have been confused by any delicate theoretical aspects of superconductivity, it has been reassuring to know that Enlightenment - in the form of Gilles Santi - is always close to hand. Gilles taught me almost everything I know about gap symetry and Fermi surfaces, had a

colossal impact on chapter 6 and has been excellent company on conferences and retreats. As far as actually using an STM is concerned, I was lucky enough to be trained by a master in Cédric Dubois. His tips and advice demystified a seemingly impenetrable pile of electronics and wiring, remaining at the forefront of my mind long after his departure. Without his groundbreaking early measurements on $PbMo_6S_8$, this thesis would have been immeasurably more painful.

Yanina Fasano showed me that there is so much more to vortices than mere core spectroscopy, thus revealing an entirely new branch of physics to me. Without her inspiration and tireless positive attitude, chapter 7 would be a pale shadow of itself. It was also a great pleasure to collaborate with Carmine Senatore, who generously performed the VSM measurements shown in the same chapter. We share an appreciation for the finer things in life, including vortex pinning and Serie A football. Furthermore, I acknowledge several illuminating discussions with Christophe Berthod, Thierry Giamarchi, Christian Bernhard, Laszlo Forro, Andrei Mourachkine and Christos Panagopoulos over the years. It has been very satisfying to see other scientists taking an interest in molybdenum cluster compounds.

The success of all my measurements has hinged on the excellent quality of crystals with which I was supplied by Michel Potel and his colleagues at Rennes: Patrick Gougeon, Diala Salloum, Octavio Peña and Roger Chevrel. I have also enjoyed excellent theoretical support on $M_2Mo_6Se_6$ from Lilia Boeri and Ole Andersen in Stuttgart and Jens Kortus in Freiburg.

It has been a great privilege to collaborate with Albin Demuer at the Grenoble High Magnetic Field Laboratory, thanks to his enthusiasm, humour and willingness to share his knowledge. I am also indebted to Antoine Paré and Arlei Antunes for their assistance, particularly Antoine's software contributions and Arlei introducing me to the benefits of Brazilian maté in the early hours of the morning.

When I first met Moritz Hoesch at a conference back in 2007 I could not have imagined how much he would contribute to our efforts to understand $M_2Mo_6Se_6$. Not only did he share his considerable inelastic X-ray scattering and diffraction expertise, but he also introduced me to ARPES techniques and can always be relied upon to solve any phonon-related mysteries. As with Albin, I hope our collaborations will continue long into the future. Dmitry Chernyshov at the ESRF Grenoble played a crucial rôle in our XRD experiments and data analysis; chapter 5 would be much poorer without him. The company and assistance of Holly Hedgeland during our recent ARPES measurements in Trieste

was also a huge pleasure.

The considerable practical aspect of this work has left me frequently dependent on the skills of my technicians. Roland Pellet and his team have never failed to impress me with the quality of their machining and their wonderful attitude, especially Miguel, Charly, Robert and Régis; I have thoroughly enjoyed working with them. Paul-Emile Bisson is missed enormously in our laboratory and his innovations made an immeasurable improvement to the general health of my cryostat. Further work by Géraldine Cravotto and Daniel Antonietti is also appreciated, with the electronic developments and support from Laurent Stark forming an invaluable contribution to the Aurora.

Although he has played an unusual rôle in a physics laboratory, I have had a very rewarding symbiotic relationship with Philippe Sormani. Armed with an infectious good humour, he has always been ready to lend a hand where needed, in addition to opening my mind to the ethnomethodological aspects of STM. The moment when we discovered multi-band superconductivity in $PbMo_6S_8$ together was truly special. I would also like to thank the students from the Datcha bar for helping out on numerous occasions late at night when any heavy lifting was required. On a more administrative front, Fabienne Hartmeier has dealt marvellously with the innumerable bills incurred by my research, which have an uncanny ability to bury themselves in my desk for 6 months. Though she will probably be keen to see the back of me, I will miss her seemingly unlimited organisational skills. I have also noted that the world would be a much happier place if it contained more people like Nathalie Chauduiron.

If one man deserves an award for unlimited patience in the face of adversity, it is Spiros Zanos. Faced with my "special needs" approach to ordering liquid helium on an almost daily basis, he has never let me down. While I wish I could do more to thank him, I fear that there will always be an element of chaos in my helium consumption.

In the world of business outside the laboratory, several individuals are conspicuous for the help they have given me. René Koch (of TECO René Koch) is an unfailing source of cryogenic inspiration, as is Munir Jirmanus (of Janis Inc.): the performance of my cryostat never ceases to amaze me. Fred Morgan (of Thern Inc.) remains largely responsible for my being able to accomplish the deceptively challenging feat of lowering the insert into my cryostat, while Tim Allmendinger (Geospace Technologies), Marcel Dubey (GMP) and Matt Boughan (Acoustic Solutions) have all had a considerable impact on noise and vibration reduction. Finally, I have been heavily reliant on Jorg Töbisch, Stefan

Riesner, Thomas Beppler and the LoT-Oriel team for helping me keep the PPMS alive for the past four years against all the odds.

Back in the lab, so many others have made positive contributions to the mayhem. Some have departed for pastures new - Giorgio, Christian, Olivier, Silvia, Tristan, Corentin, Ignace, Uthaya - while others remain: Ivan, Nate, Pierre, Mathieu, Louis, Manu and Noé le petit roi du LaTeX. Special mention must be given to Alex II, with whom I have shared an office and several unforgettable conference "holidays". If my future office partners are even half as amiable then I will be very lucky.

To maintain a healthy balance, I have been fortunate enough to enjoy support from many other non-scientific quarters. In particular, Tom, Seb and Rebecca have maintained a steady interest in my work, always succeeding in cheering me up regardless of the gravity of the most recent lab-based disaster. The time spent on two wheels in the mountains with Gladys and Enrique has also been very precious to me. J'aimerais aussi remercier toute l'équipe des riders qui ont rendu ces dernières deux années tellements mémorables: Marie-Claire, Jean-Marc, Mia, Juan, Pierric, Sophie, Junior, Concha, Diane, Binh, Pika, Pascale, Fiona, Guillaume, Fred et tous les autres. You will all be sorely missed.

Finally and most importantly, I wish to thank my parents, without whose sacrifices and support I could not hope to be where I am today. Even though this is currently in a laboratory with severe thermoregulation issues, staring at a temperature controller and oscilloscope with very sleepy eyes.